Investigation of New Techniques for Increasing Efficiencies in Spectroscopic Surveys

by

Farbod Jahandar
B.Sc., University of Victoria, 2016

A Thesis Submitted in Partial Fulfillment of the
Requirements for the Degree of

MASTER OF SCIENCE

in the Department of Physics and Astronomy

Investigation of New Techniques for Increasing Efficiencies in Spectroscopic Surveys

by

Farbod Jahandar
B.Sc., University of Victoria, 2016

Supervisory Committee

Dr. K. Venn, Supervisor
(Department of Physics and Astronomy)

Dr. P. Côté, Departmental Member
(Department of Physics and Astronomy)

Dr. S. Fabbro, Departmental Member
(Department of Physics and Astronomy)

Supervisory Committee

Dr. K. Venn, Supervisor
(Department of Physics and Astronomy)

Dr. P. Côté, Departmental Member
(Department of Physics and Astronomy)

Dr. S. Fabbro, Departmental Member
(Department of Physics and Astronomy)

ABSTRACT

The efficiency of different spectroscopic techniques are examined through four different approaches: detailed analysis of IR spectra from the APOGEE database and examination of persistence, observing extremely metal-poor stars using the Plaskett telescope at the DAO, three analyses of various applications of machine learning in astronomy, and efficient transmission of light through optical fibres.

Through the first study, the technical effects of persistence in the APOGEE's IR spectra are examined, and a new technique for removing the persistence is introduced. Most of the globular cluster Pal 1's spectra in the APOGEE database are affected by persistence. Therefore, the Pal 1 spectra are corrected for the persistence and their stellar abundances are determined independently from the APOGEE's pipeline, ASPCAP. Our results for the known members of Pal 1 were in a close agreement with the results from Sakari et al. (2011). Comparison between the results from the corrected and the original spectra suggest that the persistence could have a critical effect on the results.

The second study of this thesis focused on observations of extremely metal-poor (EMP) stars from the Pristine survey. Through the DAO-Pristine project, we narrowed down the initial list of the Pristine survey by observing over 50 targets during 25 observing nights. The Ca II triplet absorption lines of the observed targets were

examined and used for estimating the metallicity of the objects. Twelve candidate EMP stars with weak Ca II triplet lines are chosen from the observed targets. These candidate EMP stars will be observed with larger telescopes for more accurate determination of their metallicity.

This thesis also presents the result of a threefold analysis for using machine learning techniques in astronomy. The supervised machine learning methods are used for determination of the stellar parameters of stars using their raw spectra, and unsupervised machine learning methods are used for classification of supernovae Type Ia from their calibrated spectra. The supervised analysis of the IR and optical spectra suggested that the StarNet neural network (Fabbro et al. 2017) can predict the stellar parameters of the APOGEE database and synthetic spectra, efficiently and accurately. The effect of persistence in the StarNet's results are examined, and we showed that the persistence does not have a critical effect on the overall performance of the StarNet. In addition, multiple unsupervised machine learning techniques such as K-mean and Self Organizing Maps (SOMs) are used for classification of the supernovae Type Ia spectra. The preliminary results suggest that a minimum of three subclasses of supernovae Type Ia can be found from our data, which are consistent with the previous studies.

Finally, this thesis presents our final results for an optical system we designed for the MSE project. At UVic, we have used the standard collimated beam method, or "ring test," to measure the Focal Ratio Degradation (FRD) of MSE-like fibres. The FRD of the system is determined from the ratio of the Full Width Half Maximum (FWHM) to the radius of the ring. Early ring test results from a sample of MSE-like fibres show an FRD of 3.7%, which meets the MSE science requirement (i.e. FRD $\leq$ 5% at f/2). Also, we have automated the ring test for fast, repeatable, and efficient measurements of an individual fibre in multi-fibre bundles. Our future tests will include automated non-static fibres in preparation for the MSE build phases.

Contents

List of Tables

List of Figures

ACKNOWLEDGEMENTS

I would like to thank:

Farideh Ghodsi and Bahram Jahandar for all the love, supports, constant encouragements and the amazing chances you have given me over the years.

Kim Venn for your patient guidance and encouragement during my master's studies. I have been lucky to have a supervisor who cared so much about my work and my research, and it was an honour for me to learn from your exceptional knowledge and amazing personality.

Patrick Côté, Sébastien Fabbro, Colin Bradley, David Crampton, Darren Erickson, Hossen Teimoorinia and Alan McConnachie for giving me the opportunity to work on amazing projects under your supervision. I am very grateful of your support, wisdom, advice and helps through my projects.

Collin Kielty, Ruth Digby, Nic Loewen, Spencer Bialek, Teaghan O'Briain, Stephanie Monty and Trystyn Berg for being wonderful and stellar friends and colleagues. I am grateful of your helps and kindness, and looking forward to working with you in the future.

Jo Bovy, Matthew Shetrone, Nicolas Martin, Else Starkenburg, Mike Irwin, Dave Balam and Charli Sakari the great astrophysicists who helped me significantly during my master's studies.

The knowledge of anything, since all things have causes, is not acquired or complete unless it is known by its causes.
Avicenna (1020 CE)

DEDICATION

To my parents, Farideh Ghodsi and Bahram Jahandar.

Chapter 1

Introduction

In astronomy, observation is the process of collecting and analyzing data recorded by telescopes. Due to the enormous distances to astronomical objects, their light is the main measurable and analyzable property of the far astronomical objects. Considering the countless number of stars in the sky and the limited number of observing tools; efficient observation of stars can be challenging. This thesis examines the potentials of different techniques for increasing efficiency of spectroscopic observations with telescopes. Examination of various databases such as APOGEE database along with detailed spectroscopy of stars are the main elements of this thesis. The following sections provide some scientific background for both observational and instrumental perspectives of this thesis.

1.1 Galactic Archaeology

Galactic archaeology is a field in modern astronomy that covers various astrophysical disciplines, from the examination of the nearby stellar systems to the study of the evolution of different galaxies in the Universe. Galactic archaeology can help us to trace the formation history of different galaxies such as the Milky Way galaxy using the chemical and kinematic analysis of its stars. In fact, the Milky Way galaxy is the proving ground for the Galaxy formation theory as we can observe and examine various properties of stars in different components of the Galaxy. As is shown in Fig. 1.1, our galaxy has three main components:

- The Galactic bulge is the central component of the Milky Way galaxy that distribution of stars becomes vertically thicker. The bulge stars are relatively old with age of older than 9 Gyr and have metallicity range of -1.0 dex to 0.5 dex.

- The Galactic disk is the dominant stellar component of the Milky Way galaxy. The disk is rotating and is flattened with an exponential decrease in the number of stars as you move outwards from the centre. The Galactic disk has two components, Thin Disk and Thick Disk. The Thin Disk contains young stars (with [Fe/H] range of -0.5 dex to 0.3 dex) that are distributed in a disk with the scale height of 350 pc and radius of 25 kpc. On the other hand, the Thick Disk mostly contains old and metal-poor stars ([Fe/H] range of -2.2 dex to -0.5 dex) that are distributed in a disk with the scale height of 1 kpc and radius of 25 kpc.

- The Galactic halo is the other prominent component of the Milky Way galaxy. This component contains several globular clusters and field stars and is located far out of the Galactic bulge. The Galactic halo will be discussed in the next section.

Study of stars is the inevitable part of the Galactic archaeology as some stars can be nearly as old as the Universe. The examination of chemistry and kinematics of stars helps to understand the formation of the various elements existed in the interstellar medium that formed different stellar populations like star clusters.

1.1.1 Metal-poor Halo

The metal-poor halo of the Milky Way galaxy contains about 1% of stars in the Galaxy. Because of the old formation history of the stars in the halo, the Galactic halo is one of the best study-targets for understanding the formation history of the Galaxy. The stars in the Galactic halo are usually metal-poor with the metallicity of [Fe/H]<-1, and they can be nearly as old as the Universe (Peacock et al. 2015; Carollo et al. 2007; Carollo et al. 2010). In addition, the study of these metal-poor stars can give us insights into the chemical history of the Milky Way galaxy as they mostly have not been contaminated with the other astrophysical processes (Hattori et al. 2013; Cohen et al. 2008; Beers & Christlieb 2005). The other factor that made the Galactic halo a unique testbed for the study of the Galaxy formation is that they are mostly collisionless. Therefore, the halo objects were able to conserve the halo stars' initial orbital motion. In fact, the orbital motions of the stars in the Galactic halo reflect the type of early supernovae and the orbital behaviour of the Galaxy's progenitor; therefore it can be examined to understand the Galaxy's evolution.

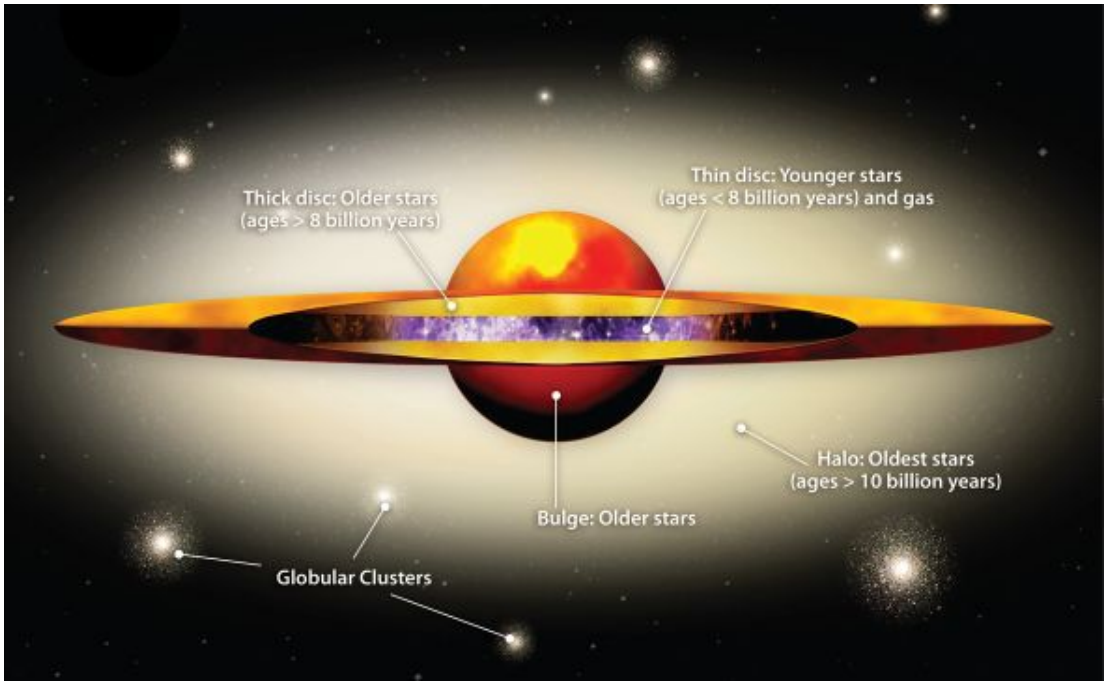

Figure 1.1: Our Milky Way galaxy has multiple components. Stars in each of these components have distinct chemical, kinematical and dynamical properties. Image credit: http://astronomy.swin.edu.au/cosmos/T/Thick+Disk

In general, the Galactic halo extends up to 100 kpc from the centre of the Galaxy and the analysis of the proper motion is one of the efficient ways of examining the orbital motion of stars in the halo. Studies of the line-of-sight velocity and spatial distribution of stars in the halo have inspired a variety of kinematic and distribution models. Recent studies have introduced various distribution models such as tangentially-anisotropic-orbital distributions (Kafle et al. 2012; Sommer-Larsen et al. 1997) and radially-anisotropic distributions(Deason et al. 2012) of the stars in the halo.

1.1.2 Stellar Clusters

A stellar cluster is defined as a group of stars that are gravitationally bounded with shared physical properties such as age and chemical composition. Study of stellar clusters helps astronomers to understand stars' and galaxies' evolution. In general, there are two types of stellar clusters: open clusters and globular clusters.

Open clusters contain up to few hundreds of stars and usually do not have a symmetric shape as their number of stars do not provide enough gravity to form a spherical shape (see Fig. 1.2). They are usually young with age of few Gyrs and metallicity range of -0.5 $<$[Fe/H]$<$ 0.5 (Paunzen et al. 2010; Salaris et al. 2004). In contrast to open clusters, globular clusters can contain up to a million of stars that make them capable of being fully spherical and symmetric (see Fig. 1.3). Most of the globular clusters are located in their host galaxy's halo and are metal-poor with [Fe/H]< -1. Majority of the globular clusters are among the oldest stellar populations and are relatively dense with diameters of a few parsecs to dozens of parsecs (Kirby et al. 2016; Conroy 2012).

All stars in a stellar cluster are formed through a same star formation process; therefore they are born at the same time. This unique feature gives us the opportunity to examine the stellar evolution by observing similar stars with different masses. Examination of the colour-magnitude diagram (CMD) of stars in a globular cluster is one of the essential ways to study the stellar evolution of the cluster. In fact, CMDs demonstrate the correlation between temperatures and brightness of stars in a cluster. Different properties of clusters such as their age can be determined by comparing synthetic evolution models or isochrones of stars with the CMD (see Fig. 1.4).

Figure 1.2: The open cluster Messier 45 (M45), which is also known as the Pleiades cluster. This open cluster is 120 pc (van Leeuwen 2009) away from us and contains hundreds of stars. Image credit: NASA/ESA/AURA/Caltech.

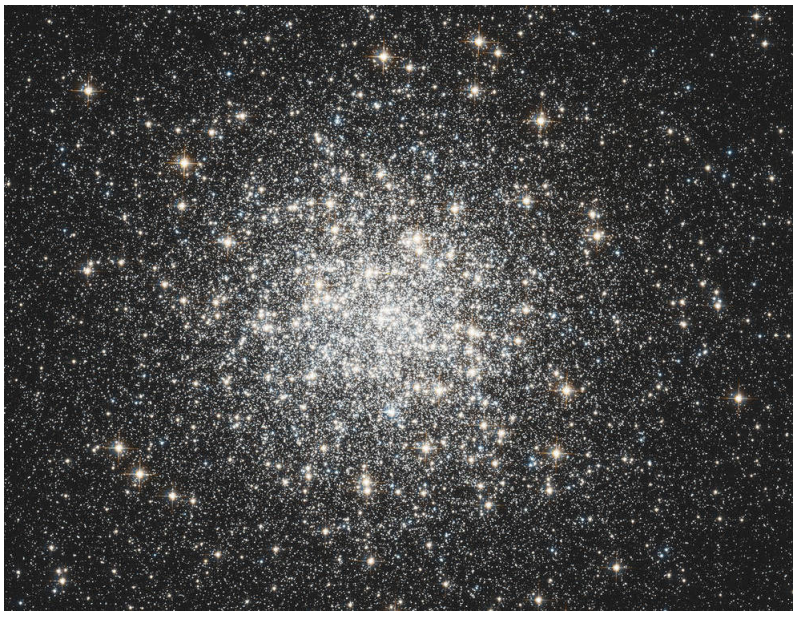

Figure 1.3: The extremely metal-poor globular cluster Messier 3 (M3). This globular cluster is 10.4 kpc (Paust et al. 2010) away from the Sun and contains about 500,000 stars. Image credit: NASA, ESA, STScI and A. Sarajedini (University of Florida)

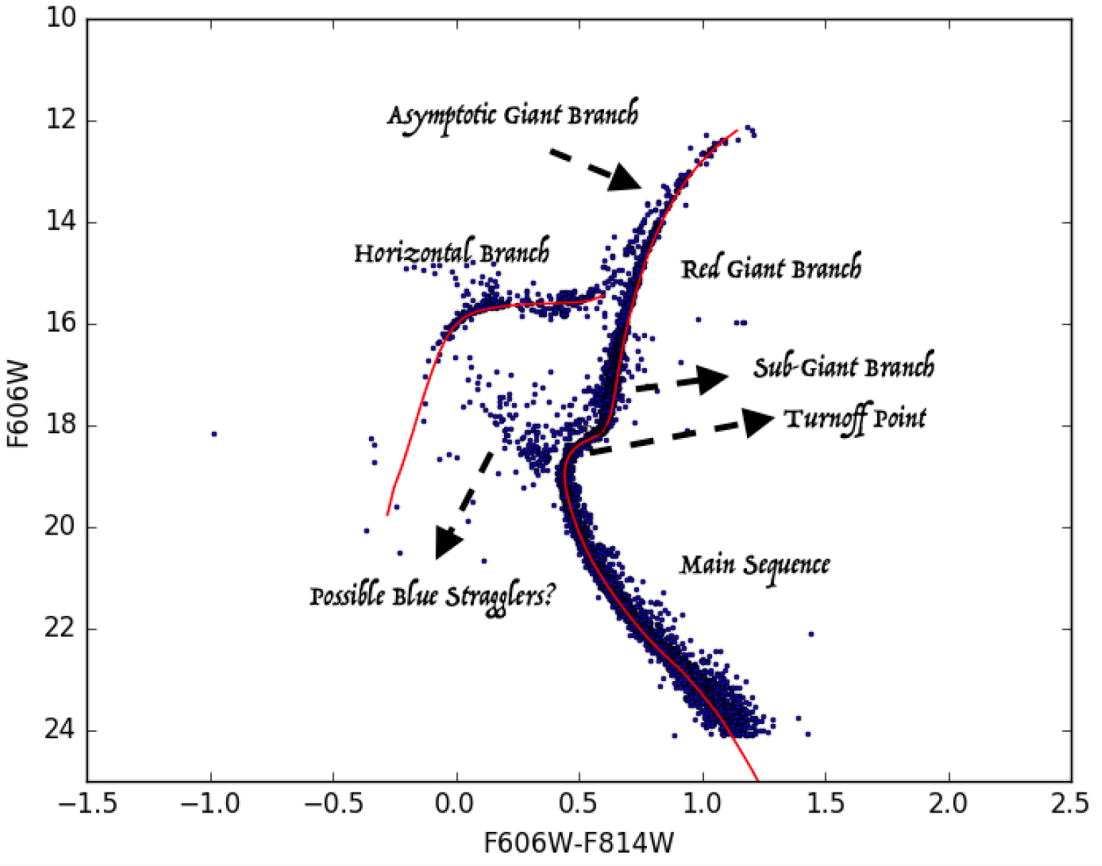

Figure 1.4: The colour-magnitude diagram of M3 (from Sarajedini et al. 2007) with an isochrone for age of 11 Gyr, from the Victoria-Regina Stellar Models (VandenBerg et al. 2006). Note that the F606W and F814W bands are almost equivalent to the V and I bands (respectively) in the Johnson magnitude system.

1.1.3 Photometric and Spectroscopic Surveys

Systematic observation of a vast region of the sky is called a sky survey. Sky surveys have provided largest datasets for various branches of astronomy. The data in a survey can be based on different physical properties such as the wavelength regime (i.e. infrared and optical fields), the observing targets (stars, galaxies or other astronomical objects) and the observation techniques (such as direct imaging, photometry and spectroscopy). Also, the wide range of data in the sky surveys make them an ideal tool for finding rare astronomical phenomena (Djorgovski et al. 2013).

Currently, thanks to the recent large astronomical surveys such as the Sloan Digital Sky Survey (SDSS), the Panoramic Survey Telescope & Rapid Response System (Pan-STARRS) and Two Micron All-Sky Survey (2MASS), a wide range of science is enabled. The following surveys are distinctly used in this thesis:

- The Sloan Digital Sky Survey (SDSS; Gunn et al. 1998; Gunn et al. 2006; York et al. 2000; Fukugita et al. 1996; `http://sdss.org`) is one of the most successful surveys in the modern astronomy that started scanning the night sky from over a decade ago. The first two generations of SDSS (SDSS-I and SDSS-II) were completed by 2008 and identified over 700000 objects within the 8000 $\deg^2$ of the sky, and with the completion of the third extension (SDSS-III) the total coverage increased to 14500 $\deg^2$ of the Northern sky. The first three generations used a 2.5 telescope at Apache Point Observatory in New Mexico that could cover the wide wavelength range of 3000 Å to 10 600 Å (Gunn et al. 2006). Also, two on-going generations of SDSS-IV and SDSS-V are planned to observe more targets from both the Northern and the Southern skies by the next decade. These future surveys will use the Irenee de Pont Telescope at Las Campanas Observatory, which is a Ritchey-Chrétien 2.5-m telescope (Bowen & Vaughan 1973) and will scan the Southern sky.

- The Panoramic Survey Telescope & Rapid Response System (Pan-STARRS, Kaiser et al. 2002; Kaiser et al. 2010) is another successful wide-field survey that is done by four 1.8 m telescopes (3 deg diameter and 7 square deg field of view for each of them). This instrument has a 1.4 gigapixel camera and covers five broadband filters of *g, r, i, z* and *y* (see the next section for more details about different photometric systems). Due to the high-resolution observations of targets, other surveys such as the Pristine Survey has used the photometric

data of the Pan-STARRS database in their analysis (see Chapter 3 for more details about the Pristine survey).

1.2 Observations

1.2.1 Photometry and Spectroscopy

The electromagnetic radiation we receive from astronomical objects is called flux, and the process of measuring and analyzing this flux is called photometry. The photometric data of stars can be determined by isolating part of the spectrum with different wavelength filters. The isolated part is the bandpass, and the central wavelength of the filter is the effective wavelength. The general equation for the monochromatic flux is as follows:

$$F_\lambda = \frac{\Delta E}{\Delta A \Delta t \Delta \lambda}$$

where ΔE is the energy arriving at the telescope, ΔA is the collecting area of the telescope, Δt is the exposure time and $\Delta\lambda$ is the wavelength range over which we have collected photons.

Today several photometric systems such as UBVRI, Johnson-Morgan-Cousins and the Sloan Digital Sky Survey (SDSS) systems are well known. The central bandpass and wavelength coverage of different photometric systems are shown in Fig. 1.5.

The flux is a general term for the brightness of an object, but sometimes it is required to specify the relative brightness of stars. In this case, the apparent magnitude is the alternative term for the brightness of the star, and it can be expressed as follows:

$$m_A - m_B = -2.5 log(F_A/F_B) \tag{1.1}$$

Here m_A and m_B are the apparent magnitudes of two different targets and F_A and F_B are the relative fluxes of the targets.

The analysis of the flux of an object in different wavelength regimes can tell us about various physical properties of the object (i.e. temperature, distance, chemistry and size). This analysis can be done by examination of the absorption lines in the light spectrum of the object. In fact, when light interacts with a layer of gas, a group of electrons in the molecules of the gas layer absorb some energy from the incident light. As the result of this process, the spectrum from the gas layer will have some

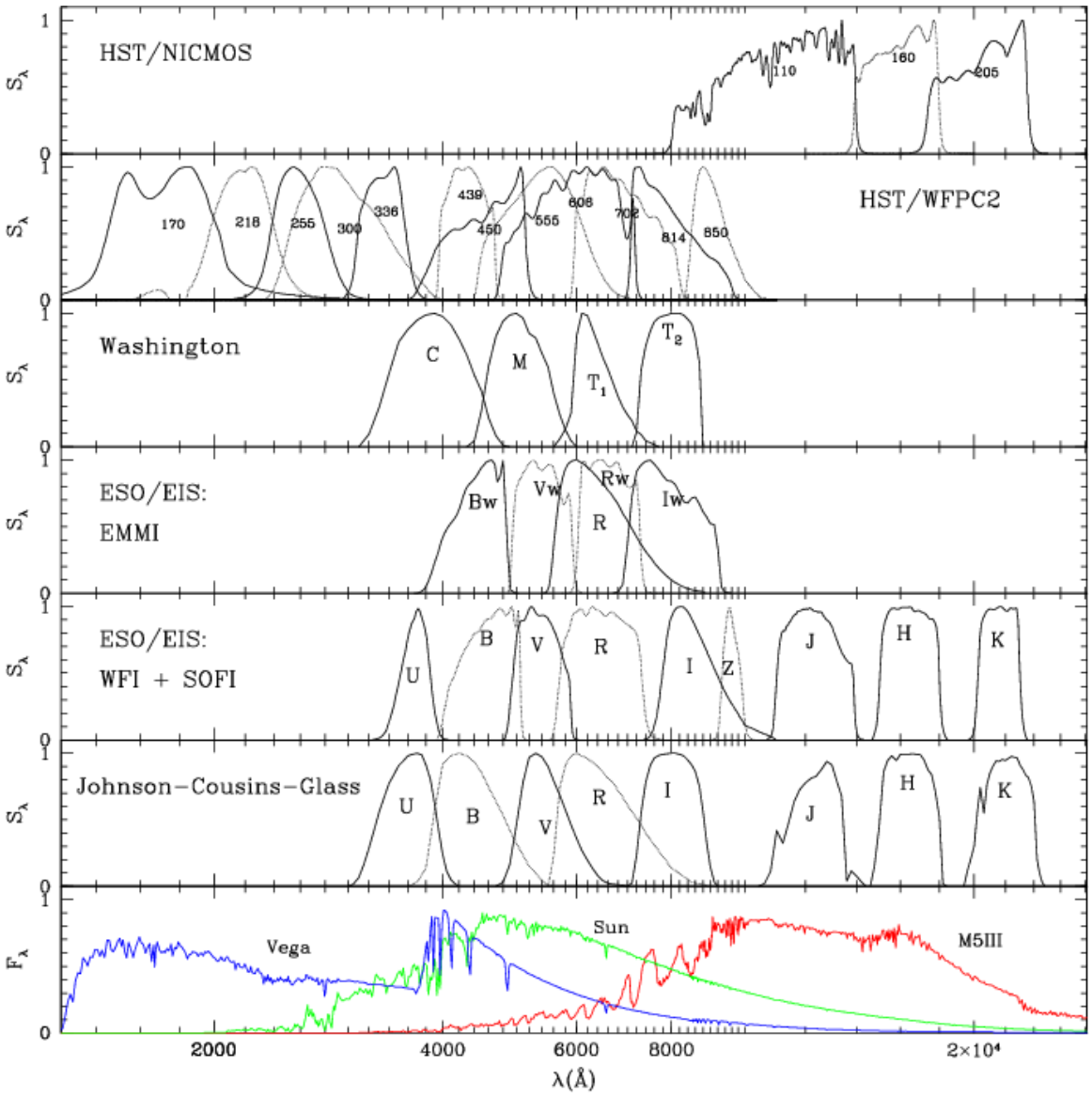

Figure 1.5: The wavelength coverage in different photometric systems (from Girardi et al. 2002).

missing portions due to the wavelength of the absorbed energies. These missing lines are called absorptions lines. The study of absorption lines helps us to understand the chemistry of the object and also its dynamical properties such as radial velocity and rotation speed. The process of collecting and examining an object's spectrum is spectroscopy.

1.2.2 Data Reduction

Charge Coupled Devices (CCDs) are sensitive photon detectors that allow astronomers store observed images of the astronomical objects. The surface of a CCD contains several pixels that record pixel counts when a photon hits the CCD. In fact, the collision forms an electron that can be preserved digitally on the CCD's pixels. The number of each pixel's count is proportional to the number of electrons captured in the pixel. Therefore, the total number of counts is proportional to the total energy (i.e. # of counts $\propto \Delta$E).

The raw images require multiple corrections to be usable in science. The main correction steps are as follows:

- Bias and Flat Corrections
- Background Correction
- Photometric Calibration

1.2.3 Bias and Flat Corrections

The first step to calibrate a CCD is to remove the bias and flat frames. In general, CCDs can have a fixed pattern of noise even without receiving any signal, which is called the bias frame. The bias frames are repeatable and should be taken with minimum exposure time (zero seconds). The second calibration frame is the flat frame. Sometimes the exposed light on a CCD does not form a homogenous image as the light is not distributed on the CCD uniformly. A common cause of this non-uniformity is dust on the telescope's camera. The flat correction can be done by taking a picture from a covered but illuminated CCD when the dome is closed. In this case, all the obscured area on the CCD will be exposed and can be removed from the future science frames.

1.2.4 Background Correction

If we look at an empty part of the sky with no stars, we still record some pixel counts on the CCD because the night sky is not entirely dark. This faint background can have a critical effect on the science frames. Therefore, it has to be removed from the pixel counts of the target star. The critical step for removing the background is estimating the pixel counts from a part of the sky with the minimum number of stars. Note that the sky background frame can be contaminated with some other factors such as the cosmic rays, faint nearby stars or even the saturation from the point spread function (PSF) of the target star.

1.2.5 Photometric Calibration

Once the general systematic calibrations and background corrections are done, the pixel counts in the science frames should be converted into a photometric system. This conversion allows astronomers to observe and examine the science frames in different wavelength regions with different filters. The photometric calibration is not constant for different instruments as the conversion factor between the pixel counts and the real photometric value depends on several factors such as the size of the telescope and the filter.

1.2.6 Persistence

Removal of persistence on data is a critical challenge in the infrared (IR) astronomy. Persistence is the faint signature of the previous exposure's image on the CCD's pixels that decays over time. This type of noise usually occurs in IR imaging when a pixel in the IR array is exposed to a light that exceeds roughly more than half well of the pixel. Note that the amount of persistence mostly depends on the amount of time the detector has held the charge and the next exposure. In other words, the CCDs can eliminate the persistence effect if their pixels have enough time to release the stored charge. One of the critical issues that persistence can cause on a spectrum is showing unreal spurious features such as extra absorption lines from the previous target's spectrum on the new science frame (see Fig. 1.6; Smith et al. 2008).

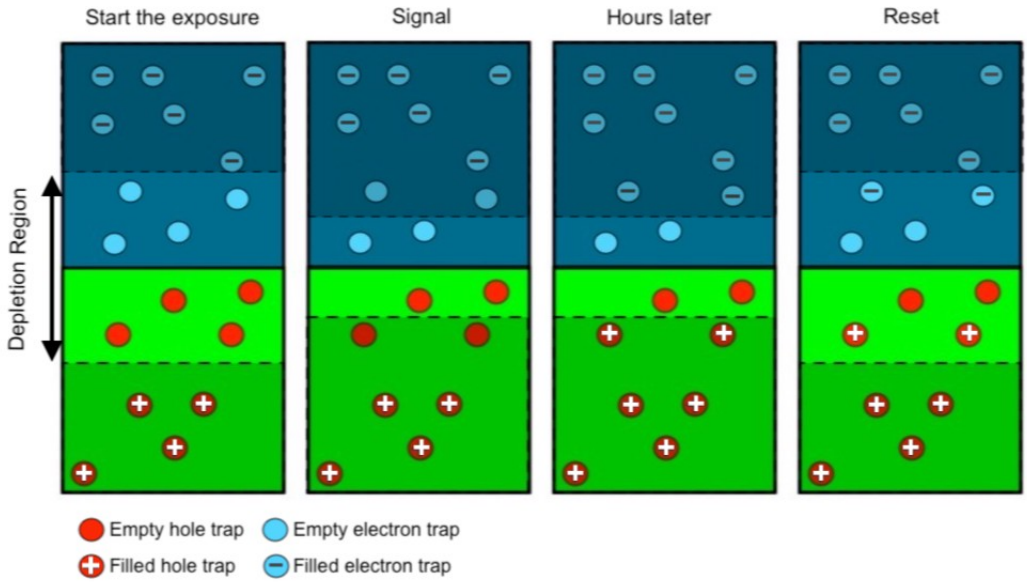

Figure 1.6: The effect of persistence on an IR detector (modifed from Anderson et al. 2014). The left panel shows the stable state of the CCD as there are filled traps in the free-charge region and empty traps in the depletion region. In the next panel, the CCD is exposed by a source of light, which increases the size of the free-charge region and captures some of the empty traps. Within the next few hours, we will have the third panel. In the third panel, all the empty traps in the free-charge region are filled with negative or positive charges. Finally, in the last panel, the whole system is reset, but the depletion region is not filled with empty traps anymore. In fact, the last panel tells us that in the next exposure there will be an imprint of the previous light from the decay of the filled traps in the depletion region.

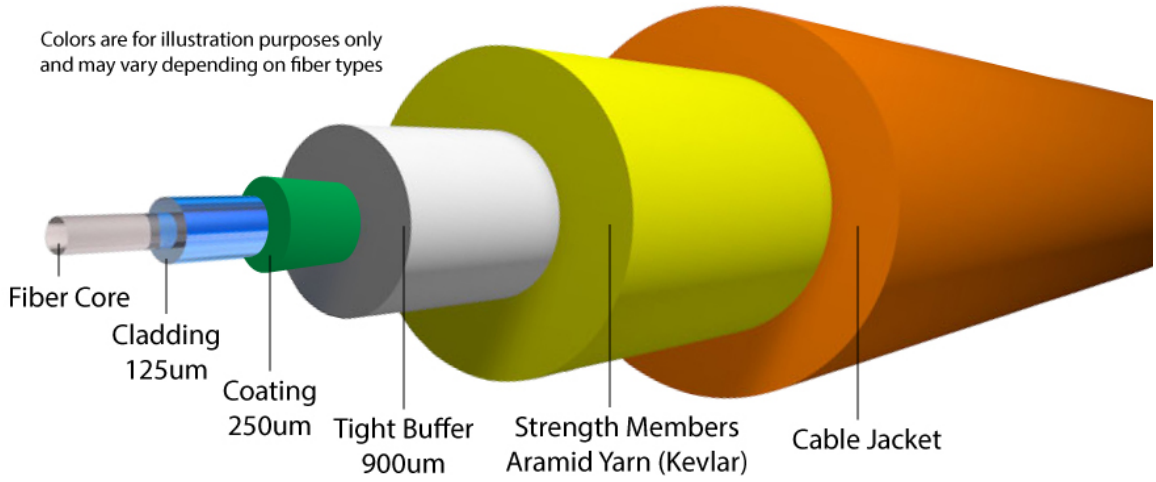

Figure 1.7: The general schematic of an optical fibre. The main core of the fibres can be protected with multiple protection layers to make them resistant to unstable and extreme conditions. Image credit: http://www.primuscable.com/info/fiber.aspx

1.2.7 Optical Fibre Spectroscopy

Over the past few decades, the technical developments in photonic technologies such as optical fibres have been a rapidly evolving industry. The main use of the optical fibres in astronomy is the efficient transmission of light from the focal plane to the spectrographs or CCDs. Currently, the limited amount of observing time and observing tools encourage astronomers toward extensive use of optical fibres in telescopes (see Fig. 1.7, Jovanovic et al. 2017). One of the first successful experiences of using optical fibres for transmission of light was Gemini Remote Access to CFHT-ESPaDOnS Spectrograph (GRACES) that made a connection between the Canada-France-Hawaii Telescope (CFHT) and Gemini Observatory. A system with 270m long optical fibres that transfers light from the Gemini telescope to the ESPaDOnS Spectrographs (Pazder et al. 2014; Chené et al. 2014).

In general, there are two main types of optical fibres, Single-mode fibres and Multi-mode fibres. The main difference between these two types of fibres is in their core's size. The single-mode fibres have a thin core with the average core size of 9 μm; therefore they are only suitable for propagation of a single wavelength light. Consequently, the small size of the single-mode fibres causes less reflection of light and hence less attenuation that let the light transmit in a longer path. In contrast to the single-mode fibres, the multi-mode fibres have a thicker core with the average core

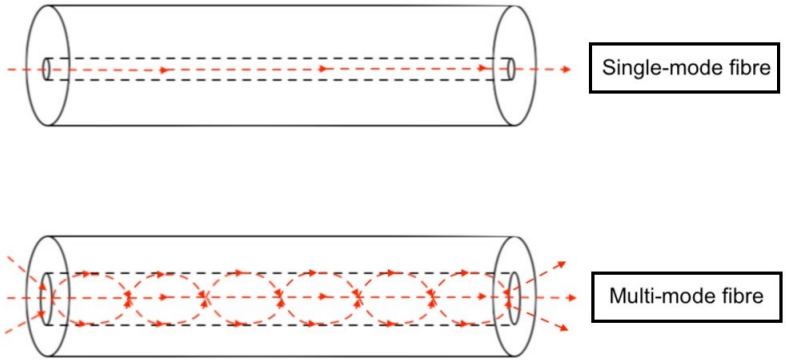

Figure 1.8: Difference between single-mode fibre and multi-mode fibre. Single-mode fibres can only transmit a single wavelength signal, but the multi-mode fibres are capable of transmitting multiple wavelengths of light simultaneously. Note that the single-mode fibres have a smaller core and are cheaper than the multi-mode fibres.

size of about 50 μm. The larger core of the multi-mode fibres makes them capable of transmitting multiple wavelengths of light. However, the high number of light reflection causes higher attenuation that makes the multi-mode fibres only usable for the short distances (see Fig. 1.8).

1.3 Thesis Map

This thesis has the following structure:

Chapter 2 examines the globular cluster Palomar 1 and its surrounding field in the SDSS-APOGEE database (DR12) and also it investigates the possible effect of persistence on the IR spectra.

Chapter 3 demonstrates results from the observations and analysis of the extremely metal-poor stars from the Pristine survey using the Plaskett telescope at the Dominion Astrophysical Observatory.

Chapter 4 includes my contributions to three different machine learning projects. This chapter investigates the potential of using machine learning techniques for analyzing spectra of stars and supernovae.

Chapter 5 mostly focuses on instrumental astronomy. This chapter demonstrates full automation of quality tests for optical fibres and also it reports our pre-

liminary results for the optical fibres quality of the Maunakea Spectroscopic Explorer project.

Chapter 6 gives a summary of all the mentioned projects in this thesis. It also suggests the future work and projects that can be considered as the follow-up projects.

Chapter 2

The Peculiar Globular Cluster Palomar 1 and Persistence in The SDSS-APOGEE Database

This chapter was originally published in the Monthly Notices of the Royal Astronomical Society journal (2017, MNRAS, 470, 4782) by Farbod Jahandar, Kim A. Venn, Matthew D. Shetrone, Mike J. Irwin, Jo Bovy, Charli M. Sakari, Collin L. Kielty, Ruth A. R. Digby and Peter M. Frinchaboy. In this publication, I led the data extraction and re-processing, data analysis, model atmospheres analysis and data interpretations; and I made all of the plots, figures, tables; and oversaw the submission, refereeing, and publication processes of the journal.

2.1 Abstract

The SDSS-III APOGEE DR12 is a unique resource to search for stars beyond the tidal radii of star clusters. We have examined the APOGEE DR12 database for new candidates of the young star cluster Palomar 1, a system with previously reported tidal tails (Niederste-Ostholt et al. 2010). The APOGEE ASPCAP database includes spectra and stellar parameters for two known members of Pal 1 (Stars I and II), however these do not agree with the stellar parameters determined from optical spectra by Sakari et al. (2011). We find that the APOGEE analysis of these two stars is strongly affected by the known persistence problem (Majewski et al. 2015; Nidever et al. 2015). By re-examining the individual visits (i.e. single observations, often one amongst many observations that will be coadded), and removing the blue (and sometimes green) APOGEE detector spectra affected by persistence, then we find excellent agreement in a re-analysis of the combined spectra. These methods are applied to another five stars in the APOGEE field with similar radial velocities and metallicities as those of Pal 1. Only one of these new candidates, Star F, may be a

member located in the tidal tail based on its heliocentric radial velocity, metallicity, and chemistry. The other four candidates are not well aligned with the tidal tails, and comparison to the Besançon model (Robin et al. 2003) suggests that they are more likely to be non-members, i.e. part of the Galactic halo. This APOGEE field could be re-examined for other new candidates if the persistence problem can be removed from the APOGEE spectral database.

2.2 Introduction

Palomar 1 (Pal 1) is an unusual globular cluster. It is young (4-6 Gyr; Sarajedini et al. 2007) and it has a high metallicity ([Fe/H] $= -0.6 \pm 0.1$; Sakari et al. 2011; Monaco et al. 2011); however, it is located 3.6 kpc above the Galactic plane, and 17.2 kpc from the Galactic Centre (Harris 1996, 2010 edition). Niederste-Ostholt et al. (2010) examined SDSS and HST photometric fields around Pal 1, and detected a dispersed tidal tail extending up to 1^o (~ 0.4 kpc, or ~ 80 half-light radii) from either side of the cluster centre, with roughly as many stars in the tails as in the central cluster region.

Examination of the chemical abundances of the stars in Pal 1 can be used to study the origin of this system. If Pal 1 is a globular cluster then its stellar population will show a Na-O anti-correlation (as seen in other globular clusters, see Carretta et al. 2010). However, if Pal 1 is a captured stellar group from a dwarf galaxy, then it can be expected to show lower ratios of the α-elements (amongst other chemical signatures, e.g., see Venn et al. 2004; Tolstoy et al. 2009; Frebel & Norris 2015). Sakari et al. (2011) determined the elemental abundances of five stars in Pal 1 from high-resolution HDS Subaru spectroscopy. There was no evidence for a Na-O anti-correlation in the sample, and the [α/Fe] ratios were slightly lower than Galactic field stars at the same metallicity but only with 1σ significance. These signatures do not favour *either* scenario for the origin of Pal 1; however, Sakari et al. (2011) also found high values of [Ba/Y] and [Eu/α] that indicate unique contributions of r-process elements in this system, which seem to differ from most Galactic stars.

The physical properties of Pal 1 more closely resemble those of young clusters associated with the Sgr stream (i.e. Pal 12 and Ter 7; Sakari et al. 2011), or the intermediate-age clusters in the LMC (Sakari et al. 2017; Mucciarelli et al. 2008; Hill et al. 2000). Like Pal 1, those clusters also have young ages determined from isochrone fitting (Dotter et al. 2008; Siegel et al. 2007; Salaris & Weiss 2002) and show

lower [α/Fe] ratios for their metallicities (Sbordone et al. 2007; Cohen 2004; Bonifacio et al. 2004). Furthermore, neither Pal 1, nor the other young halo clusters, show the sodium-oxygen anti-correlation that Carretta et al. (2010) have shown is typical of globular clusters in the Milky Way. Another interesting sparse and young cluster in the halo is Rup 106. Like Pal 1, Rup 106 also has low [α/Fe] for its metallicity and no Na-O anti-correlation (Villanova et al. 2013). Rup 106 is not associated with any stellar streams, unlike the Sgr clusters. However, Rup 106 also shows low [La/Fe] and [Na/Fe], so does not appear to be directly linked to Pal 1. Pal 1 may also be linked to the Canis Major over-density based on its chemistry, e.g., high [Ba/Fe] and [La/Fe] (Sakari et al. 2011; Martin et al. 2004; Chou et al. 2010).

If Pal 1 is a tidally disrupted globular cluster, then it contributes to probing the shape of the Milky Way halo. Palomar 5 (Pal 5), another low-mass, low-velocity dispersion globular cluster with more spectacular tidal tails, has been used to model the Galactic potential by Bovy et al. (2016a), Ishigaki et al. (2016) (2016), Grillmair (2006), and Belokurov et al. (2007). Pal 5 also shows gaps in the tidal tails that have been examined for constraints on mini-halo substructure (Bovy et al. 2016b; Carlberg et al. 2012). The tidal tails around Pal 1 are much shorter. Characterizing this system further by identifying member stars in the tidal tails, or in a more extended envelope, could be used to better study the shape of the Milky Way halo and the origin and evolution of this cluster.

In this paper, we examine the SDSS-APOGEE DR 12 database, which targeted Pal 1 as part of its globular cluster ancillary data project. Our search for new members of Pal 1 required a critical and substantial re-examination of the individual visit spectra and data analysis techniques. In this paper, we present our target selection methods, and cleaning of the combined spectra to remove the persistence problem, and re-analysis of the stellar parameters using the FERRE pipeline. We compare the results with those from Sakari et al. (2011) and Niederste-Ostholt et al. (2010), as well as with the Besançon model (Robin et al. 2003).

2.3 APOGEE data

The Apache Point Observatory Galactic Evolution Experiment (APOGEE) is a high-resolution, high signal-to-noise infrared (IR) spectroscopic survey of over 100,000 red giant stars across the full range of the Galactic bulge, bar, disk, and halo (Majewski et al. 2015). The survey was carried out at the 2.5-m Sloan Foundation Telescope

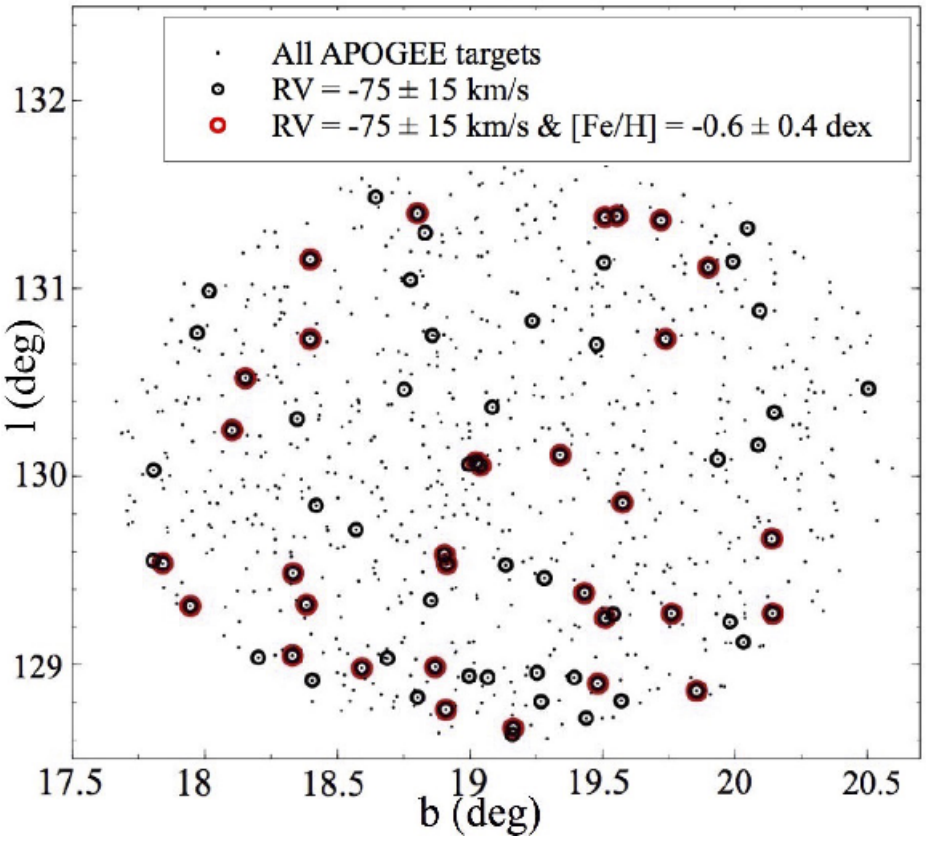

Figure 2.1: Position of each star from the APOGEE DR12 database in the Pal 1 field in Galactic coordinates. Those with heliocentric radial velocities and metallicities similar to those for Pal 1 are indicated by red circles. Note that the half-light radius is 0.007 deg, which is smaller than size of the overlapping stars at the centre.

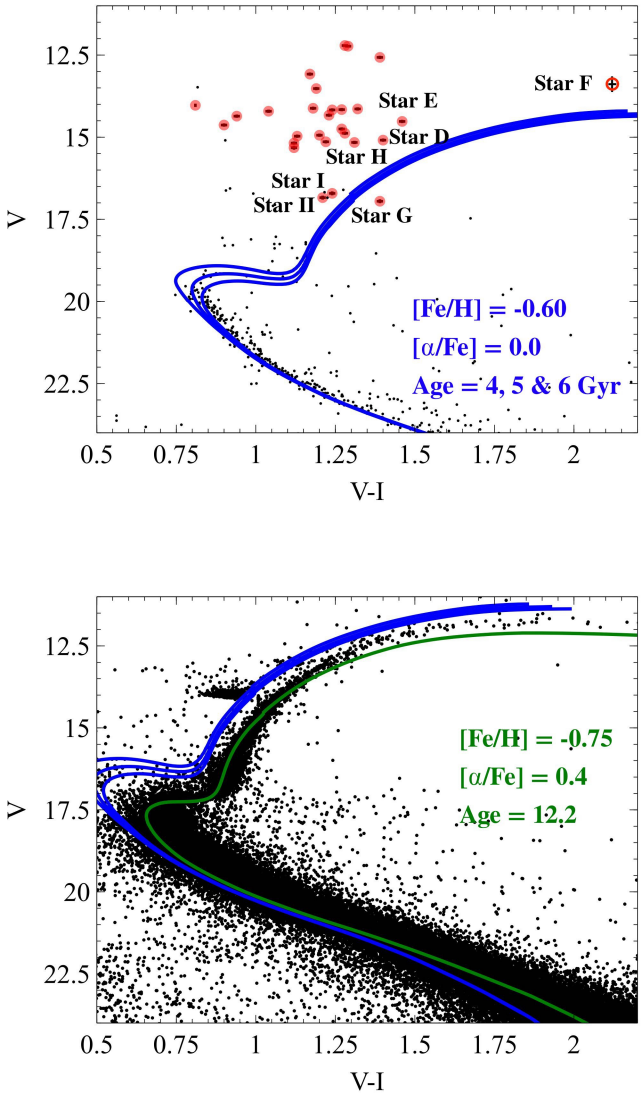

Figure 2.2: The top panel shows a colour-magnitude diagram for Pal 1 (from Sarajedini et al. 2007) with three isochrones for ages 4, 5 and 6 Gyr, from the Dartmouth Stellar Evolution Database (Dotter et al. 2008) and the bottom panel shows the colour-magnitude diagram of 47 Tuc (from Sarajedini et al. 2007) and an isochrone for age 12.2 Gyr as a reference for the position of the red giant branch in a typical globular cluster. Note that the distance modulus and reddening of 47 Tuc is applied to the isochrones of Pal 1 in the lower panel in order to compare age of the clusters. All of the APOGEE stars with velocities and metallicities similar to Pal 1 are shown by the red solid circles in the upper panel. The new Pal 1 candidate stars, and Stars I and II, are selected as those closest to the isochrones. Star F is denoted by an open red circle because it is flagged by SDSS as having unreliable photometric magnitudes ("*too few detection to be deblended*").

in New Mexico, covering the wavelength range from 1.5 to 1.7 microns in the H band, with spectral resolution R = 22,500 (Gunn et al. 2006). The APOGEE Stellar Parameters and Chemical Abundances Pipeline (ASPCAP) DR12 (Pérez et al. 2016) is a data analysis pipeline that produces stellar parameters and abundances for 15 different elements (C, N, O, Na, Mg, Al, Si, S, K, Ca, Ti, V, Mn, Fe and Ni).

APOGEE uses the same field size and target positioner as the Sloan Extension for Galactic Understanding and Exploration (SEGUE) of the Sloan Digial Sky Survey (SDSS). It uses a series of 7 squared degree tiles to sample the sky with 2" fibres that observe 300 targets simultaneously. One of these tiles was centred on Pal 1 (RA $=53.33^{o}$ & Dec $=79.58^{o}$, Harris 1996, 2010 edition) with fibers allocated to a variety of targets based on the colours of cool stars (see target selection for the APOGEE program by Zasowski et al. 2013). Foreground dwarfs are removed from our analysis, as well as objects that are unlikely to be associated with Pal 1 based on their metallicity and radial velocity. These include objects with radial velocities outside of -75 ± 15 kms^{-1} and metallicities outside of $-1.0 <$[Fe/H] < -0.2 (i.e., 4σ and 2σ of the values for confirmed Pal 1 members respectively, e.g., Rosenberg 1998, to account for errors in the APOGEE metallicities and potential kinematic effects along the tidal tails). These targets are shown in Fig. 2.1, where 9% of the stars in this field may be associated with Pal 1. Two of these are Stars I and II examined from optical spectra by Sakari et al. (2011). To further select Pal 1 members, we examine a colour-magnitude diagram (CMD) of stars in the central portion of Pal 1 from HST ACS photometry (Sarajedini et al. 2007); see Fig. 2.2. Isochrones are generated from the Dartmouth Stellar Evolution Database (Dotter et al. 2008) are included with ages of 4, 5 and 6 Gyrs, with the distance, reddening, and metallicity from Sarajedini et al. (2007), and adopting [α/Fe]=0. However, the APOGEE target selection provides Gunn ugriz and JHK magnitudes of the targets (Doi et al. 2010), requiring conversion to Johnson VI. We have adopted the calibration from Table 4 of Jordi et al. (2006) for Population I stars. [1]

The bottom panel in Fig. 2.2 shows the CMD of 47 Tuc and an isochrone generated from the Dartmouth Stellar Evolution Database (Dotter et al. 2008) with an age of 12.2 Gyr. The distance and metallicity are from Sarajedini et al. 2007, with

[1]The uncertainties are determined in quadrature given the uncertainties for each colour index listed in the APOGEE DR12 database and formulae by Jordi et al. (2006).

[α/Fe]=0.4 and E(B-V)=0.0 mag [2]. Comparing the CMD of Pal 1 to that of 47 Tuc in Fig. 2.2 clearly shows that Pal 1 is younger and more sparsely populated than a typical globular cluster.

The V and I magnitudes from this transformation for Stars I and II are in good agreement with those from the Sarajedini et al. (2007); see Table 2.1. An additional five stars (Stars D, E, F, G and H) with radial velocities and metallicities consistent with Pal 1 were selected from near the isochrones. We examine the stellar properties of these additional five stars below.

2.4 Stars I and II

The stellar parameters for Stars I and II are shown in Table 2.1, from the optical analysis by Sakari et al. (2011), and the IR analysis of the APOGEE spectra through the ASPCAP pipeline. These two sets of results are in very poor agreement, with differences of $\Delta T_{\rm eff} \sim 1000$ K and $\Delta \log g \sim 1.0$, resulting in differences in Δ[Fe/H] ~ -0.4.

In order to understand these differences, the individual visit spectra for these two stars are examined. There are 24 visits for Star I and 21 visits for Star II, with SNR > 6. We find a clear persistence problem in many of the spectra, in additional to some other effects such as poor flat fielding or telluric division problems, poor night sky line removal, and several cosmic ray hits.

2.4.1 Removing Persistence

Individual visits for Stars I and II were extracted from the APOGEE database. The alignment of each spectrum was compared to Arcturus, in order to check the radial velocity corrections, and the offsets are determined. Each visit was then broken into the three wavelength regions corresponding to the blue, green, and red detectors. Some of APOGEE's detectors suffered from persistence, which is the contamination of a spectrum by remnants of the previous exposure. The persistence problem is worse on the blue chip (1.514-1.581 μm), see Fig. 2.3. We remove the portion of the spectrum coming from the blue chip detector for any visit that shows persistence (i.e. continuum level difference of greater than two sigma between the blue and the green

[2]The reddening for 47 Tuc of E(B-V)=0.055 mag from Sarajedini et al. (2007) does not fit the turn-off well. When no reddening is applied, the fit is better (a lower reddening was similarly found by Schlafly & Finkbeiner 2011, E(B-V)=0.03 mag).

	APOGEE ID	RA (deg)	Dec (deg)	RV (kms^{-1})	T_{eff} (K)	log$g$ (dex)	[Fe/H] (dex)	[α/Fe] (dex)	V (mag)	I (mag)	(S/N)
Star D	2M03100079+7853325	47.503	78.892	−84.2	4957.7	2.69	−0.3	0.1	15.086	13.861	85.3
Star E	2M04023010+7935181	60.625	79.588	−78.4	4231.1	1.49	−0.7	0.1	14.522	13.664	151.2
Star F	2M03354183+7841453	53.924	78.696	−84.9	4847.7	2.56	−0.3	0.1	13.386	11.266	377.9
Star G	2M03070369+7933134	46.765	79.554	−62.0	4564.0	3.05	−0.5	0.2	16.955	15.562	68.7
Star H	2M03122767+7927416	48.115	79.462	−87.4	4856.8	2.75	−0.3	0.1	15.163	13.854	156.6
Star I	2M03332183+7935382	53.341	79.594	−75.2	5710.9	3.47	−0.2	0.1	16.705	15.461	83.6
Star II	2M03332960+7934162	53.373	79.571	−75.3	5602.4	3.22	−0.1	0.1	16.840	15.618	67.4
Star I	(Sakari et al. 2011)	53.341	79.589	−77.2	4800.0	2.27	−0.61	0.01	16.705	15.459	15
Star II	(Sakari et al. 2011)	53.373	79.571	−78.0	4750.0	2.33	−0.61	−0.10	16.675	15.618	15

Table 2.1: DR12 ASPCAP results for members and candidates of Pal 1

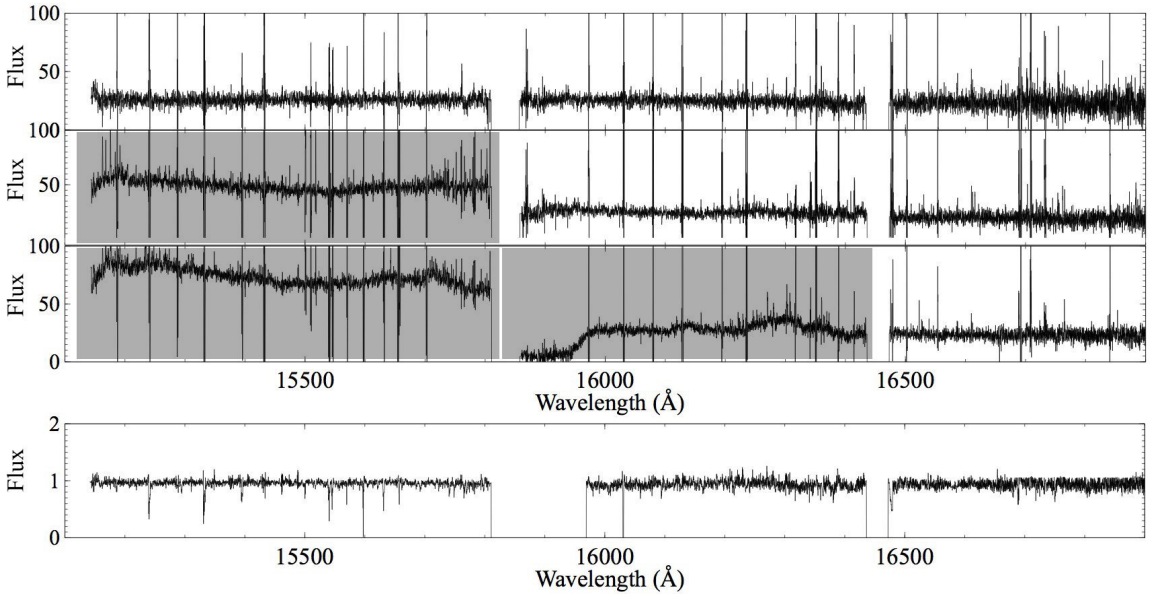

Figure 2.3: The top three panels are a sample of the spectra with no persistence problems (top), moderate persistence (middle), and strong persistence (or other flat fielding problems; bottom) for Star I (note the offsets and incongruities in the blue and the green chip spectra). All chips that would be removed in our analysis are shaded. The lower panel shows the final spectra after continuum normalization (see text) and removing sky lines.

Table 2.2: Details of each visit for members and candidates of Pal 1

Visit #	Visit ID	Derived Velocity (kms^{-1})	Offset (kms^{-1})	Chip A	Chip B	Chip C	S/N
Star I							
1	5283-55816-050	−73.8	−23	P	✓	✓	10.3
2	5282-55822-203	−74.8	−26	✓	✓	✓	8.5
3	5283-55823-050	−71.9	−25	P	P	✓	10.3
4	5282-55823-203	−73.7	−27	✓	✓	✓	15.3
5	5282-55841-161	−76.0	−25	✓	✓	✓	13.6
6	5283-55843-050	−73.1	−28	P	✓	✓	8.3
7	5283-55873-056	−77.2	−25	P	✓	✓	8.2
8	5283-55874-056	−75.2	−20	P	✓	✓	15.0
9	5283-55905-053	−76.5	−13	P	P	✓	13.6
10	5283-55906-053	−75.7	0	P	✓	✓	6.5
11	6246-56263-046	—	—	P	P	F	9.7
12	6247-56264-053	−76.6	−12	P	✓	✓	9.8
13	6247-56283-044	−76.7	0	P	P	✓	7.3
14	6363-56284-183	−75.0	0	✓	✓	✓	9.8
15	6364-56285-047	−76.7	0	P	P	✓	10.9
16	6246-56539-039	−75.3	−20	P	P	✓	6.1
17	6364-56561-038	−72.8	−17	P	P	✓	11.9
18	6363-56583-232	−76.4	−20	✓	F	✓	16.8
19	6364-56584-032	—	—	P	P	F	14.8
20	6363-56587-183	−74.0	−19	✓	✓	✓	14.7
21	6365-56608-182	−76.0	−20	✓	✓	✓	13.8
22	6365-56642-200	−75.8	0	✓	✓	✓	12.0
23	6366-56644-203	−73.8	−10	✓	✓	✓	12.5
24	6365-56676-203	−73.2	−2	✓	✓	✓	13.4
Star II							
1	5283-55816-053	−71.9	−17	P	✓	✓	9.1
2	5282-55822-204	−75.5	−19	✓	✓	✓	7.1
3	5283-55823-053	−71.4	−25	P	P	✓	7.7
4	5282-55823-204	−73.4	−27	✓	✓	✓	12.9
5	5282-55841-162	−75.1	−25	✓	✓	✓	12.4
6	5283-55843-053	−71.1	−25	P	✓	✓	8.4
7	5283-55873-059	−73.0	−25	P	✓	✓	7.2
8	5283-55874-059	−73.7	−22	P	P	✓	13.8
9	5283-55905-050	−74.4	−13	P	P	✓	11.0
10	6246-56263-047	—	—	RV	RV	RV	7.0
11	6247-56264-049	−76.2	−13	P	✓	✓	9.1
12	6247-56283-048	—	—	RV	RV	RV	9.1
13	6363-56284-182	−72.8	0	✓	F	O	8.9
14	6364-56285-044	−71.6	0	P	P	✓	7.2
15	6364-56561-041	—	—	RV	RV	RV	6.8
16	6363-56583-233	−74.9	−17	✓	F	O	13.5

Table 2.2

Visit #	Visit ID	Derived Velocity (kms^{-1})	Offset (kms^{-1})	Chip A	Chip B	Chip C	S/N
17	6363-56587-182	−72.1	−19	✓	✓	✓	11.8
18	6365-56608-181	−73.9	−18	✓	✓	✓	12.0
19	6365-56642-199	−72.3	0	✓	✓	✓	10.0
20	6366-56644-059	−75.0	−10	P	P	✓	11.2
21	6365-56676-204	−72.2	0	✓	✓	O	11.6
Star D							
1	5282-55815-010	−66.1	−30	P	✓	✓	5.4
2	5282-55822-010	−82.6	−30	✓	✓	✓	21.0
3	5282-55823-010	−83.8	−32	✓	✓	✓	35.8
4	5282-55841-004	−87.7	−33	✓	✓	✓	40.6
Star E							
1	6365-56608-154	−78.5	−20	P	✓	✓	68.2
2	6365-56642-165	−78.5	−10	✓	✓	✓	61.6
3	6365-56676-16	−78.2	0	✓	✓	✓	71.7
Star F							
1	6247-56264-148	−84.8	−20	✓	✓	✓	165.2
2	6247-56283-093	−84.8	−15	✓	✓	✓	170.5
3	6247-56541-099	−85.0	−34	✓	✓	✓	88.4
4	6247-56542-099	−85.1	−34	✓	✓	✓	110.3
Star G							
1	5282-55822-218	−64.0	−10	✓	✓	✓	7.2
2	5282-55823-218	−63.4	−10	✓	✓	✓	12.9
3	5282-55841-212	−63.9	−10	✓	✓	✓	9.5
4	5283-55816-013	−57.2	−10	P	✓	✓	7.3
5	5283-55823-019	−58.4	−10	P	✓	✓	8.5
6	5283-55843-013	−56.9	0	P	✓	✓	8.2
7	5283-55873-013	−61.2	−20	P	✓	✓	6.4
8	5283-55874-013	61.7	0	P	✓	✓	13.1
9	5283-55905-013	−64.9	10	P	✓	✓	11.2
10	5283-55906-013	−63.2	15	P	✓	✓	5.4
11	6246-56263-013	−63.1	5	P	✓	✓	10.4
12	6246-56282-019	−68.0	0	P	✓	✓	5.9
13	6246-56318-013	−72.5	15	P	✓	✓	5.3
14	6246-56539-013	−60.7	-5	P	✓	✓	5.8
15	6247-56264-216	−62.4	7	✓	✓	✓	11.1
16	6247-56283-216	−45.1	10	✓	✓	✓	11.7
17	6247-56541-211	−60.5	-10	✓	✓	✓	7.5
18	6247-56542-211	−63.1	−5	✓	✓	✓	8.6
19	6363-56284-013	−68.1	8	P	✓	✓	6.4
20	6363-56583-014	−63.6	−7	P	✓	✓	10.6
21	6363-56587-013	−62.6	5	P	✓	✓	9.5
22	6364-56285-018	−65.3	5	P	✓	✓	8.2
23	6364-56561-019	−59.9	−10	P	✓	✓	9.6
24	6364-56584-013	−63.2	−5	P	✓	✓	9.5
25	6365-56608-013	−64.1	0	P	✓	✓	9.1
26	6365-56642-018	−60.9	10	P	✓	✓	8.9
27	6365-56676-018	−65.8	0	P	✓	O	8.7
28	6366-56644-013	−62.2	10	P	✓	✓	8.2
Star H							
1	5282-55815-214	−87.7	−30	✓	✓	✓	6.1
2	5282-55822-214	−87.6	−35	✓	✓	✓	26.5
3	5282-55823-214	−87.4	−34	✓	✓	✓	45.5
4	5282-55841-232	−87.4	−35	✓	✓	✓	40.4
5	5283-55816-016	−87.5	−36	P	✓	✓	25.3
6	5283-55823-022	−87.0	−35	P	✓	✓	33.9
7	5283-55843-016	−86.8	−33	P	✓	✓	30.4
8	5283-55873-016	86.8	−27	✓	✓	✓	26.7
9	5283-55874-016	−87.3	−26	P	✓	✓	47.5
10	5283-55905-015	−87.7	-20	P	✓	✓	35.4
11	5283-55906-015	−87.5	−20	P	✓	✓	17.1

Note. P = persistence, F = flat problems, RV = incorrect RV, Offset = the offset with respect to the high resolution radial velocity corrected spectrum of Arcturus (Hinkle et al. 2003) and O = other problems related to SNR or large noise spikes or poor night sky line removal.

regions). Occasionally it was also necessary to remove the green chip spectrum - we suspect that the green chip itself does not have the persistence problem, but that the data reduction processing of the visit induces a flat fielding problem when persistence is bad on the blue chip. After this process, the remaining spectra from each visit are co-added, i.e., only the non-persistence spectra from the blue, green, and red regions are kept for our analysis.

The non-persistence regions of each visit were combined to create the full wavelength range visits, and the cleaned visits were median-combined using IRAF. The final combined spectra for Stars I and II tend to have fewer green spectra than red, and fewer blue than either. This results in a lower SNR for the green than red spectrum, and lowest SNR for the blue spectrum. These spectra were then normalized with a Legendre polynomial (order=8), followed by a k-sigma clipping routine (see Venn et al. 2012), and sky lines are removed. These steps are illustrated in Fig. 2.3. Since these stars are moderately metal-poor, we found this normalization method to be sufficient for our purposes, but we caution that this is not the same as that used by the ASPCAP pipeline. Stars G and H also have significant persistence on their spectra. We have cleaned them similar to Stars I and II. Stars D, E and F did not have significant persistence problems. These gave us an opportunity to use and test ASPCAP on the original spectra in the APOGEE database.

In Fig. 2.4, a portion of the cleaned and combined spectra of our Pal 1 members to that of Arcturus are compared. APOGEE spectra have R=22,500 whereas the Arcturus spectrum from (Hinkle et al. 2003) was convolved with a Gaussian profile to match the lower resolution and has R=24,000.

Star G shows broader lines than Arcturus and the other spectra in our sample, which suggests that it is a dwarf star[3].

In Fig. 2.4, the CN, OH, Mg I, Al I, Si I, and Fe I features in our candidate spectra are highlighted and compared to the Arcturus spectrum. Stars I and II exhibit weaker spectral lines for these species than Arcturus, which can be attributed to their higher surface temperatures. The aforementioned line broadening observed in Star G is present in these spectral ranges as well.

[3] The newest APOGEE DR13 grids for dwarfs include rotation models and therefore log g of Star G is removed in the new data release, which supports our claim that Star G is a dwarf star.

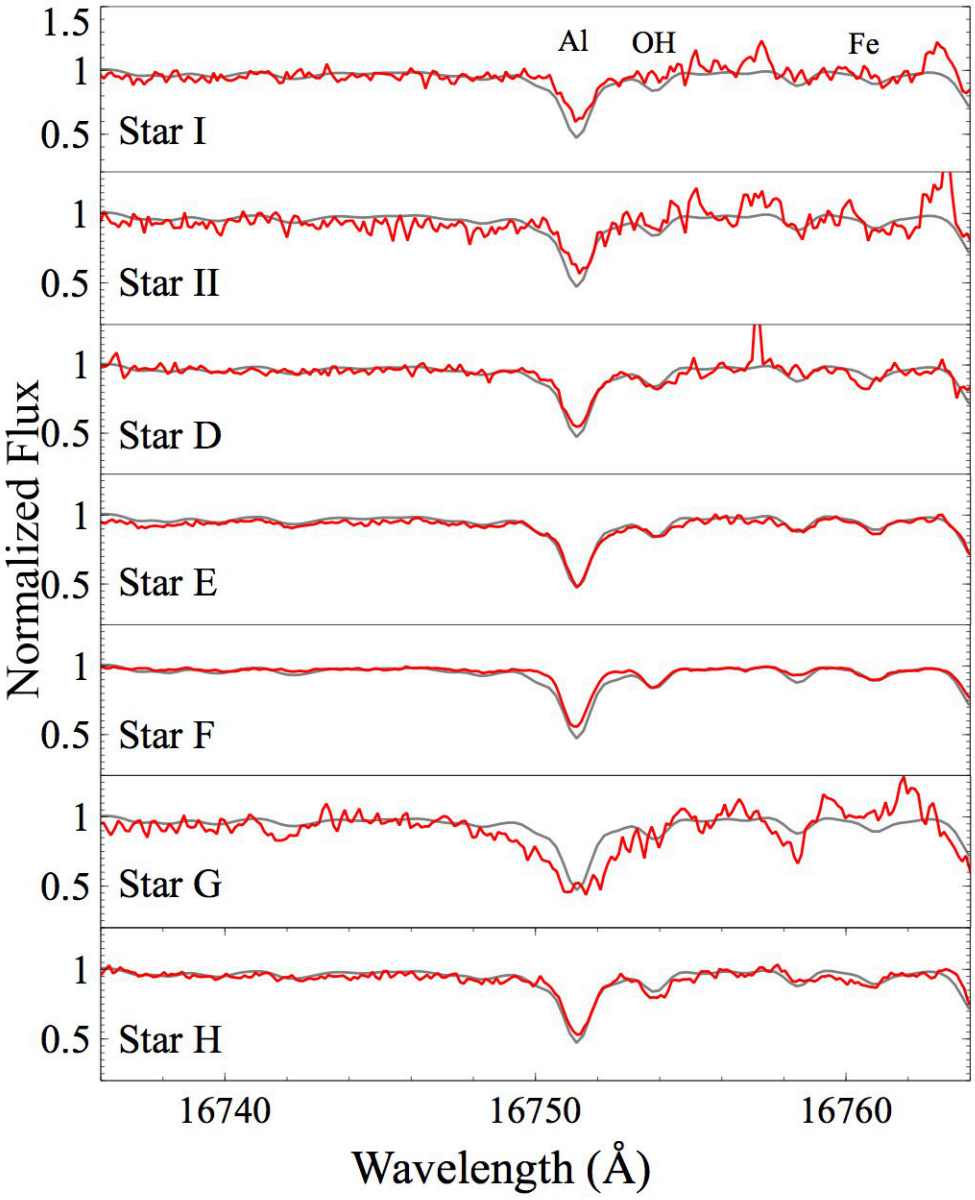

Figure 2.4: Comparing Pal 1 member and candidate spectra (red) to Arcturus (grey). All spectra have been shifted to the Arcturus wavelength scale. Lines of Fe I, Mg I, Al I, Si I, OH and CN are labelled.

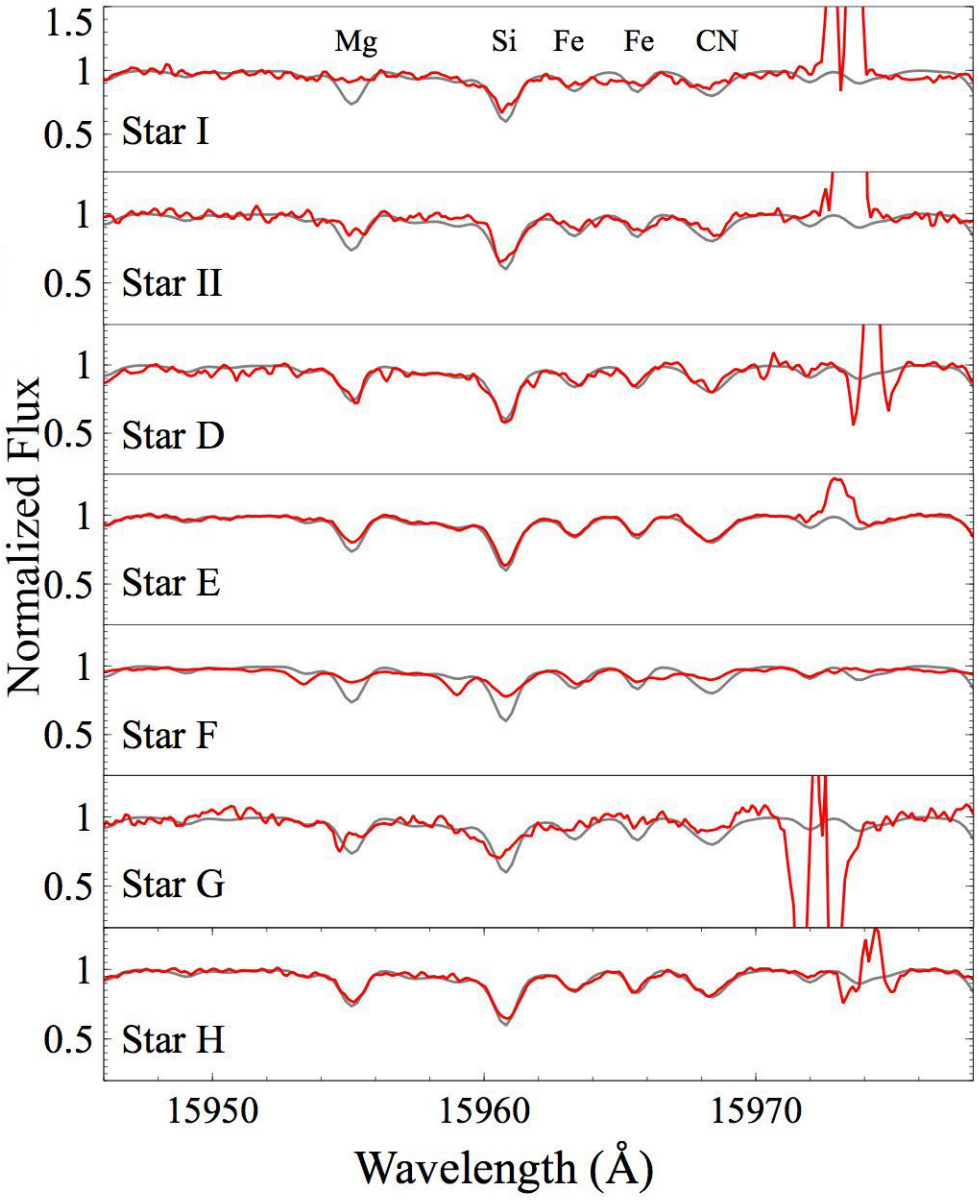

Figure 2.5: Comparing Pal 1 member and candidate spectra (red) to Arcturus (grey). All spectra have been shifted to the Arcturus wavelength scale. Lines of Fe I, Mg I, Al I, Si I, OH and CN are labelled.

2.5 New Stellar Analysis

We have carried out a new analysis for all of the stars that may be members of Pal 1 based on the DR12 data. This includes those stars that have a persistence problem, but also those that do not so that we treat the data for all of these objects in a similar way. New stellar parameters are determined, initially from optical and IR photometry using both the Casagrande et al. (2010) and Ramírez & Meléndez (2005), colour-temperature relationships. Temperatures and bolometric corrections are determined from the unweighted average of four colours: (B-V), (V-I), (V-K), and (J-K), adopting the metallicity and cluster distance for Pal 1 from Sarajedini et al. (2007). Reddening estimates are from Schlafly & Finkbeiner (2011). Surface gravities are determined photometrically as in Venn et al. (2012), after adopting a cluster turn-off mass of MA=1.14$M_{\odot}$ (Sakari et al. 2011) corresponding to its young age, such that:

$$logg = 4.44 + log(MA) + 4log(\frac{T_{\rm eff}}{5790}) + 0.4(M_{\rm bol} - 4.75)$$

The $T_{\rm eff}$ values determined from the two different colour-temperature calibrations were in excellent agreement for all of the candidates, with the exception of Star F. For this one star, the temperatures differed by $\Delta T_{\rm eff} \sim 1200$ K (see Table 2.3). The temperature from Casagrande et al. (2010) is much higher, and inconsistent with the position of this star on the colour-magnitude diagram in Fig. 2.2; however, the position of Star F in Fig. 2.2 depends on a correct V magnitude, which has been flagged in the SDSS database. Without further information on the V magnitude of Star F, we consider both temperatures in the discussion below. The difference between the log$g$ values for two different distance moduli from Harris (1996, 2010 edition) and Sarajedini et al. (2007) is Δ log$g \sim 0.4$, which causes only small to negligible differences in our abundance results.

The APOGEE ASPCAP data analysis pipeline uses the least squares template fitting routine, FERRE (Prieto et al. 2006), which matches observed spectra to (renormalized) synthetic spectra from model atmospheres that have been run through the 1D, LTE, spectrum synthesis code ASSET FERRE simultaneously determines the stellar parameters, metallicities, and element abundance ratios for a given spectrum. We too have used FERRE[4] for metallicities and chemical abundances, once where

[4]FERRE at Github: https://github.com/jobovy/apogee.

Table 2.3: Photometric Stellar Parameters

	T_{bv} (K)	T_{vi} (K)	T_{vk} (K)	T_{jk} (K)	$T_{\rm eff}$ (K)	log$g$
Star I	4930	4939	4872	4481	4806	2.27
Star II	5032	5015	4887	—	4978	2.33
Star D	4611	4635	4582	4660	4622	1.55
Star E	4516	4554	4415	—	4495	1.22
Star F	4787	—	—	5199	4993	1.64
Star F*	—	3800	3934	—	3867	0.43
Star G	4620	4632	4775	4670	4674	2.28
Star H	4787	4805	4826	4847	4816	1.47

Note. $T_{\rm eff}$ of Star F* is calculated using Ramírez & Meléndez (2005) calibration and the rest are computed using Casagrande et al. (2010) calibration.

Table 2.4: Different Properties of the candidates using FERRE

	DR12	DR13	FERRE*	Photom*	Sakari et al. (2011)
Star I					
T_{eff} (K)	5711	5203	4806 ± 92	4806 ± 218	4800 ± 70
log$g$	3.5	2.7	2.8	2.3 ± 0.2	2.27 ± 0.15
[FeI/H]	−0.2	−0.4	−0.8 ± 0.1	−0.6 ± 0.0	−0.61 ± 0.08
[α/Fe]	0.1	0.2	—	0.1 ± 0.1	0.00 ± 0.00
[C/Fe]	−0.2	—	0.5 ± 0.2	< 0.1	—
[Ca/Fe]	0.4	−0.4	0.3 ± 0.2	0.2 ± 0.1	0.16 ± 0.16
[S/Fe]	-0.3	—	0.6 ± 0.2	0.2 ± 0.1	—
[O/Fe]	1.0	0.8	0.2 ± 0.4	0.4 ± 0.1	<0.82
[Mg/Fe]	−0.1	0.1	−0.3 ± 0.3	−0.1 ± 0.2	−0.11 ± 0.20
[Mn/Fe]	0.0	−0.2	0.9 ± 0.1	−0.1 ± 0.1	—
[Si/Fe]	0.3	0.1	−0.1 ± 0.1	0.1 ± 0.2	0.24 ± 0.24
[Al/Fe]	—	—	0.1 ± 0.1	0.1 ± 0.2	—
[K/Fe]	—	—	0.1 ± 0.1	0.1 ± 0.1	—
Star II					
T_{eff} (K)	5602	4886	4936 ± 92	4978 ± 79	4750 ± 135
log$g$	3.2	2.3	2.7	2.3 ± 0.2	2.33 ± 0.15
[FeI/H]	−0.1	−0.5	−0.5 ± 0.2	−0.6 ± 0.0	−0.61 ± 0.08
[α/Fe]	0.1	0.2	—	0.1 ± 0.1	−0.10 ± 0.00
[C/Fe]	−0.3	—	0.1 ± 0.2	< 0.2	—
[Ca/Fe]	0.3	−0.3	0.4 ± 0.2	0.2 ± 0.3	−0.04 ± 0.22
[S/Fe]	−0.6	—	0.0 ± 0.2	0.2 ± 0.1	—
[O/Fe]	−0.1	0.7	0.1 ± 0.1	0.2 ± 0.1	<0.32
[Mg/Fe]	−0.6	0.0	−0.2 ± 0.2	−0.1 ± 0.1	−0.13 ± 0.30
[Mn/Fe]	0.0	−0.1	0.5 ± 0.1	−0.1 ± 0.1	−0.16 ± 0.36
[Si/Fe]	0.2	0.2	0.1 ± 0.2	0.2 ± 0.1	0.13 ± 0.23
[Al/Fe]	0.0	—	−0.3 ± 0.1	−0.1 ± 0.1	—
[K/Fe]	−0.8	—	0.0 ± 0.1	0.2 ± 0.1	—

* This use of "FERRE" is on our persistence cleaned spectra, allowing FERRE to simultaneously determine the stellar parameters and chemical abundances, whereas "Photom" uses our photometrically determined stellar parameters.

Table 2.5: Different Properties of the candidates using FERRE

	DR12	DR13	FERRE*	Photom*
Star D				
T_{eff} (K)	4958	4843	4870 ± 92	4622 ± 33
log$g$	2.7	2.6	2.8 ± 0.1	1.6 ± 0.2
[FeI/H]	−0.3	−0.3	−0.4 ± 0.1	−0.6 ± 0.0
[α/Fe]	0.1	0.1	—	0.1 ± 0.1
[C/Fe]	0.3	—	0.3 ± 0.2	0.1 ± 0.1
[Ca/Fe]	0.3	0.3	0.4 ± 0.1	0.2 ± 0.2
[S/Fe]	0.1	—	0.1 ± 0.1	0.1 ± 0.1
[O/Fe]	0.0	0.5	−0.1 ± 0.4	0.3 ± 0.1
[Mg/Fe]	0.2	0.0	0.2 ± 0.1	−0.2 ± 0.1
[Mn/Fe]	−0.2	−0.1	0.4 ± 0.1	−0.1 ± 0.1
[Si/Fe]	0.2	0.2	0.1 ± 0.1	0.1 ± 0.1
[Al/Fe]	−0.7	—	−0.6 ± 0.1	0.4 ± 0.1
[K/Fe]	−0.4	—	−0.2 ± 0.1	−0.2 ± 0.1
Star E				
T_{eff}	4231	4138	4168 ± 92	4495 ± 72
log$g$	1.5	1.3	1.9 ± 0.1	1.2 ± 0.15
[FeI/H]	−0.7	−0.6	−0.6 ± 0.1	−0.6 ± 0.0
[α/Fe]	0.1	0.1	—	0.2 ± 0.1
[C/Fe]	0.0	—	−0.1 ± 0.0	0.1 ± 0.1
[Ca/Fe]	0.0	0.1	0.0 ± 0.1	0.2 ± 0.2
[S/Fe]	0.2	—	0.1 ± 0.1	0.2 ± 0.5
[O/Fe]	−0.2	0.1	0.1 ± 0.1	0.5 ± 0.1
[Mg/Fe]	−0.3	0.1	0.0 ± 0.1	0.3 ± 0.1
[Mn/Fe]	0.0	−0.1	0.6 ± 0.0	0.0 ± 0.2
[Si/Fe]	−0.2	0.1	0.2 ± 0.1	0.0 ± 0.1
[Al/Fe]	0.2	—	0.3 ± 0.1	0.3 ± 0.0
[K/Fe]	0.0	—	0.0 ± 0.1	0.0 ± 0.1
Star G				
T_{eff} (K)	4564	4472	4425 ± 92	4674 ± 70
log$g$	3.1	—	4.6 ± 0.1	2.3 ± 0.2
[FeI/H]	−0.5	0.0	−0.2 ± 0.1	−0.6 ± 0.0
[α/Fe]	0.2	0.1	—	—

Table 2.5

	DR12	DR13	FERRE*	Photom*
[C/Fe]	0.5	—	0.2 ± 0.1	< 0.2
[Ca/Fe]	—	0.0	0.0 ± 0.1	—
[S/Fe]	0.0	—	-0.8 ± 0.2	—
[O/Fe]	0.3	0.1	0.1 ± 0.1	0.1 ± 0.1
[Mg/Fe]	0.2	0.1	0.4 ± 0.1	0.8 ± 0.1
[Mn/Fe]	−0.7	−0.1	0.2 ± 0.1	-0.1 ± 0.3
[Si/Fe]	−0.0	0.2	0.3 ± 0.1	0.2 ± 0.1
[Al/Fe]	—	—	$0.0 \pm$ —	< 0.7
[K/Fe]	−0.1	—	0.2 ± 0.2	< 0.7
Star H				
T_{eff} (K)	4857	4800	4780 ± 92	4816 ± 26
log$g$	2.8	2.9	3.1 ± 0.1	1.5 ± 0.2
[Fe/H]	−0.3	−0.3	-0.3 ± 0.1	-0.4 ± 0.0
[α/Fe]	0.1	0.1	—	0.2 ± 0.1
[C/Fe]	0.2	—	-0.1 ± 0.1	0.2 ± 0.1
[Ca/Fe]	0.2	0.1	0.0 ± 0.0	0.1 ± 0.0
[S/Fe]	−0.2	—	0.4 ± 0.1	0.2 ± 0.1
[O/Fe]	0.1	0.3	0.1 ± 0.2	0.2 ± 0.1
[Mg/Fe]	0.2	0.2	0.1 ± 0.1	0.5 ± 0.1
[Mn/Fe]	−0.2	-0.1	0.3 ± 0.0	0.1 ± 0.2
[Si/Fe]	0.2	0.1	0.1 ± 0.1	0.1 ± 0.1
[Al/Fe]	0.0	—	$-0.2 \pm$ —	0.3 ± 0.1
[K/Fe]	−0.3	—	0.0 ± 0.1	0.0<

* This use of "FERRE" is on our persistence cleaned spectra, allowing FERRE to simultaneously determine the stellar parameters and chemical abundances, whereas "Photom" uses our photometrically determined stellar parameters.

Table 2.6: Different Properties of Star F

	DR12	DR13	FERRE*	Photom1*	Photom2*
Star F					
T_{eff} (K)	4848	4828	4875 ± 92	4993 ± 291	3867 ±95
log$g$	2.6	2.5	3.2 ± 0.1	1.6 ± 0.2	0.4 ± 0.2
[Fe/H]	−0.3	−0.4	−0.8 ± 0.1	−0.6 ± 0.1	−1.4 ±0.1
[α/Fe]	0.1	0.1	—	−0.3 ± 0.3	—
[C/Fe]	−0.1	—	0.4 ± 0.3	0.3 ± 0.1	−0.1 ±0.1
[Ca/Fe]	−0.1	0.0	0.0 ± 0.1	−0.3 ± 0.1	—
[S/Fe]	0.2	—	−0.1 ± 0.2	−0.4 ± 0.1	−0.2 ± 0.1
[O/Fe]	0.1	0.1	−0.1 ± 0.3	−0.2 ± 0.2	0.0 ± 0.1
[Mg/Fe]	0.0	0.1	0.2 ± 0.1	−0.3 ±0.2	−0.5 ± 0.1
[Mn/Fe]	0.1	0.0	0.8 ± 0.0	0.3 ± 0.2	0.3 ± 0.1
[Si/Fe]	0.2	0.1	0.0 ± 0.0	−0.1 ± 0.2	0.0 ± 0.1
[Al/Fe]	0.2	—	0.6 ± 0.0	0.8 ± 0.1	0.8 ± 0.1
[K/Fe]	−0.1	—	−0.1 ± 0.1	0.1 ± 0.1	−0.2 ±0.1

* This use of "FERRE" is on our persistence cleaned spectra, allowing FERRE to simultaneously determine the stellar parameters and chemical abundances. For Star F, we found two very different temperatures depending on which set of photometric magnitudes were examined; see Table 2.3. Here we present the elemental abundances for each temperature.

FERRE determines the stellar parameters and a second time where we adopt our photometrically determined stellar parameters (see Tables 2.4-2.6). To match the observed spectra to the synthetic spectra, it was necessary to resample the observations to be on the same wavelength scale. This caused the observations to have a slightly lower resolution than the original visits, and the combined spectra had a slightly larger spectral range. This resulted in observations of a few additional absorption lines (K, Mn) that that are not in the APOGEE DR12 database.

For Stars I and II, Table 2.4 shows that the photometric stellar parameters yield chemical abundances and metallicities in excellent agreement with the optical analyses. This implies that persistence is a significant problem in the analysis of these two stars in the DR12 data release (also see discussion of the DR13 data in Section 2.7.4). This further implies that the analysis of some stars in the APOGEE database can still be improved using the APOGEE spectra themselves.

2.6 Stellar Abundances

The stellar parameters and chemical abundances for 10 elements have been redetermined in this paper for in a set of Pal 1 members and candidates from persistence-cleaned APOGEE spectra. The results are shown in Tables 2.4-2.6, including the elements C, O, Mg, Al, Si, S, K, Ca, Mn, and Fe (see Table 2.7 for log abundances of all detected lines).

The abundance uncertainties are calculated in two ways. When fewer than four lines are available, the error is taken as the standard deviation in [Fe/H]. When there are more than four lines, the measurement error is taken as the standard deviation divided by root of number of lines. For cases where either of these methods results in an error < 0.1 dex, an error of 0.1 dex is adopted since the best synthetic fits have been determined by eye.

A few elements require special notes:

- Titanium: Holtzman et al. (2015) show that the APOGEE (DR12) abundances do not reproduce the [Ti/Fe] trends seen for stars in the solar neighbourhood by Bensby et al. (2014). This difference is not currently understood, and therefore the ASPCAP titanium lines are to be treated with caution. Hawkins et al. (2016) suggested that the Ti line at 15837.8Å, which is not included in the set adopted by ASPCAP, can be considered reliable. We did not use this line in our FERRE estimates.

- [α/Fe]: We estimate a mean [α/Fe] ratio by averaging the results for Mg, S, Si and Ca (not O due to the very noisy oxygen lines, and not Ti as discussed above).

Overall, the chemical abundances of Stars I and II are in a good agreement with the optical analysis by Sakari et al. (2011). Three candidate stars (Stars D, E, and G) have stellar parameters typical of red giants and metallicities of [Fe/H]=−0.6, when determined from the photometric parameters. These values are similar to the members in the core of Pal 1. On the other hand, the chemistry of Star H is sufficiently different that it is a likely non-member.

Star F warrants special attention due to its position in the tidal tails of Pal 1. Two temperatures have been determined from the colour-temperature calibrations for this star, based on its photometric uncertainties (see Table 2.3). When the cooler temperature is examined, then its metallicity is significantly different from that of Pal 1 such that it would be a non-member. However, if the hotter temperature is adopted, its stellar parameters are typical of a red giant, with a metallicity and chemical abundances that are similar to those of the members of Pal 1. Furthermore, with the hotter temperature, then Star F has a low [α/Fe] that is consistent with the other members of Pal 1. Its high [Al/Fe], with slighly low [Mg/Fe], is unusual for a star in Pal 1, unless Star F is, or has been contaminated by, an AGB star (e.g., Ventura & D'Antona 2008).

2.7 Discussion

Using the APOGEE database, we have re-examined the spectra for two known members of Pal 1 and five new candidate members that are well away from the central region of this cluster. For each member and candidate star, all visits were examined and the blue chips of the spectra with persistence removed, then recombined the clean visits (see section 2.4.1 for more details). A new stellar analysis has been conducted using FERRE. The results for the cleaned spectra of Stars I and II are in excellent agreement with the optical analysis by Sakari et al. (2011), whereas the DR12 analyses based on the original spectra are not (see Table 2.1). The chemical abundance and stellar parameters of the candidates are shown in Table 2.4-2.6. The estimated [α/Fe] ratios for Stars I and II are in good agreement with the optical results of Sakari et al. (2011). The Na I lines are too weak or noisy in most of the spectra for reliable determinations of [Na/Fe], therefore we do not investigate the Na-O anticorrelation.

Table 2.7: Atomic line data and FERRE [X/Fe][a] ratios

Element	Lambda (Å)	Star I	Star II	Star D	Star E	Star F	Star F*	Star G	Star H
Fe I	15211.682	−1.0	−0.6	—	−0.7	−1.0	<−1.7	−0.6	−0.4
	15249.140	−0.6	−0.6	−1.0	−0.7	−0.6	−1.3	−0.4	−0.4
	15297.317	−0.4	>−0.4	>−1.0	−0.7	—	—	—	−0.2
	15309.789	—	—	—	∼-0.8	−0.4	—	—	−0.2
	15339.574	−0.8	−0.6	−0.9	−0.6	−1.0	<−1.8	−0.4	−0.2
	15392.011	−0.8	−0.6	−0.8	−0.6	−0.6	<−1.8	−0.8	−0.6
	15483.107	−0.6	−0.4	—	−0.6	—	—	—	−0.2
	15494.762	−0.6	−0.6	−0.6	−0.6	−0.6	—	—	−0.4
	15505.316	—	—	−0.6	−0.6	−0.6	−1.4	−0.6	−0.4
	15528.553	—	—	−0.4	−0.7	—	—	—	—
	15546.326	—	—	>−0.9	−0.5	−0.6	−1.4	−0.4	—
	15595.760	−0.8	−0.6	−1.0	−0.7	<−0.8	−1.6	—	−0.3
	15608.487	−0.8	−0.8	>−1.0	−0.8	−0.6	−1.6	−0.6	−0.4
	15615.412	—	−0.6	—	—	—	<−1.8	−0.6	−0.6
	15666.296	−0.8	−0.8	—	−0.7	<−0.7	<−1.8	−0.5	−0.6
	15681.805	−0.7	−0.4	−1.0	−0.6	−0.6	—	−0.5	−0.4
	15735.713	—	—	—	—	—	—	—	—
	15765.622	—	—	—	−0.4	−0.6	—	—	−0.2
	15778.381	−0.4	−0.6	−1.0	−0.5	−0.6	−1.2	—	−0.4
	15899.571	−0.6	—	−0.4	>−0.4	—	—	−0.5	−0.4
	15905.797	−0.6	—	−0.4	−0.4	—	—	—	−0.4
	15910.390	−0.6	−0.4	−0.4	−0.5	−0.8	—	—	−0.4
	15924.987	−0.7	−0.5	−0.4	−0.7	−0.6	−1.3	—	−0.4
	15946.207	—	—	−0.4	−0.8	−0.6	−1.6	—	−0.5
	15958.447	<−0.8	−0.6	−0.4	−0.6	—	<−1.4	−0.7	−0.2
	15969.209	−0.8	−0.8	−0.6	<−0.8	—	—	−0.8	−0.6
	15975.615	—	—	—	—	−0.4	—	—	—
	16011.133	−0.6	−0.6	−0.4	−0.8	—	−1.4	>−0.4	−0.6
	16013.985	−0.6	−0.6	−0.4	−0.8	—	—	>−0.4	−0.6
	16080.311	−0.5	−0.6	—	−0.6	−0.6	<−1.8	—	−0.6
	16130.274	−0.8	−0.6	—	−0.6	−0.8	−1.4	—	−0.4
	16157.660	−0.6	−0.4	−0.4	−0.6	−0.6	−1.4	−0.4	−0.4
	16169.448	−0.6	−0.5	−0.8	−0.7	−0.8	−1.6	>−0.4	−0.2
	16190.224	−0.6	−0.4	−1.0	−0.8	−0.6	—	—	−0.6
	16212.175	−0.7	−0.4	−0.8	−0.6	−0.8	—	−0.8	−0.4
	16217.970	−0.4	−0.4	−0.8	−0.7	—	−1.2	−0.4	−0.4
	16236.084	−0.8	−0.6	—	−0.7	−0.8	<−1.8	—	−0.6
	16240.487	—	—	—	—	—	<−1.8	−0.4	—
	16256.993	—	—	−0.4	<−0.8	−0.6	—	—	—
	16297.294	−0.6	—	—	−0.8	−0.6	−1.4	−0.4	−0.6
	16320.829	—	—	−0.8	−0.6	−0.8	−1.5	—	−0.6
	16328.912	−0.7	−0.4	−0.4	−0.8	−0.8	<−1.4	—	−0.6
	16402.650	−0.6	−0.6	−0.8	−0.8	—	<−1.8	−0.6	−0.6
	16409.869	—	—	—	—	—	—	—	—
	16510.805	−0.6	−0.4	−0.8	−0.6	—	−1.4	−0.4	−0.6
	16521.738	−0.5	−0.6	−0.4	−0.6	−0.4	>1.4	>−0.4	−0.2
	16536.502	−0.6	—	−0.6	−0.6	−0.4	−1.4	−0.6	−0.4
	16556.519	−0.6	−0.5	−0.4	−0.6	−0.3	—	—	−0.4
	16590.582	—	—	—	—	—	—	—	—
	16617.302	—	—	>−1.0	<−0.8	—	<−1.8	−0.6	<−0.6
	16624.278	—	—	−1.0	−0.7	—	—	—	−0.6
	16650.424	−0.4	−0.4	−0.6	−0.6	−0.3	−1.4	>−0.4	−0.4
	16670.037	>−0.4	>−0.4	−0.8	−0.3	−0.3	−1.4	—	−0.4
	16757.644	—	−0.8	−0.4	−0.6	−0.3	—	—	−0.2
	16804.240	—	—	−0.4	−0.6	—	—	—	−0.4
	16848.118	—	—	−0.8	<−0.8	—	<−1.8	—	—
O from OH lines	15241.164	—	—	—	0.0	—	—	—	0.2
	15396.206	—	—	—	—	−0.2	—	—	0.4
	15413.211	0.4	0.2	0.5	>0.5	<−0.2	—	—	0.2
	15509.737	—	—	0.2	>0.5	—	<−0.2	0.1	0.3
	15564.252	—	0.2	0.1	0.3	−0.4	—	0.2	<−0.2

Table 2.7

Element	Lambda (Å)	Star I	Star II	Star D	Star E	Star F	Star F*	Star G	Star H
	15573.254	—	—	0.2	0.7	—	—	—	0.4
	15576.255	—	—	—	0.7	<0.0	—	—	—
	15631.270	—	—	—	0.7	—	—	—	—
	16056.386	0.5	—	—	0.7	—	—	—	−0.2
	16065.388	0.5	0.2	0.2	−0.2	−0.3	0.0	0.2	−0.2
	16069.389	—	—	—	—	—	—	—	0.4<
	16196.424	—	—	—	—	—	—	—	—
	16256.440	—	—	—	—	—	—	0.0	—
	16264.442	—	—	—	—	—	—	—	—
	16350.466	0.5	0.2	0.5	0.3	0.2	—	—	0.2
	16356.467	—	—	—	—	—	—	—	—
	16358.467	—	0.5	0.4	0.3	<0.2	—	—	—
	16372.472	>0.6	—	0.2	0.7	—	<−0.2	—	—
	16530.515	—	—	—	—	—	<−0.2	—	—
	16539.517	>0.6	—	>0.2	0.7	—	—	—	0.2
	16543.518	—	—	—	—	—	0.0	0.2	—
	16708.563	0.5	—	0.2	0.7	—	<−0.2	—	0.4
	16718.566	>0.5	0.5	0.5	0.7	—	<−0.2	—	0.4
C from CO lines	15325.187	—	<0.1	0.1	—	—	—	—	0.2
	15367.243	—	—	< 0.2	0.1	0.2	—	< 0.2	−0.1
	15470.226	—	—	—	—	0.4	—	—	0.2
	15499.690	—	<0.0	—	—	—	—	—	0.2
	16186.421	< 0.0	<0.2	0.1	0.0	—	—	—	—
	16193.923	—	—	—	—	0.2	—	—	0.0
MgI	15745.017	0.0	0.0	−0.2	0.1	−0.2	−0.2	0.8	0.5
	15753.189	−0.2	−0.1	−0.1	0.3	−0.5	−0.6	0.8	0.5
	15770.150	−0.3	−0.2	−0.4	0.3	—	−0.6	0.7	0.5
	15958.836	—	0.1	0.3	0.2	−0.2	—	<0.4	0.3
MnI	15222.009	−0.1	<0.0	−0.2	0.1	0.4	0.3	0.2	0.2
	15791.657	—	—	0.0	0.0	—	<0.0	—	—
	15969.543	—	−0.1	−0.2	−0.2	0.1	0.2	−0.3	−0.1
CaI	16161.778	0.2	0.4	0.3	0.2	−0.2	—	—	0.1
	16208.514	<0.0	0.0	0.4	0.3	−0.4	—	—	—
	16213.018	—	—	0.0	0.0	—	—	—	—
SI	15426.404	0.2	<0.1	0.0	0.6	—	—	—	0.2
	15474.047	—	—	—	0.0	−0.3	−0.2	—	0.1
	15482.710	0.1	0.2	0.2	−0.2	−0.5	—	—	0.3
AlI	16723.527	−0.1	−0.1	0.4	0.3	0.8	0.8	<0.7	0.3
	16767.939	0.2	<0.2	0.4	0.3	0.7	0.8	—	0.3
KI	15172.521	0.1	0.2	−0.2	0.0	0.1	−0.2	0.7	>0.0
NaI	16378.326	—	—	—	>0.1	—	—	—	—
	16393.327	—	—	—	—	>−0.4	<−0.4	—	—
SiI	15562.031	<−0.2	0.2	—	0.2	—	—	0.2	—
	16055.585	—	—	—	—	—	—	—	—
	16064.397	−0.2	0.0	0.0	−0.2	—	—	—	0.0
	16099.184	<−0.2	0.2	0.4	0.0	−0.4	−0.4	<0	0.2
	16185.583	−0.2	—	0.0	0.2	—	—	0.0	0.1
	16191.217	—	—	—	—	—	—	—	—
	16220.100	0.0	0.2	−0.1	−0.2	−0.4	−0.4	0.0	0.2
	16685.327	0.2	0.2	0.2	0.0	0.4	0.4	0.2<	0.2
	16832.756	0.0	—	0.2	0.0	0.4	0.4	0.2	0.0

[a] [X/H] is given instead for Fe I.

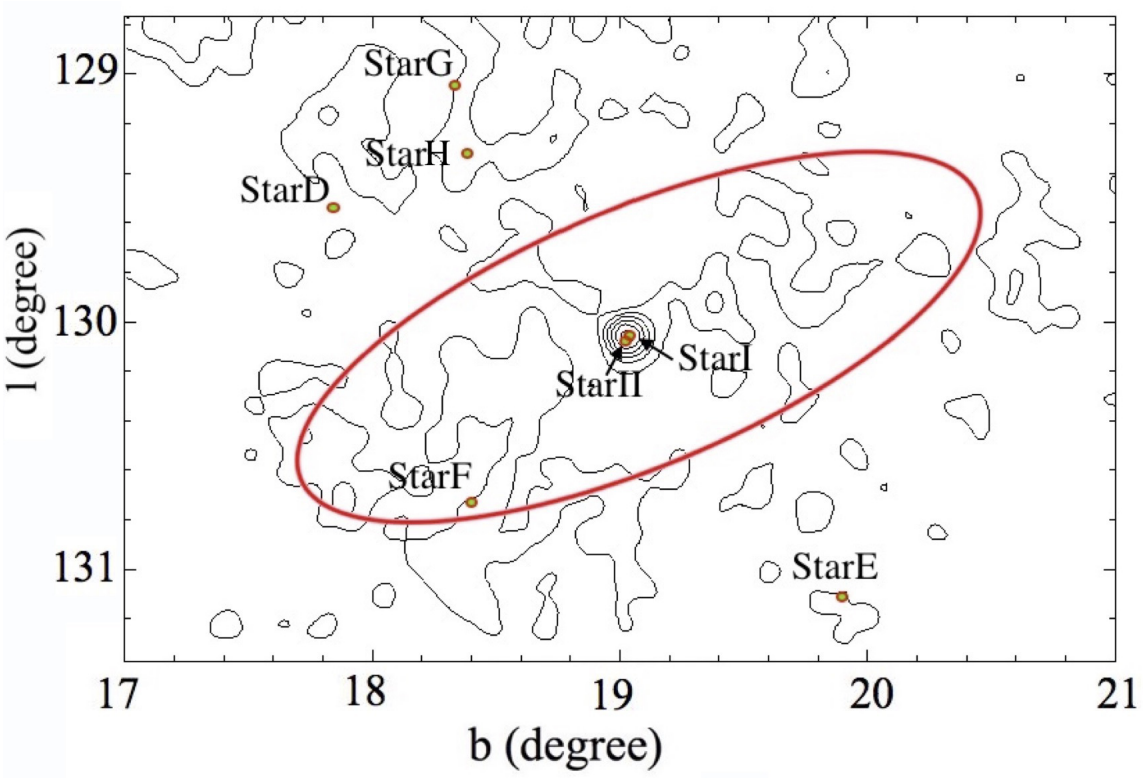

Figure 2.6: Position diagram of our Pal 1 members and candidates relative to the SDSS stellar densities around Pal 1. The red outline shows the position of the tails from Niederste-Ostholt et al. (2010). Our stars do not lie in those tails, except Star F.

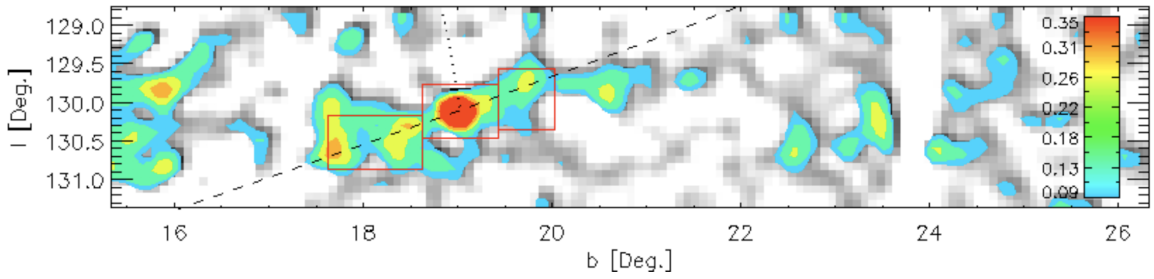

Figure 2.7: Pixel density plot of Pal 1 cluster using the SDSS stellar densities centered on Pal 1 with high spatial resolution of 123×27 pixels. Note that coloured contours indicate 1.5, 2, 3, 4 and 5 σ levels above the mean and the colour scale within the contours shows the pixel density in each region. This plot is from Niederste-Ostholt et al. (2010).

2.7.1 Tidal Tails of Pal 1

The position of the Pal 1 candidates with respect to the tidal tails mapped out by Niederste-Ostholt et al. (2010) based on SDSS photometry are shown in Fig. 2.6 and Fig. 2.7 . Their contour map is constructed from a probability-weighted star count map of Pal 1 candidates from the CMD in the MSTO/MS region. The number of candidates per square arcmin can be determined as 0.856 at the centre of Pal 1 and 0.050 above the background region. The positions of Stars I, II, and D-H are shown relative to new isophotes determined by M. Irwin from the same SDSS data in Fig. 2.6. A difference in the adopted bin sizes and isophote levels can suppress the apparent tidal features. Only one of these candidates, Star F, is coincident with the tidal tail found by Niederste-Ostholt et al. (2010).

Given the distance to Pal 1 as 14.2 kpc from the Sun (Sarajedini et al. 2007), and the angular separations of each star from its core, then the minimum distances of each star from the core of Pal 1 range from 220.8 pc (Star F) and 236.9 pc (Star H), to 294.6 pc (Star G), 319.8 pc (Star D), and 326.7 pc (Star E). For these stars to have reached these distances over the lifetime of this cluster (< 6 Gyr) would have required ejection velocities ≤ 1 kms^{-1}. These velocities are not particularly large, therefore it is possible that if stars escape from Pal 1 then they could be lurking at these angular separations.

2.7.2 Membership Probability Analysis

We examined the Besançon model (Robin et al. 2003) of the stellar populations in the Galaxy to evaluate membership probability of the new Pal 1 candidates. The number of stars in the smooth Galactic halo in the direction of Pal 1 are estimated based on similar limits in magnitude, colour, radial velocity, and metallicity (Fig. 2.8). To extract this simulated dataset, we run the model with the following selection criteria:

- an H-band range of 7 to 13.8, comparable to the APOGEE target list.
- a distance interval from 0 to 50 kpc, to include most of both foreground and background stars.
- a 7 sq. deg. field of view, centred on Pal 1 to match the SDSS field.
- The APOGEE database flags all non-giant stars as dwarfs. To directly compare the Besançon results with APOGEE, MS, WDs and T Tauri stars were removed

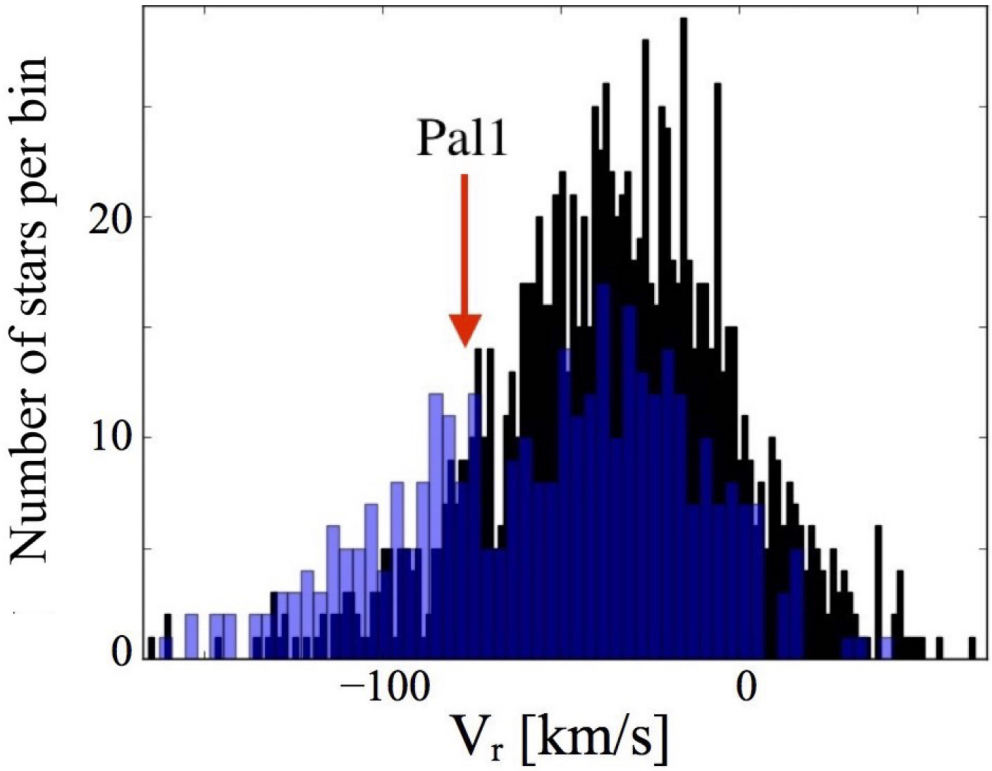

Figure 2.8: Histogram of the heliocentric radial velocities of APOGEE data (blue bars) and as determined from the Besançon model (Robin et al. 2003) in the direction of Pal 1 (black bars, renormalized). This suggests that our candidate Pal 1 objects could be consistent with sampling of the smooth Galactic halo distribution.

from our Besançon model and only giant stars were taken into account.

These selection criteria result in 1124 total stars in the Besançon model. 129 (12%) stars have radial velocities (-75 ± 15 kms^{-1}) and metallicities ([Fe/H] $= -0.6 \pm 0.4$) similar to our parameters for the APOGEE search in the Pal 1 field. These should be treated as field contaminants from the smooth halo distribution. In comparison, the SDSS/APOGEE Pal 1 field contains 377 giants, of which 33 (9%) have radial velocities and metallicities similar to Pal 1. Therefore, the Besançon model predicts a larger fraction of field contaminants (12%) than observed in the APOGEE Pal 1 field (9%). This strongly implies that the APOGEE field is representative of the smooth halo, with no evidence for additional stars due to the Pal 1 globular cluster.

It should be noted that APOGEE's Pal 1 field is subject to observational placements, particularly in the fibre limitations. These include (1) crowding in the centre of Pal 1 where the bonafide members are located, (2) that not all red giants can be observed simultaneously, and (3) that only 30% of the total number of good targets were observed.

A Monte Carlo approach was also used to randomly examine the potential for extracting Pal 1 members from APOGEE Pal 1 field. This was done by selecting 30% of stars from Besançon model to account for the APOGEE selections. For each sampling run, the fraction of field stars with our search criteria for Pal 1 radial velocities and metallicities (-75 ± 15 kms^{-1} and [Fe/H] $= -0.6 \pm 0.4$ dex, respectively) was calculated. 10000 runs were performed and the histogram of the distribution of corrected field contaminants is shown in Fig. 2.9. This histogram shows a well defined Gaussian distribution with a mean fraction of Pal 1 contaminants of 0.12 ± 0.02.

Considering that number of stars in the RV and [Fe/H] search criteria in the APOGEE Pal 1 field yielded 33 out of 377 stars (or 9%), we find that this is consistent with the predicted estimate from our Monte Carlo sampling of the Besançon smooth halo.

2.7.3 Binarity

The velocity variation of the candidates are examined to find any evidence for a binarity, which could affect the stellar parameters analysis. The radial velocity variations for the two Pal 1 members and for all of our candidate stars are shown in Fig. 2.10. Note that the y-axis represent the RV scatter of the candidates and is the standard

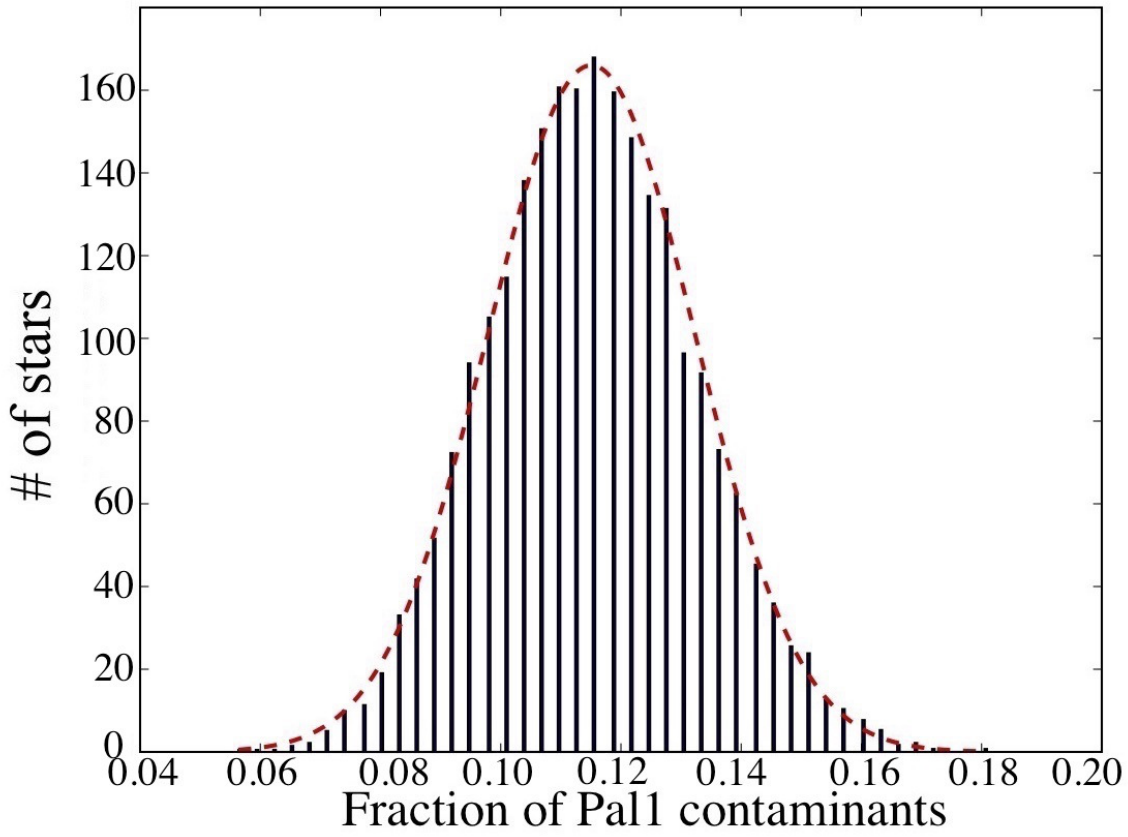

Figure 2.9: The histogram of the Gaussian distribution of Pal 1 field contamination after 10000 runs in the Monte Carlo simulation. This plot suggests that $\sim$ 12 % of stars in Pal 1 field have radial velocities and metallicities comparable to our search criteria around the Pal 1 core.

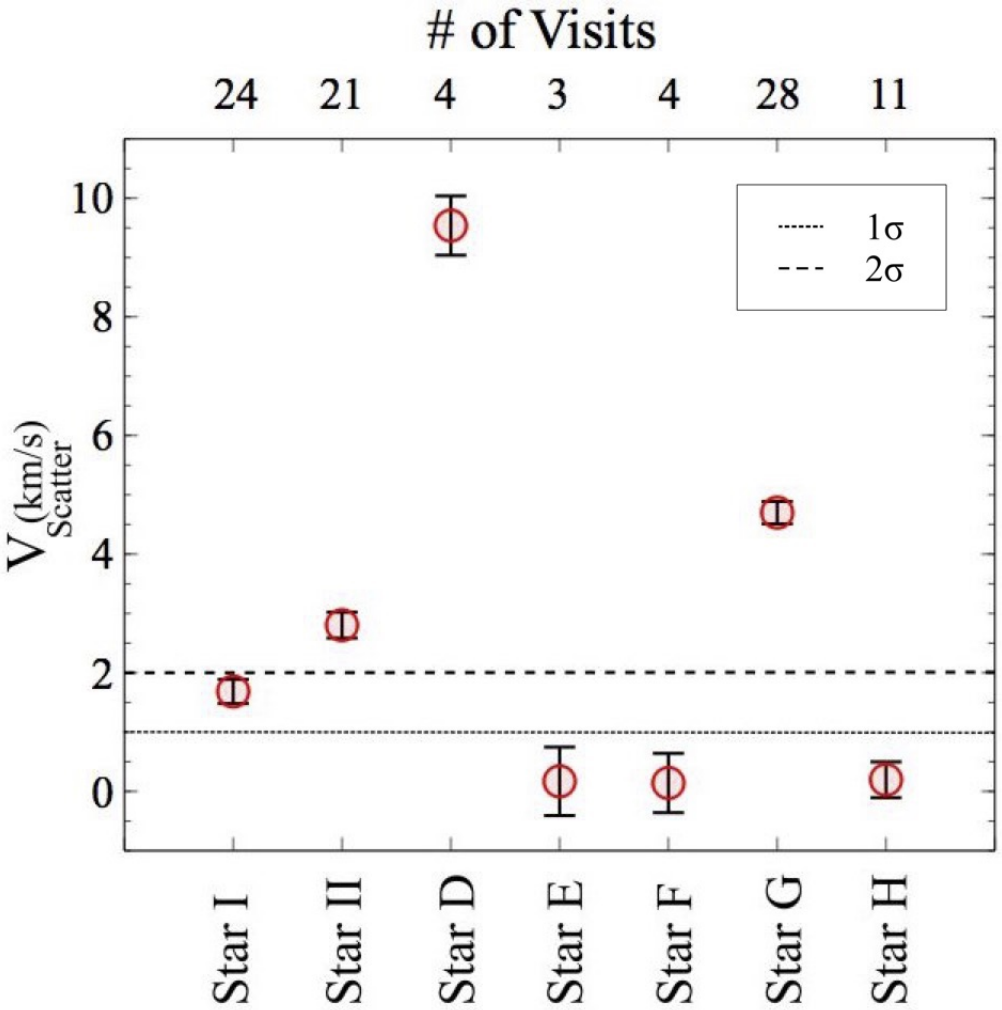

Figure 2.10: Velocity variation of the Pal 1 members and candidates, with respect to number of visits for each star. When the scatter is ≥ 1 kms^{-1} (dotted line), there is a high probability of a binary system. Error bars are $1/\sqrt{\#\ of\ visits}$.

deviation of all visits for each target. Nidever et al. (2015) has analysed a Plate-to-Plate RV variation analysis for the APOGEE stars and found that the RVs in the APOGEE database are very stable as the rms scatter is $\sigma = 0.044$ kms^{-1}. They suggest that stars with RV scatter of greater than 1 kms^{-1} have uncertainty much larger than the typical uncertainties and are possibly in a binary system.

Only Stars D and G show a scatter in their radial velocities well above the 2σ limit suggested by Nidever et al. (2015) for detecting binary systems. However, the RV scatter of Star II suggests that it too may be in a binary system. If so, the binary nature of this star does not seem to have affected either its optical analysis, nor our analysis of the corrected IR spectra, since the stellar parameters and chemical abundance ratios are in good agreement with other stars in Pal 1. It should be noted that the binarity of Star D, E, F and H cannot be conclusively established as the sample sizes of these stars are small.

2.7.4 DR13

In the SDSS DR13 release, an attempt to unweight spectra with the persistence problem was established to improve the combined spectral analyses (Albareti et al. 2016). When we examine the DR13 database, two more objects could be added to our analysis; however, the results for Stars I and II are still significantly different from the optical results (see Table 2.4). We did not pursue the DR13 data release further. The persistence problem is indeed well named.

2.8 Summary

Two members of the unusual star cluster Pal 1 have been observed in the APOGEE survey. Examination of their ASPCAP database results are in very poor agreement with previously determined optical analyses. We trace this problem to the known persistence problem that affects up to 30% of the spectra in the APOGEE database. By removing those spectra with persistence (and other reduction problems), we have re-analysed the cleaned spectra. Our new analyses for the APOGEE spectra of Stars I and II are in excellent agreement with the optical analysis by Sakari et al. (2011). One star, Star F, may be a member of Pal 1, based on its heliocentric radial velocity, metallicity, chemical abundances, and location in the tidal tails. However, the temperature of this star is highly uncertain, and it may be (or be contaminated by) an AGB star. All other candidate members found in the APOGEE DR12 database

appear to be part of the smooth Galactic background.

Chapter 3

Observation and Spectroscopy of Candidate Extremely Metal-Poor Stars from the Pristine Survey

This work was carried out as part of an independent studies course supervised by Dr. Patrick Côté at the NRC Herzberg Astronomy and Astrophysics. I led the observations, the data extraction and correction, data analysis, data interpretations, and I made all plots, figures and tables.

3.1 Introduction

Extremely metal-poor (EMP) stars with metallicities [Fe/H] < -3.0 are rare but important observing targets. We believe that after the Big Bang, the early universe was made of the three lightest elements, Hydrogen, Helium and Lithium. The condensation of the primordial gases formed EMP stars. These EMP stars did not have the chance of being metal-enriched by the heavy elements as most of the heavy elements are formed during the supernovae explosions or thermo-nuclear reactions inside of stars. The EMP stars have a relatively long lifetime of at least 12.5 Gyr (Pallottini et al. 2014). Therefore, low-mass EMP stars ($<1M_{\odot}$) are still observable as their lifetime is longer than the current age of the universe, in contrast, the massive stars had the chance of being evolved into their next stellar phase and have become neutron stars, black holes or white dwarfs (Caffau et al. 2017).

Observation and examination of the EMP stars can help us understand the early formation of our Milky Way galaxy and its early pristine stars. Spectroscopy of the EMP stars is challenging as their number of detectable absorption lines is significantly lower than in other stars. In fact, a low-resolution spectrum of an EMP star often

has only one prominent absorption line: Ca II K absorption line (Caffau et al. 2014). Therefore, observation of stars with a narrow band filter centred on the Ca II H and K lines is a well-known method for detection of the EMP stars (Twarog et al. 2007; Anthony-Twarog & Twarog 1998; Twarog & Anthony-Twarog 1995).

The Pristine survey is a narrow-band photometric survey that is centred on Ca II H and K lines and is being undertaken in the northern hemisphere (Starkenburg et al. 2017). This survey uses MegaCam on the Canada-France-Hawaii Telescope (CFHT) for detection of the EMP stars in the Galaxys halo. It is the goal of the Pristine survey to detect the metal-poor stars in the halo and map the metal-poor structure of the Galactic halo. Currently, among candidates in the initial list of the Pristine survey, 24% of them are believed to be EMP with [Fe/H] $\leq$ -3 (i.e. based on both g-i and g-r colours, Starkenburg et al. 2017). The DAO-Pristine project's goal is observing candidate EMP stars (with 14.0 <V< 15.2) in the Pristine survey to narrow down the initial list of the candidates. This can be done by detecting the strong Ca II triplet (CaT) absorption lines of the candidates from the Pristine Survey.

3.2 Observed Targets

For this project, we used the 1.8m Plaskett telescope at the Dominion Astrophysical Observatory (DAO) with the following setup to collect spectra centred on the CaT absorption lines:

- SITe-2 CCD detector (#pixels: 1752×532)
- Cassegrain Spectrograph (2161R with 600 g/mm grating and 30 Å/mm dispersion)
- Wavelength coverage of 8156 Å- 8899 Å (to cover the CaT lines)

During our 25 nights at the DAO, 52 targets were observed (note that there were over 200 targets in the initial list but 52 targets were observed due to the limited observing conditions and observation time). These targets include Arcturus, three standard Pristine stars that were previously observed with ESPaDOnS[1] instrument and 48 new targets (see Table 3.1 and 3.2).

[1]ESPaDOnS is a high-resolution echelle spectrograph with resolving power of over 68000, which makes it an ideal tool for precise observation of faint objects.

Table 3.1: Coordinates and metallicities of Arcturus and standard Pristine stars (from ESPaDOnS survey).

Name	RA (deg)	Dec (deg)	[Fe/H] $(1/cm^2)^a$
Arcturus	213.917	19.182	-0.5
pr.255.555+10.861 (PP4)	255.555	10.861	-2.6
pr.198.548+11.412 (P27)	198.548	11.412	-3.3
pr.237.834+10.590 (PP6)	237.834	10.590	-2.0

[a] Recall that [Fe/H]= log n(Fe/H)$_*$ - log n(Fe/H)$_\odot$

Table 3.2: Coordinates and metallicity of new observed Pristine candidates. Note that the listed metallicities are from Pristine survey and is determined from (g-i) and (g-r) colour indices.

Name	RA (deg)	Dec (deg)	$[Fe/H]_{gi}$ $(1/cm^2)$	$[Fe/H]_{gr}$ $(1/cm^2)$
pr.138.594+15.366	138.594	+15.366	-2.1	-2.2
pr.180.474+11.070	180.474	+11.070	-2.6	-2.7
pr.180.947+16.381	180.947	+16.381	-2.8	-2.5
pr.228.656+09.091	228.656	+09.091	-3.0	-3.0
pr.244.487+16.893	244.487	+16.893	-3.1	-3.0
pr.187.859+03.622	187.859	+03.622	-3.1	-3.2
pr.180.792+03.622	180.792	+03.408	-3.1	-3.7
pr.224.593+11.471	224.593	+11.471	-3.3	-3.1
pr.187.978+08.729	187.978	+08.729	-3.3	-3.7
pr.246.514+05.983	246.514	+05.983	-3.6	-3.8
pr.131.513+15.443	131.513	+15.443	-3.6	-3.6
pr.190.647+08.411	190.647	+08.411	-3.8	-3.6
pr.202.344+13.229	202.344	+13.229	-3.8	-3.6
pr.181.634+11.994	181.634	+11.994	-3.1	-3.0
pr.183.616+0.857	183.616	+0.857	-2.6	-2.7
pr.208.080+04.427	208.080	+04.427	-3.7	-3.6
pr.210.456+14.636	210.456	+14.636	-2.6	-2.6
pr.217.386+15.165	217.386	+15.165	-2.9	-2.9
pr.237.357+12.997	237.357	+12.997	-2.6	-2.6
pr.255.804+10.844	255.804	+10.844	-2.9	-2.9

pr210.863+08.180	210.863	+8.180	-2.7	-2.7
pr204.901+10.551	204.901	+10.551	-3.2	-3.0
pr214.556+07.467	214.556	+7.467	-2.6	-2.8
pr216.124+10.214	216.124	+10.213	-2.5	-2.4
pr225.399+02.833	225.399	+2.833	-2.7	-2.7
pr233.514+01.410	233.514	+1.410	-2.7	-2.7
pr233.861+02.583	233.861	+2.583	-3.2	-3.1
pr234.385+02.970	234.385	+2.970	-3.2	-3.6
pr236.107+10.531	236.107	+10.531	-2.6	-2.4
pr236.311+02.445	236.311	+2.445	-2.7	-2.6
pr237.144+04.546	237.144	+4.546	-2.6	-2.6
pr237.972+04.258	237.972	+4.258	-3.6	-3.4
pr238.722+06.195	238.722	+6.194	-2.9	-2.8
pr241.790+14.092	241.790	+14.092	-2.8	-2.8
pr243.000+16.911	243.000	+16.911	-2.4	-2.4
pr243.440+05.264	243.440	+5.264	-2.5	-2.4
pr244.614+16.918	244.614	+16.918	-2.5	-2.5
pr245.484+17.616	245.484	+17.616	-2.5	-2.5
pr246.558+09.695	246.558	+9.695	-2.9	-2.9
pr246.917+15.132	246.917	+15.132	-2.5	-2.5
pr247.001+16.065	247.001	+16.065	-2.5	-2.5
pr247.138+05.897	247.138	+5.896	-2.5	-2.6
pr247.199+16.223	247.199	+16.223	-2.7	-2.7
pr247.823+16.225	247.823	+16.225	-2.4	-2.6
pr247.930+17.660	247.930	+17.660	-2.7	-2.6
pr248.175+07.652	248.175	+7.652	-2.5	-2.4
pr252.375+17.521	252.375	+17.521	-2.5	-2.6
pr253.773+15.106	253.773	+15.106	-2.5	-2.6

For the new targets, spectra were collected using a fixed 60 minutes exposure time. Then the spectra are calibrated with the calibration frames (i.e. the bias and flat frames) by Dave Balam. Finally, the calibrated spectra are median-combined and normalized with respect to a high order Legendre polynomial. The normalized spectra of the targets are shown in Fig. 3.1-3.5.

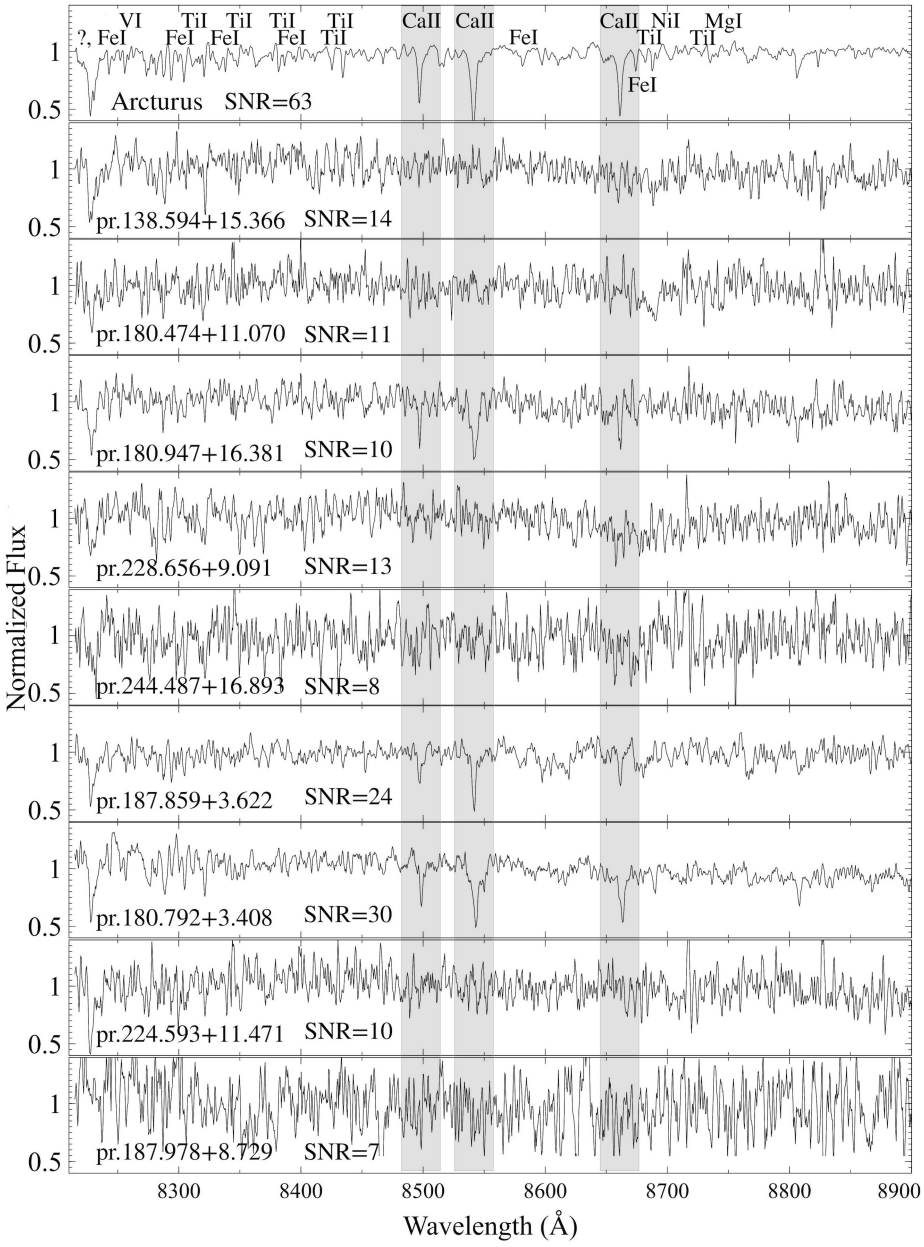

Figure 3.1: Spectra of the Pristine targets. The three Ca II absorption lines are shaded. Note that the standard Pristine stars have a star in top left of their panel. All the SNR values are per resolution element.

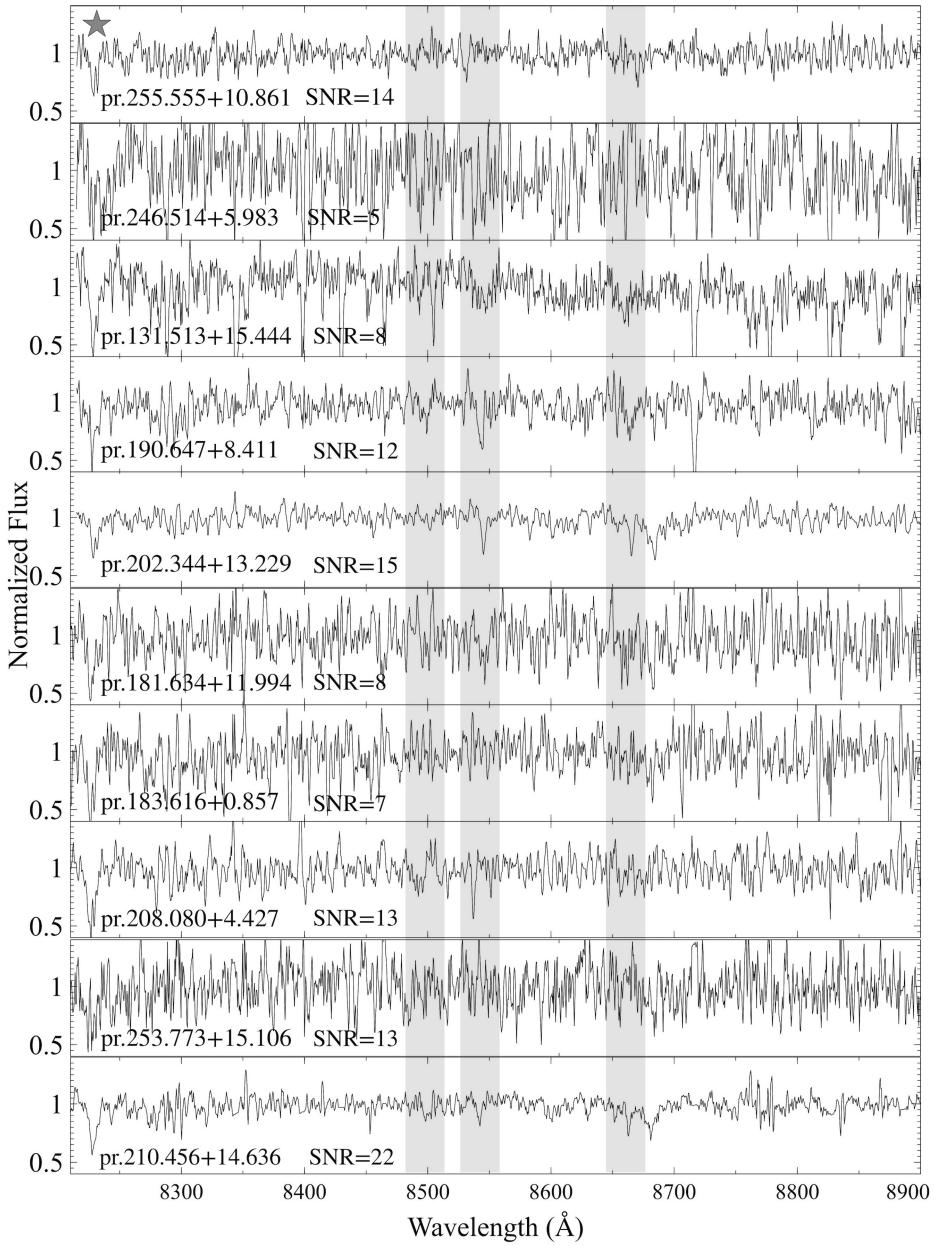

Figure 3.2: Spectra of the Pristine targets. The three Ca II absorption lines are shaded. Note that the standard Pristine stars have a star in top left of their panel. All the SNR values are per resolution element.

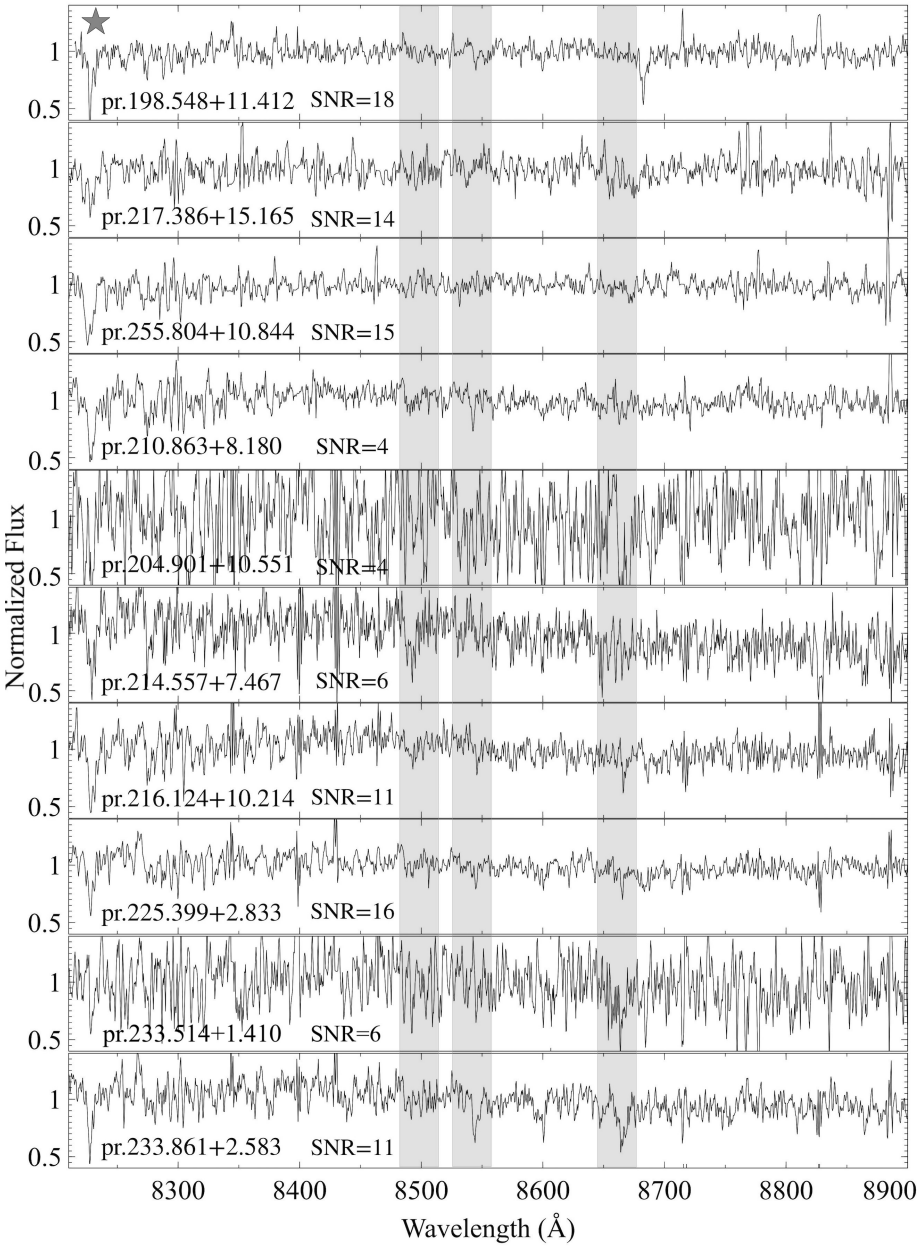

Figure 3.3: Spectra of the Pristine targets. The three Ca II absorption lines are shaded. Note that the standard Pristine stars have a star in the top left of their panel. All the SNR values are per resolution element.

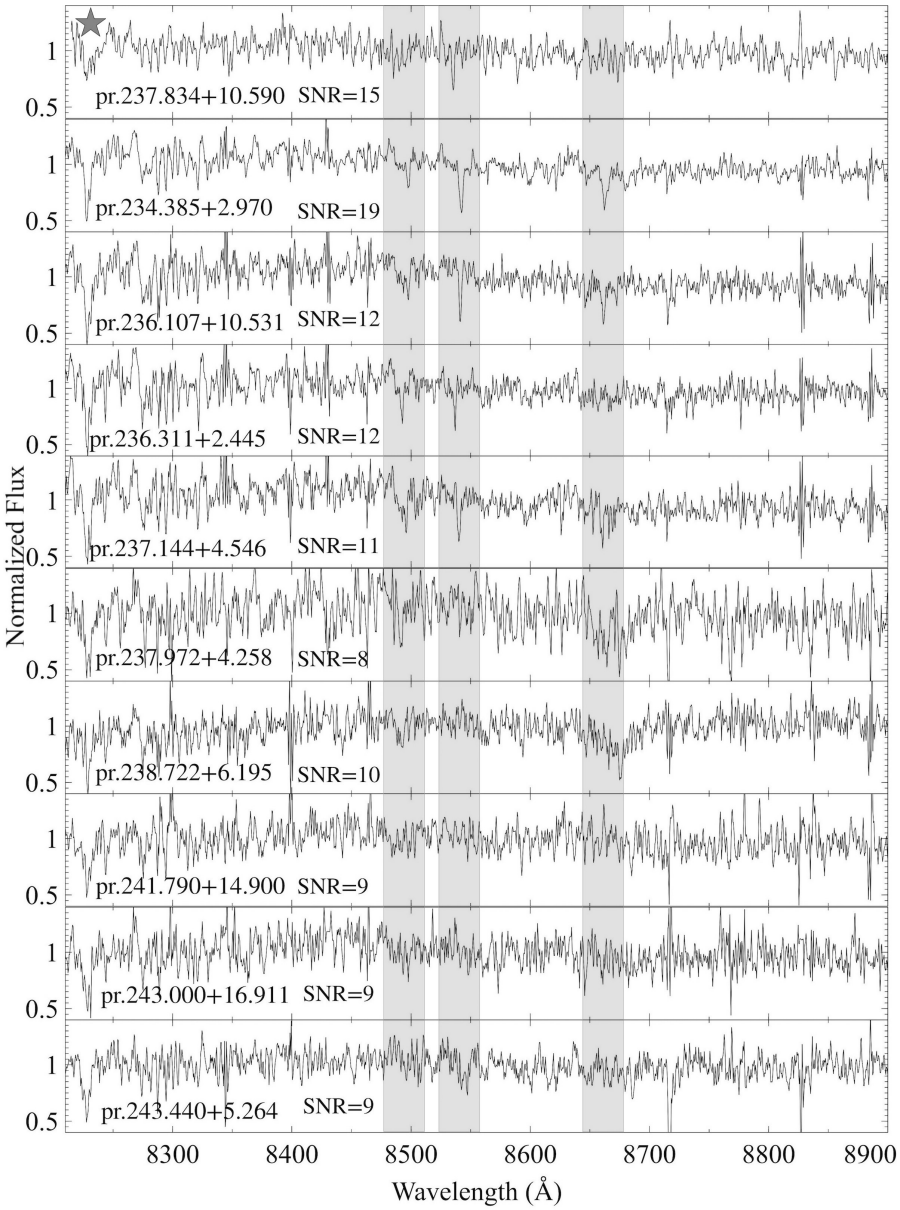

Figure 3.4: Spectra of the Pristine targets. The three Ca II absorption lines are shaded. Note that the standard Pristine stars have a star in the top left of their panel. All the SNR values are per resolution element.

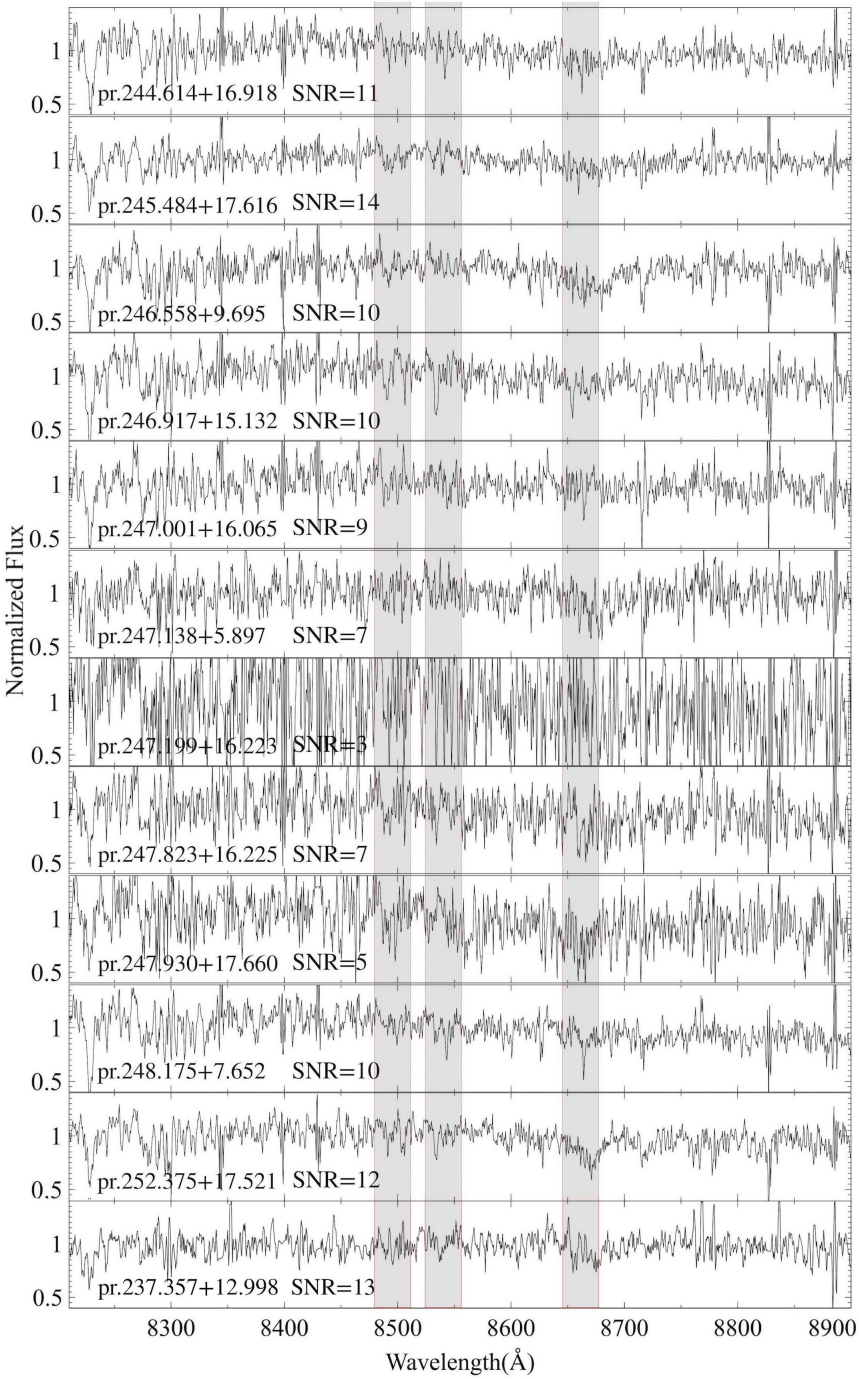

Figure 3.5: Spectra of the Pristine targets. The three Ca II absorption lines are shaded. Note that the standard Pristine stars have a star in top left of their panel. All the SNR values are per resolution element.

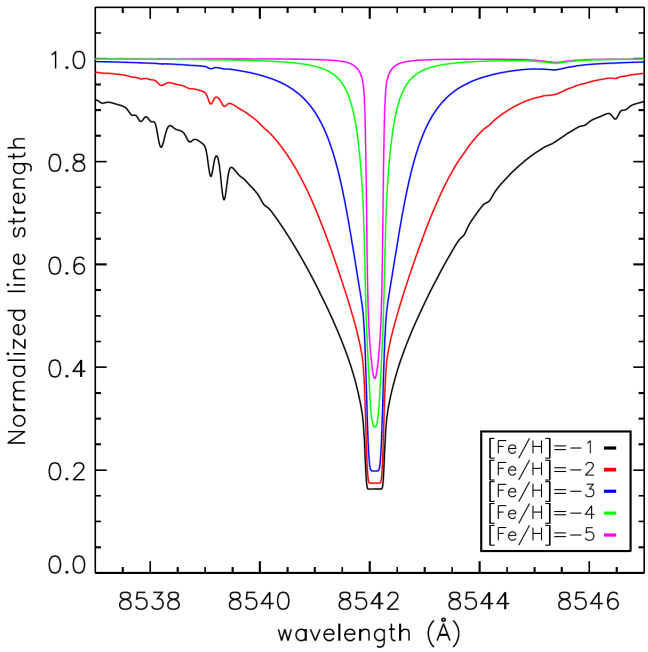

Figure 3.6: The change of the CaT line absorption line at 8542 Å with the metallicity of the star. Note that the Fe wings on the body of the CaT lines are one of the main causes of this correlation between the EQW of the CaT lines and the metallicity. This figure is from Starkenburg et al. (2010).

3.3 The Mysterious Case of Ca II Triplet lines

The exact correlation between the CaT absorption lines and metallicity of a star has always been a question as the only way to determine it is the empirical examinations of this correlation. Armandroff & Zinn (1988) introduced one of the first empirical correlations between CaT lines and metallicity of the galactic globular clusters by showing a correlation between the EQW of the CaT lines and the luminosity of stars along the RGB. Follow-up studies could generalize this correlation for the individual field stars as well as the globular clusters (Armandroff & Da Costa 1991). In particular, the CaT metallicity indicator is an efficient method for extremely metal-poor stars as the strong CaT lines are the only detectable lines in the spectra of EMP stars.

In the last few years, several studies have determined this correlation empirically for EMP stars with metallicity less than -2.5 dex. Most of the current CaT metallicity equations are determined for the globular clusters with a well defined horizontal branch (HB), but not all stellar populations have an observable HB, and the HB-

based correlations cannot be used for the field stars. In this work, our targets are individual field stars, which means the HB-based correlations cannot be used for them. Therefore, we used the results of Starkenburg et al. (2010) that has determined three CaT metallicity correlations as a function of (V-V_{HB}), M_I and M_V. The following equation from Starkenburg et al. (2010) is used in our analysis:

$$[Fe/H] = -2.9 + 0.187 \times M_v + 0.442 \times EW_{2+3} - 0.882 \times EW_{2+3}^{-1.5} + 0.0133 \times EW_{2+3} \times M_v \quad (3.1)$$

This equation requires the absolute magnitude of the target (M_v) and EQW_{2+3} of the two strong Ca II lines (8542Å and 8662Å). Note that the first Ca II line (8498Å) is not included in this equation as it is relatively weaker than the other two.

3.3.1 Results

The EW_{2+3} of CaT lines of all targets are measured using *IRAF* (see Table 3.3-3.5), and the absolute magnitudes of the targets are determined with the isochrone fitting method. For the isochrone method, we used the Dartmouth Stellar Evolution Database (Dotter et al. 2008) to generate an isochrone with age of 12 Gyr and [Fe/H] of -2.5 dex. The photometric values of the targets are converted from SDSS ugriz system to Johnson VI (using transformation equations from Table 3 of Jordi et al. 2006) and overplotted on the isochrone. Two different possibilities are examined: a) all targets are giants b) all targets are dwarfs. For each case, the isochrone is vertically moved to determine two distance modulus for each star (i.e. giant and dwarf distance modulus). Finally, by having the apparent magnitude of the stars and also the distance modulus of them, the absolute magnitude of each case is determined (see Fig. 3.7).

From the measured EQW and the calculated absolute magnitude values, metallicities of all targets are derived (Table 3.3-3.5) using equation 3.1.

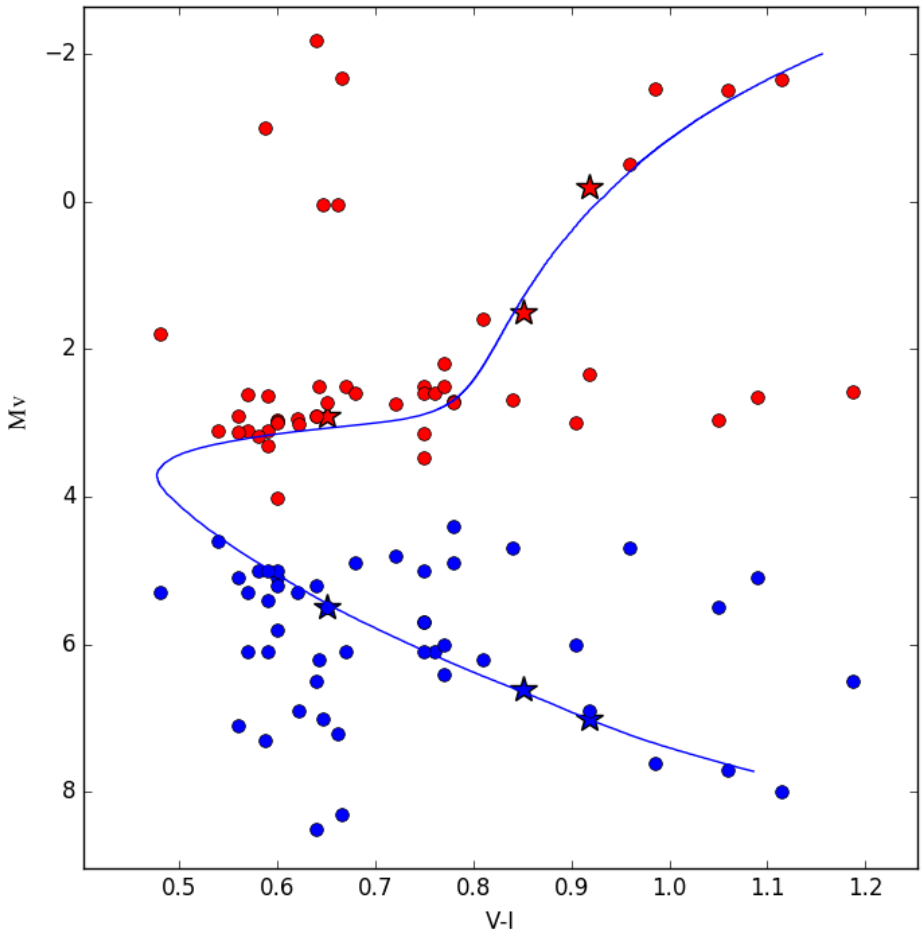

Figure 3.7: The absolute magnitudes of the target stars are determined for two assumptions of being giant (red) and dwarf (blue). The isochrone is for age of 12 Gyr and [Fe/H] $\sim$ -2.5 from the BaSTI isochrones (Pietrinferni et al. 2004). Note that the star symbols show the standard Pristine stars.

Table 3.3: CaT metallicity for Arcturus and the standard stars.

Name	V (mag)	I (mag)	Mv_{giant} (mag)	Mv_{dwarf} (mag)	EW_{2+3} (Å)	$[Fe/H]_{giant}$ ($1/cm^2$)	$[Fe/H]_{dwarf}$ ($1/cm^2$)	[Fe/H] ($1/cm^2$)	SNR
Arcturus	—	—	-0.04	—	5.1	-0.7	—	-0.5	63
pr.255.555+10.861 (PP4)	14.50	13.65	1.5	6.6	1.6	-2.3	-1.0	-2.6	14
pr.198.548+11.412 (P27)	14.30	13.65	2.9	5.5	0.8	-3.2	-2.7	-3.3	18
pr.237.834+10.590 (PP6)	14.40	13.48	-0.2	7.0	2.0	-2.3	-0.8	-2.0	15

Table 3.4: CaT metallicity for the new targets.

Name	V (mag)	I (mag)	Mv_{giant} (mag)	Mv_{dwarf} (mag)	EW_{2+3} (Å)	$[Fe/H]_{giant}$ ($1/cm^2$)	$[Fe/H]_{dwarf}$ ($1/cm^2$)	$[Fe/H]_{gi}$ ($1/cm^2$)	$[Fe/H]_{gr}$ ($1/cm^2$)	SNR
pr.138.594+15.366	14.07	13.48	3.1	6.1	1.0	< -2.0	<-1.4	-2.1	-2.2	14
pr.180.474+11.070	14.55	13.98	3.1	6.1	0.7	< -1.9	<-1.5	-2.6	-2.7	11
pr.180.947+16.381	15.01	14.20	1.6	6.2	3.3	<-0.6	<0.6	-2.8	-2.5	10
pr.228.656+09.091[b]	14.80	14.24	2.9	7.1	—	—	—	-3.0	-3.0	13
pr.244.487+16.893[a]	14.35	13.68	2.5	6.1	1.0	<-2.8	<-2.1	-3.1	-3.0	8
pr.187.859+03.622	13.13	12.49	2.9	6.5	2.7	-1.3	-0.8	-3.1	-3.2	24
pr.180.792+03.622	13.18	12.12	-1.5	7.7	3.8	-1.5	0.7	-3.1	-3.7	30
pr.224.593+11.471[a]	14.27	13.79	1.8	5.3	1.3	<-2.5	<-1.6	-3.3	-3.1	10
pr.187.978+08.729	14.93	14.18	2.5	5.7	2.1	<-1.5	< -0.7	-3.3	-3.7	7
pr.246.514+05.983	14.47	13.51	-0.5	4.7	3.8	<-1.5	<0.3	-3.6	-3.8	5
pr.131.513+15.443[a]	14.41	13.64	2.2	6.4	0.7	<-3.7	<-2.9	-3.6	-3.6	8
pr.190.647+08.411	15.06	14.31	2.6	5.0	3.2	-1.6	-0.8	-3.8	-3.6	12
pr.202.344+13.229	14.24	13.48	2.6	6.1	2.3	-1.4	-0.7	-3.8	-3.6	15
pr.181.634+11.994	15.01	14.41	4.0	5.1	3.3	<-0.7	<-1.1	-3.1	-3.0	8
pr.183.616+0.857	14.49	13.95	3.1	4.6	1.4	<-2.2	<-2.4	-2.6	-2.7	7
pr.208.080+04.427	14.54	13.79	3.5	6.1	2.0	<-1.6	<-1.6	-3.7	-3.6	13
pr253.773+15.106[b]	14.81	14.17	-2.2	8.5	—	—	—	-2.5	-2.6	7
pr.210.456+14.636	14.46	13.86	3.0	5.2	1.5	-2.1	-2.2	-2.6	-2.6	22
pr.217.386+15.165[a]	14.61	14.03	3.2	5.0	1.2	<-2.3	<-2.4	-2.9	-2.9	14
pr.255.804+10.844[b]	14.34	13.72	2.9	5.3	—	—	—	-2.9	-2.9	15
pr210.863+08.180	14.50	13.72	2.7	4.4	3.6	-0.8	-0.4	-2.7	-2.7	15
pr204.901+10.551	14.88	14.32	3.1	5.1	—	—	—	-3.2	-3.0	4
pr214.556+07.467	14.64	14.04	3.0	5.0	—	—	—	-2.6	-2.8	6
pr216.124+10.214	14.49	13.65	2.7	4.7	1.5	<-2.1	<-1.7	-2.5	-2.4	11
pr225.399+02.833[a]	14.54	13.82	2.7	4.8	1.2	<-2.5	<-2.1	-2.7	-2.7	16
pr233.514+01.410	14.38	13.60	2.7	4.9	—	—	—	-2.7	-2.7	6
pr233.861+02.583	14.65	13.97	2.6	4.9	4.2	-0.5	0.0	-3.2	-3.1	11
pr234.385+02.970	14.80	14.16	2.9	5.2	3.9	-0.6	0.0	-3.2	-3.6	19
pr236.107+10.531	14.54	13.45	2.6	5.1	2.1	-1.7	-1.2	-2.6	-2.4	12
pr236.311+02.445	14.85	13.80	3.0	5.5	2.1	<-1.6	<-1.1	-2.7	-2.6	12
pr237.144+04.546	14.89	14.14	3.1	5.7	2.3	<-1.5	<-0.9	-2.6	-2.6	11

[a] Candidate EMP stars from Pristine.

[b] The EQW measurement of CaT is not reliable as the lines are extremely weak.

Table 3.5: CaT metallicity for the new targets.

Name	V (mag)	I (mag)	Mv_{giant} (mag)	Mv_{dwarf} (mag)	EW_{2+3} (Å)	$[Fe/H]_{giant}$ ($1/cm^2$)	$[Fe/H]_{dwarf}$ ($1/cm^2$)	$[Fe/H]_{gi}$ ($1/cm^2$)	$[Fe/H]_{gr}$ ($1/cm^2$)	SNR
pr237.972+04.258	14.65	14.00	2.7	5.5	2.4	<-1.5	<-0.9	-3.6	-3.4	8
pr238.722+06.195	14.76	14.19	2.6	5.3	1.4	<-2.3	<-1.7	-2.9	-2.8	10
pr241.790+14.092[a]	14.66	14.07	2.6	5.4	0.6	<-4.0	<-3.5	-2.8	-2.8	9
pr243.000+16.911	14.80	14.20	3.0	5.8	1.1	<-2.6	<-2.0	-2.3	-2.4	9
pr.237.357+12.997[a]	14.65	14.06	3.3	5.0	0.9	<-2.9	<-2.8	-2.6	-2.6	13
pr243.440+05.264	14.693	13.788	3.0	6.0	3.0	<-1.1	<-0.4	-2.5	-2.4	9
pr244.614+16.918	14.808	14.038	2.5	6.0	1.7	<-2.0	<-1.3	-2.5	-2.5	11
pr245.484+17.616[a]	14.797	14.155	2.5	6.2	1.0	<-2.8	<-2.1	-2.5	-2.5	14
pr246.558+09.695	15.015	14.393	3.0	6.9	1.2	<-2.4	<-1.6	-2.9	-2.9	10
pr246.917+15.132	14.766	13.578	2.6	6.5	2.8	<-1.3	<-0.4	-2.5	-2.5	10
pr247.001+16.065	14.789	13.871	2.3	6.9	2.4	<-1.6	<-0.6	-2.5	-2.5	9
pr247.138+05.897	14.837	14.190	0.0	7.0	1.9	<-2.4	<-0.9	-2.5	-2.6	7
pr247.199+16.223[a]	15.037	14.376	0.0	7.2	1.5	<-2.7	<-1.2	-2.7	-2.7	3
pr247.823+16.225	14.806	14.219	-1.0	7.3	3.0	<-2.0	<-0.1	-2.4	-2.6	7
pr247.930+17.660[a]	14.778	13.793	-1.5	7.6	1.5	<-3.0	<-1.1	-2.7	-2.6	5
pr248.175+07.652[a]	14.65	13.536	-1.7	8.0	2.1	<-2.6	<-0.6	-2.5	-2.4	10
pr252.375+17.521[a]	14.923	14.258	-1.7	8.3	2.0	<-2.7	<-0.6	-2.5	-2.6	12

[a] Candidate EMP stars from Pristine.

The estimated $[Fe/H]_{CaII}$ of the standard stars are in close agreement with the confirmed values. The residual plots of the estimated CaT-Fe of the new targets are shown in Fig. 3.8 and Fig. 3.9.

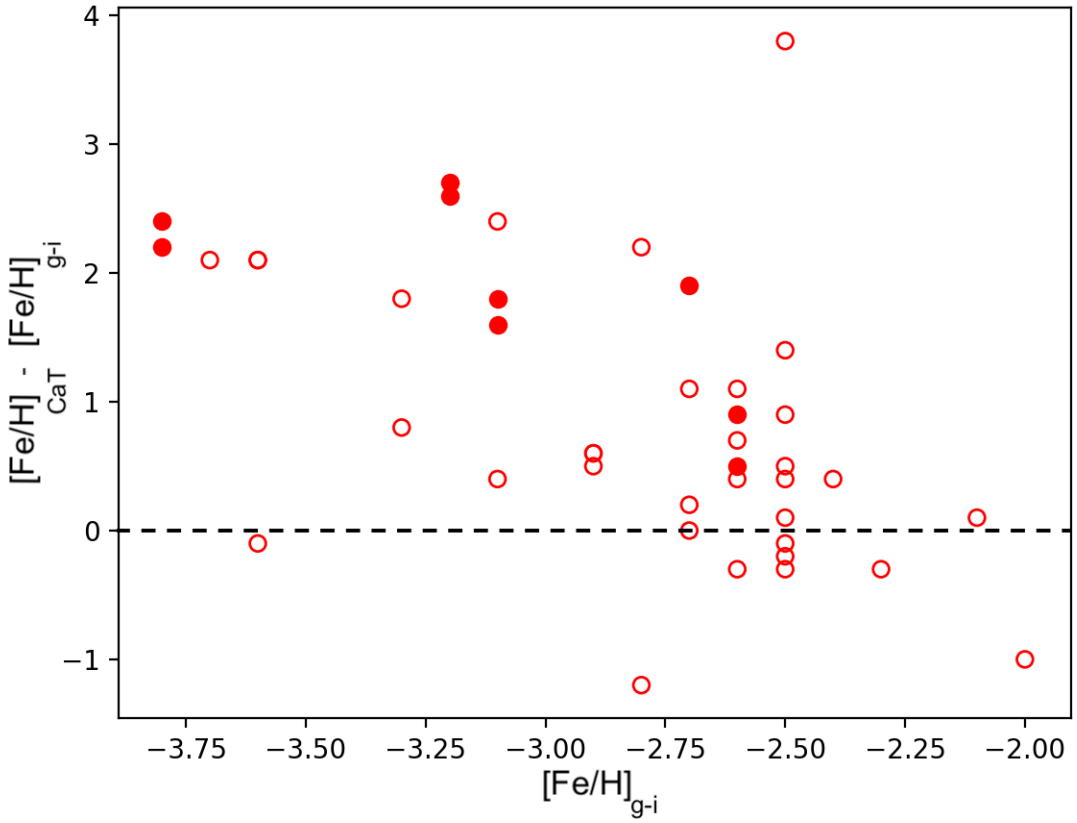

Figure 3.8: The residual plot of the estimated CaT-Fe assuming all our targets are giants. Note that the $[Fe/H]_{(g-i)}$ is from the Pristine database and is based on the g and i photometric colours. The open circles show upper-limit estimates.

3.3.2 Errors

According to Youakim et al. (2017), the Pristine estimates for hot stars (i.e. g-i<0.5 which corresponds to Teff<6000 K) are highly uncertain (see Fig. 3.9). Small errors in the photometric data (g, i, and Ca HK) for hotter stars will have larger uncertainties on the Pristine metallicity estimates. Possible sources of error in $[Fe/H]_{CaII}$ are as following:

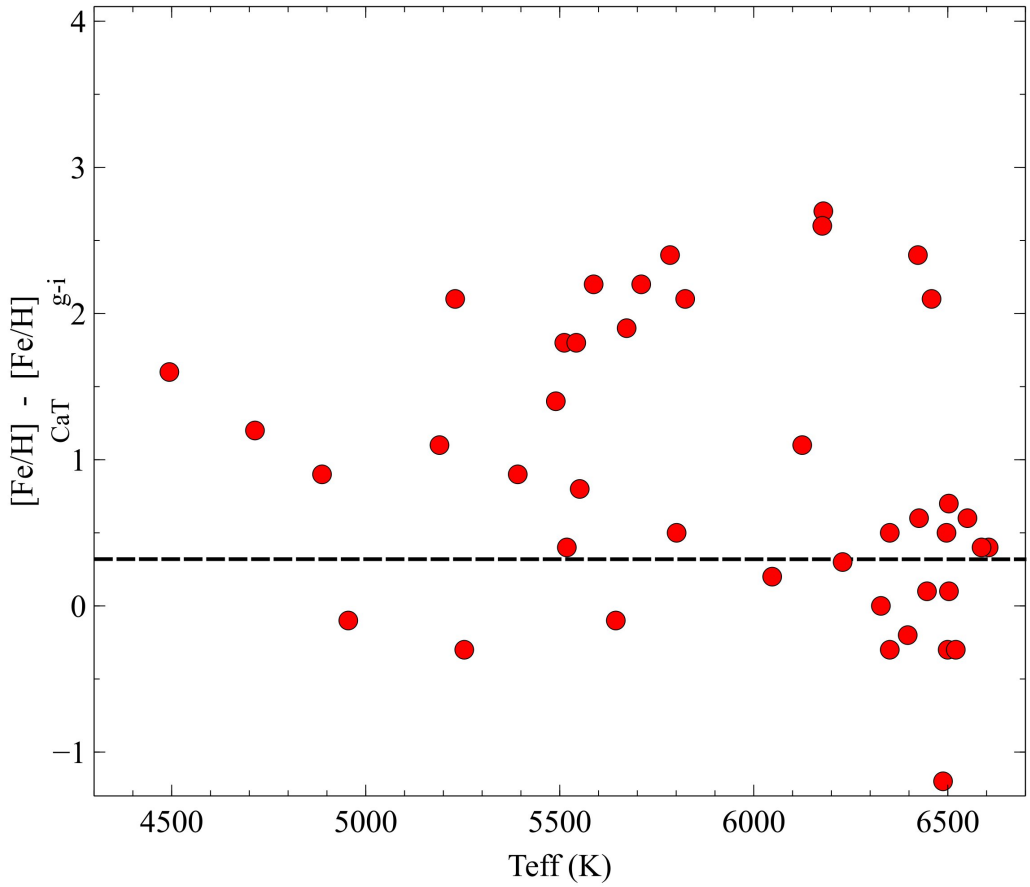

Figure 3.9: The residual plot of the estimated CaT-Fe with respect to temperature of the targets. The Pristine estimates for hot stars (i.e. g-i<0.5 which corresponds to Teff<6000 K) are highly uncertain (Youakim et al. 2017). Note that the $[Fe/H]_{(g-i)}$ is from the Pristine database and is based on the g and i photometric colours.

- M_v: The CaT-Fe calibration equation is optimized for -3<M_v <0.8 (Starkenburg et al. 2010). However the range of the absolute magnitudes of our targets is from -2.2<M_v <4.0, which means M_v of some of our stars is not within the calibration range.

- EW_{2+3}: The CaT metallicity indicator is very sensitive to the equivalent width of the Ca II lines (i.e. EW_{2+3}). Based on the previous studies (i.e. Carrera et al. 2013 and Starkenburg et al. 2010), the expected EW_{2+3} of Pristine stars is usually less than 2Å for [Fe/H]<-3. In spectra with weak CaT lines, noise on the continuum could be larger than the CaT absorption lines. Therefore the measured EQW of EMP stars can be significantly affected by the noise.

3.4 Observations Efficiency

In all four observing runs of the project, we had 25 observing nights (25 nights $\times$ 5 hours/night = 125 hours; see Fig. 3.10). However, only 14 nights were clear/partially-clear for our observations ($\sim$ 50 hours of observations in total).

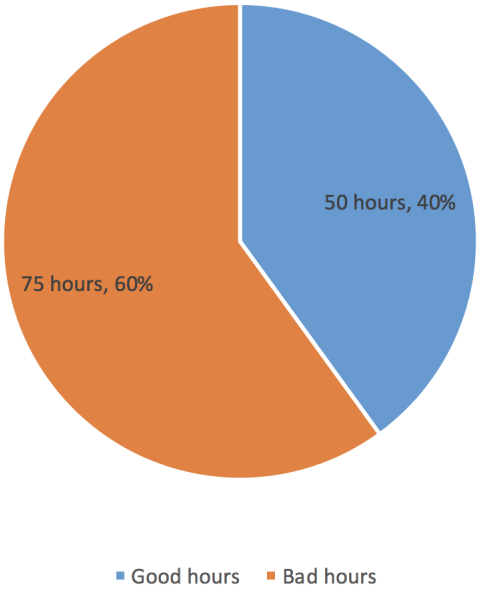

Figure 3.10: The unstable weather affected our observations critically. However, we managed to observe targets for about 50 hours. Note that the "Bad Hours" label in the chart refers to the cloudy and windy forecast that canceled our observations.

3.4.1 Candidate Pristine stars detection efficiency

The SNR of the observed candidate Pristine stars is shown in Table 3.3-3.5. For most of the cases, SNR is lower than the expected SNR of 30. The main reason for this issue is the cloudy weather of Victoria and our long exposure times (i.e. it was improbable to have a clear night for the full required one-hour exposure time of each target).

As it is shown in the Table 3.3-3.5, only one of the spectra's SNR is same as the expected value, and the other ones are in the range of 3<SNR<30. A histogram of SNRs of our targets is shown in Fig. 3.11. Note that strong CaT lines can be distinguished in all spectra with SNR>10, but accurate measurement of EQW of weak CaT lines requires higher SNR for most of the targets.

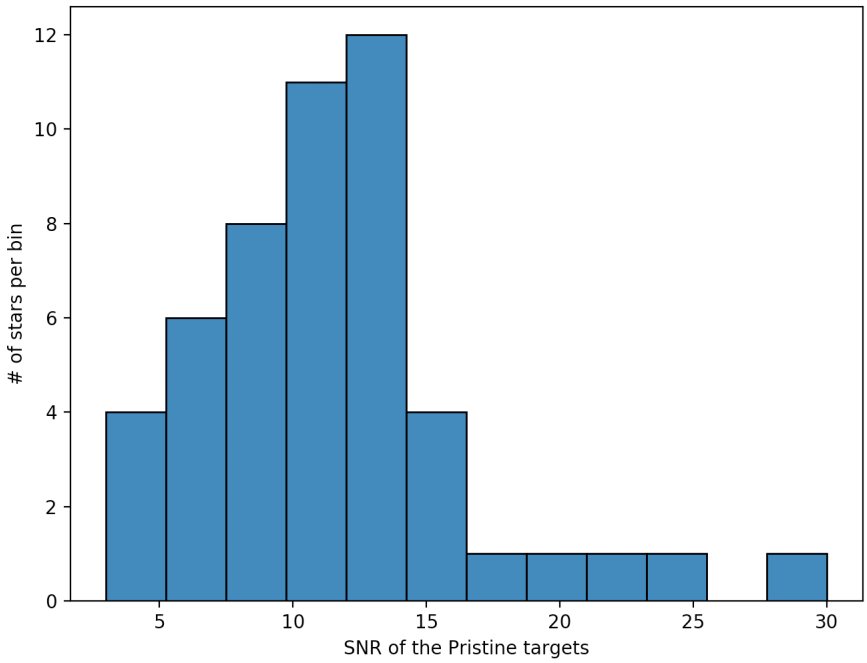

Figure 3.11: Distribution of SNR of the new Pristine targets.

Table 3.6: Possible candidate EMP stars

Name	Mv_{giant} (mag)	Mv_{dwarf} (mag)	EW_{2+3} (Å)	$[Fe/H]_{giant}$ ($1/cm^2$)	$[Fe/H]_{dwarf}$ ($1/cm^2$)	$[Fe/H]_{gi}$ ($1/cm^2$)	$[Fe/H]_{gr}$ ($1/cm^2$)	SNR
pr.244.487+16.893	2.5	6.1	1.0	<-2.8	<-2.1	-3.1	-3.0	8
pr.224.593+11.471	1.8	5.3	1.3	<-2.5	<-1.6	-3.3	-3.1	10
pr.131.513+15.443	2.2	6.4	0.7	<-3.7	<-2.9	-3.6	-3.60	8
pr.217.386+15.165	3.2	5.0	1.2	<-2.3	<-2.4	-2.9	-2.9	14
pr225.399+02.833	2.7	4.8	1.2	<-2.5	<-2.1	-2.7	-2.7	16
pr241.790+14.092	2.6	5.4	0.6	<-4.0	<-3.5	-2.8	-2.8	9
pr.237.357+12.997	3.3	5.0	0.9	<-2.9	<-2.8	-2.6	-2.6	13
pr245.484+17.616	2.5	6.2	1.0	<-2.8	<-2.1	-2.5	-2.5	14
pr247.199+16.223	0.0	7.2	1.5	<-2.7	<-1.2	-2.7	-2.7	3
pr247.930+17.660	-1.5	7.6	1.5	<-3.0	<-1.1	-2.7	-2.6	5
pr248.175+07.652	-1.7	8.0	2.1	<-2.6	<-0.6	-2.5	-2.4	10
pr252.375+17.521	-1.7	8.3	2.0	<-2.7	<-0.6	-2.5	-2.6	12

By the end of the four observing runs in the DAO-Pristine project, 12 targets are highlighted as possible EMP stars (Table 3.6). It should be noted that these stars will be followed up with other 4-8m facilities in the future.

There are two challenges based on the current configuration of the DAO-Pristine project that we need to examine in the future studies to improve the results:

1. Can we distinguish the foreground or background contaminants and not metal-poor stars from the possible EMP candidates?

   The CaT-Fe values are determined for two different cases: a) assuming all observed target are giants, b) assuming all observed targets are dwarfs. In general, for the cases that the absolute magnitude for the background or foreground stars (i.e. dwarfs) are significantly larger than 0.8 mag (i.e. the upper limit of the CaT-Fe calibration equation), the CaT-Fe will be unrealistically large. In all of the currently observed targets the Mv_{dwarf} is larger than Mv_{giant} but difference is not large enough to eliminate the possibility of being a dwarf. In future, we might be able to distinguish the foreground or background stars based on their absolute magnitude.

2. Could we confirm any EMP Pristine candidate? If yes or no, how much we trust our CaT-Fe results?

   By the end of the fourth run, we highlighted 12 candidate EMP stars (see Table 3.6). However, the SNR values of most of the targets are less than the expected value of 30. The current configuration for the Plaskett telescope can eliminate stars with strong Ca II lines, but most of the EQW estimates and the CaT-Fe values would be upper-limit (as the accurate measurement of EQWs requires higher SNR). Follow-up observations will be needed for more accurate and precise examination of the 12 candidate EMP stars.

3.5 Summary

Over 50 EMP candidates from the Pristine survey were observed at the DAO using the low spectral resolution spectrograph to detect the Ca II triplet (CaT) absorption lines. In the analysis of the spectra, two assumptions for the surface gravity are made (i.e.

giant and dwarf). Using isochrones from the Dartmouth Stellar Evolution Database (Dotter et al. 2008), the M_v of the targets were determined. Using measurements of the EQW of the CaT lines and the M_v determinations, the metallicity of the stars were estimated using the CaT-Fe equation from Starkenburg et al. (2010). Metallicities were also determined for standard stars to confirm this methodology. We have found 12 stars with weak Ca II triplet absorption lines. Their coordinates were sent to the Pristine team for follow-up observations at the Isaac Newton Telescope (INT, La Palma, Spain).

Chapter 4

Three-fold Analysis of Applications of Data Mining and Machine Learning in Astronomy

4.1 Introduction

In the past few years, astrophysics among many other fields has experienced a flood of observational data. It is believed that within the next few decades, the enormous amount of observed data will need several years of analysis if we do not change our traditional computation methods. New computational methods such as artificial intelligence (AI) and machine learning (ML) are among the best candidates for data mining and study of the new generation of data in the future. These new techniques combined with modern hardware and increased computing power will allow faster and more efficient examination of data. In other words, data mining and ML techniques can be used to find meaningful information (such as physical properties of the observed objects) from raw data (i.e. stellar spectra and supernovae light curves).

During my master's studies, I have contributed to three ML-related projects that are explained in the next sections. Supervised and unsupervised machine learning are the main components of ML methods. In supervised ML techniques, input variable(s) and output variable(s) are for training and the ML algorithm can be used to learn the mapping function from the input variable(s) to the output variable(s). In contrast, unsupervised ML is when the user use only the input variable(s), for understanding the relation between the points in the database. My projects included both supervised and unsupervised ML techniques.

4.2 Contributions to StarNet

In this project, the machine learning techniques have been applied to the SDSS-III Apache Point Observatory Galactic Evolution Experiment (APOGEE) survey (see Chapter 2 for more details about the APOGEE database). This database is an excellent testbed for different machine learning techniques as data are provided in a uniform and homogenous manner. The spectra of more than 100000 stars are provided in this database with multiple spectra for each target (to reach the minimum of SNR=100 in the co-added spectra of the targets). The APOGEE database examined these spectra through the APOGEE Stellar Parameters and Chemical Abundances Pipeline (ASPCAP), which is a data reduction pipeline tool. This technique's core is based on the nonlinear least squares fitting routine (FERRE, Pérez et al. 2016) of data that compares the raw spectra to the synthetic stellar model atmospheres. The ASPCAP's output results are the stellar parameters, including the effective temperature, gravity, metallicity and fifteen different elemental abundances (C, N, O, Na, Mg, Al, Si, S, K, Ca, Ti, V, Mn, Fe and Ni). We designed and implemented the StarNet supervised neural network to take the APOGEE's synthetic spectra in our training system to estimate the stellar parameters of the raw spectra of the targets.

My contribution in this project was examining the impact of persistence on the APOGEE spectra and the StarNet's results. Persistence is a known source of systematic noise in IR detectors. Excess charge from a previous exposure creates an afterglow in the next exposure. The greater the saturation of the detector, the greater the afterglow (see Chapter 2 and Smith et al. 2008). Through our work and also the APOGEE's flags we noticed that significant amount of the APOGEE spectra are affected by this persistence. In particular, the persistence problem is critical on the blue CCD that covers 1.514-1.581 microns wavelength regime (Nidever et al. 2015). Detailed examination of the blue CCDs suggests that over 30% of the APOGEE spectra include persistence with different strength (the diagram of the distribution of the persistence on the CCDs is shown in Fig. 4.1).

Different training sets are used in the StarNet such as synthetic data (from MARCS atmosphere models) and the APOGEE's observed spectra. The preliminary results if the StarNet show that our ML architecture can predict the stellar parameters as accurate as ASPCAP (or in some cases more accurate) in a faster and more efficient manner. The comparison between the StarNet's results and the ASPCAP's results are shown in Fig. 4.2. For the purpose of showing the effect of the

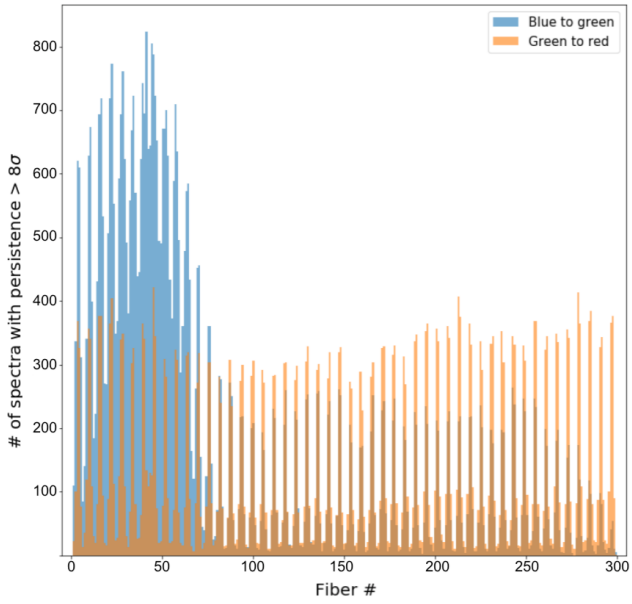

Figure 4.1: The intensity level of the blue, the green and the red chips are compared with respect to each other. The persistence effect is more serious on the blue chip as more than 30% of the blue chip's spectra have a jump in their flux level with respect to the other two chips. Note that a non-negligible number of the green chip's spectra are also slightly affected by the persistence. Plot credit: Spencer Bialek.

persistence on the APOGEE's stars, the StarNet has been trained on the APOGEE's data in order to compare accuracy of the predicted stellar parameters for the spectra with and without the persistence flag. As it is shown in Fig. 4.3, the persistence does not have a critical effect on the StarNet's performance. From our previous studies on the Palomar 1 globular cluster (see Chapter 2), we know that the persistence can strongly bias the ASPCAP results. Our results suggest that even though the StarNet architecture is not sensitive to the persistence, the safer approach is removing the affected spectra from the training set of the ML system.

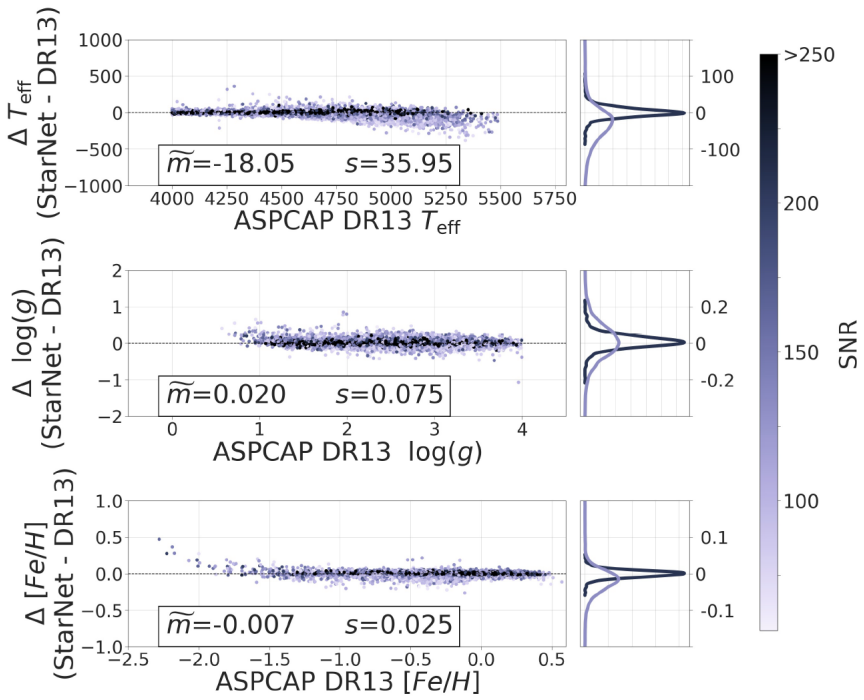

Figure 4.2: Residuals of StarNet predictions and ASPCAP parameters for APOGEE DR13 stars (Fabbro et al. 2017). This prediction of the StarNet is based on a test set of 21037 combined spectra over a large range of SNR and a training set of 41000 individual visit spectra.

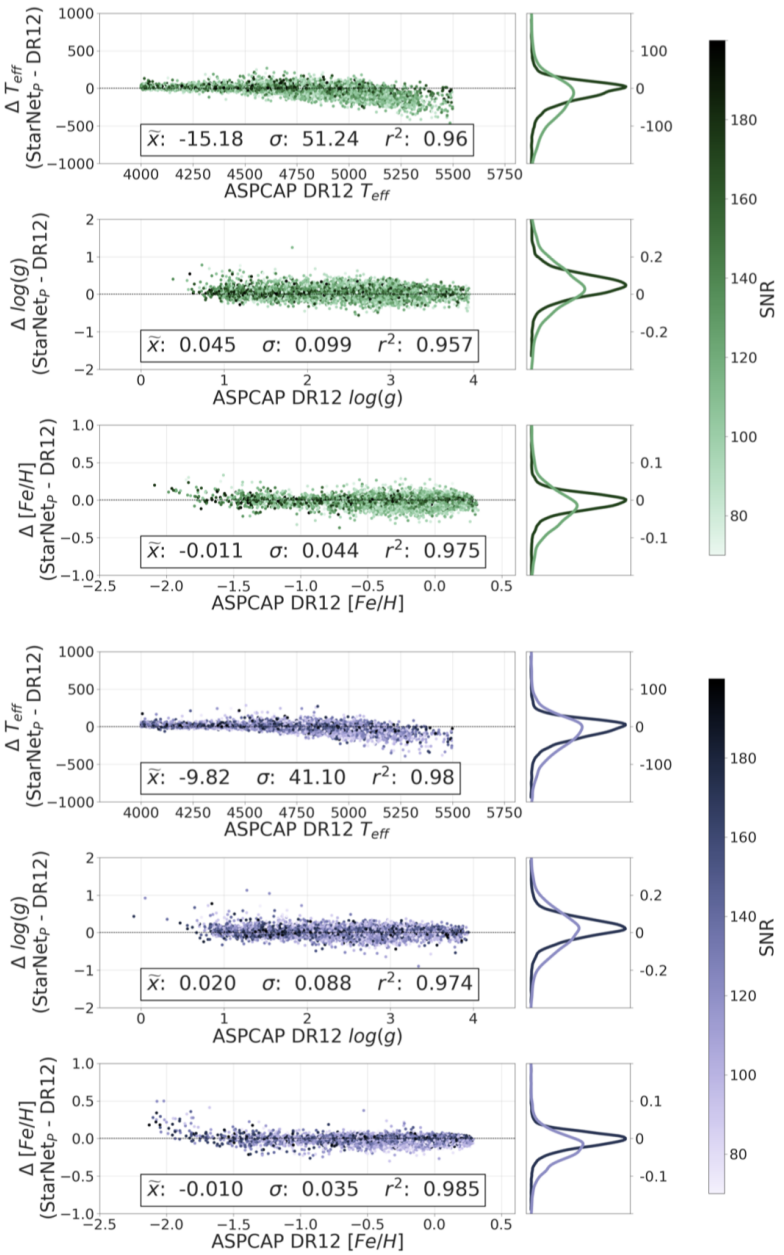

Figure 4.3: Residuals of stellar labels determined by StarNet$_p$ and those from ASPCAP DR12. The StarNet$_p$ training set only includes individual visit spectra labeled with persistence. Two test sets for the stars with persistence (top plot) and without persistence (bottom plot) are used for this comparison. The persistence does not have a critical effect on most of the StarNet's predictions (this plot is from the private communications of the StarNet team).

4.3 Contributions to the Abundance Precision Measurements

Currently, there is not a general technique to determine the systematic limits (i.e. resolution and SNR) for precise abundance measurement of different elements. Therefore, we examined effect of resolution and SNR in the precision of abundance measurements. Through this project, we created multiple synthetic spectra with different SNR and resolution for a single star (i.e. T_{eff}=5000 K, log g=3.5 and [Fe/H]=-2.0) in two different wavelength regions of 399-427 nm and 452-484 nm (i.e. P399 and P452 respectively).

The prominent absorption lines were identified from a line-list generated by MOOG (Sneden 1973) and equivalent widths (EQW) for the chosen lines were measured with IRAF and DAOSPEC programs. IRAF and DAOSPEC are programs used to measure precise EQWs of absorption lines in a spectrum.

- **IRAF** measures the EQW of the lines based on an integration of the pixel values between two points that the user marks, wherein the ideal case the mentioned two points are the edges of the absorption line at the continuum. Through this method, other than the equivalent width; the line centre, the continuum value and the line flux can be determined. Note that for the blended lines we apply Gaussian fitting to separate the blended absorption lines.

- **DAOSPEC** is an automated system that detects different absorption lines using an input line-list, and then by fitting Gaussian profiles to the lines of the input spectra and using the same FWHM for all the lines, it approximates the equivalent width of the lines.

When we compared the EQW-DAO and EQW-IRAF for R=20K and SNR = 30, they are in good agreement up to 100 mÅ. For stronger lines, the Lorentz wings are not matched by the Gaussian fitting.

4.3.1 Abundance Measurements

The synthetic spectrum program MOOG is used to calculate abundances for different elements for a given stellar model atmosphere. The synthetic spectra are over-plotted on our degraded spectra and for each line of each element (see Fig. 4.4-4.6). Each line is fit independently, and the line abundances are averaged together (see Table 4.1 and Table 4.2).

4.3.2 Errors

In this analysis, the random errors in line measurements calculated as follows:

- Each line has a fitting error noted in the table. When these are combined together, they were typically smaller than σ(X).
- For elements with number of lines < 5, error $= \sigma$(X)
- For elements with number of lines > 5, error $= \sigma(\mathrm{X})/\sqrt{N}$

Also in any of the above cases, if the uncertainty is less than σ(Fe), σ(Fe) is used as the uncertainty. The reason is that when we have fewer than 5 lines, we do not have enough number of samples to have a reliable uncertainty σ(X). In most cases, the line uncertainty is smaller than σ(Fe).

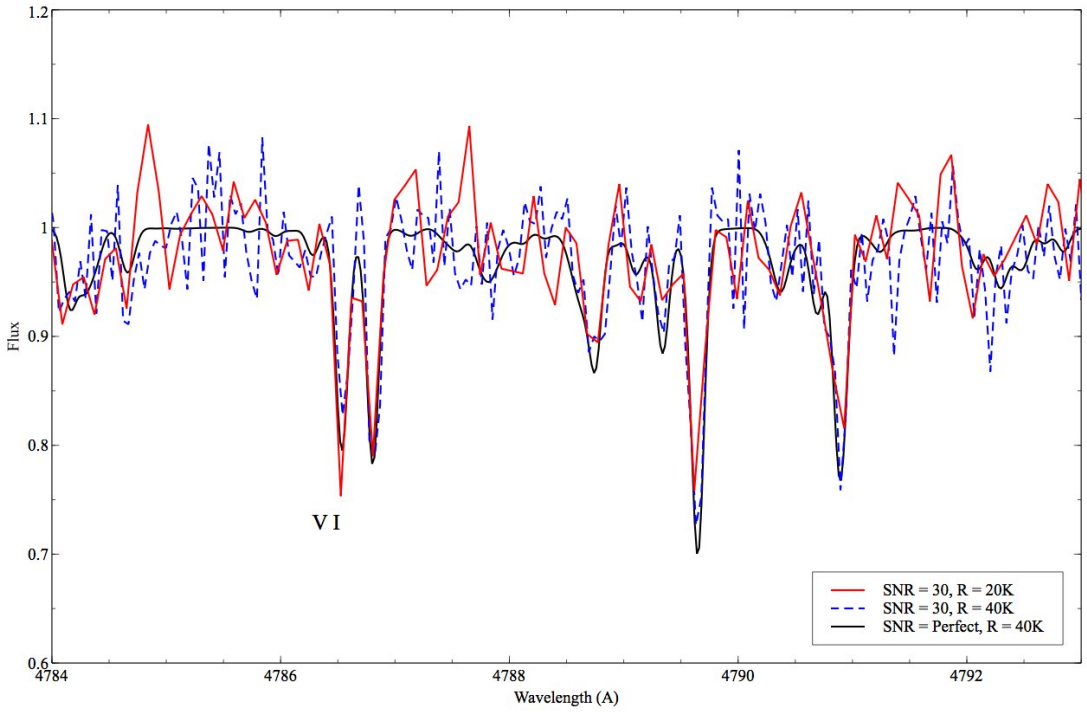

Figure 4.4: Comparison between R=40K and R=20K for the same SNR of 30 and R=40K for SNR >1000. The V I line from Table 4.2 is marked. The resolution affects the measurement of this line due to the nearby blend at R=20K. Note that at wavelength of 4791 Å, there is a blend where two components can be seen in the 40K but not in the 20K.

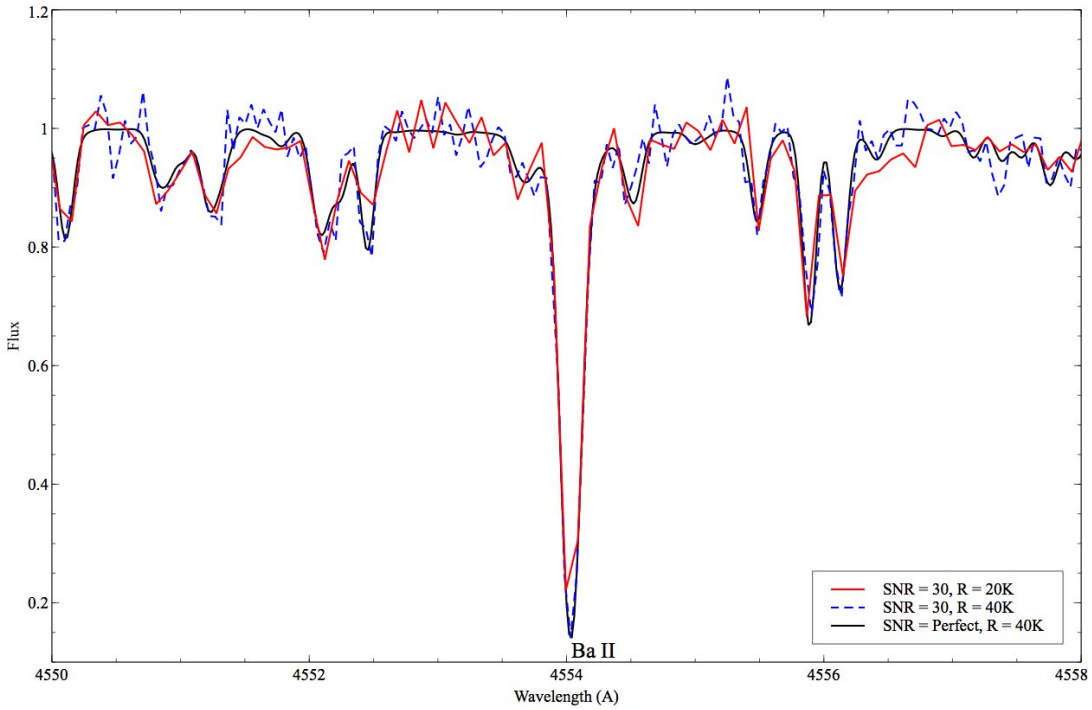

Figure 4.5: Comparison between R=40K and R=20K for the same SNR of 30 and R=40K for SNR >1000. The Ba II line is affected by the hyperfine structure and this means that there are multiple components of the Ba II feature near the same wavelength. This cannot be accounted for as a single equivalent width in the model atmosphere analysis.

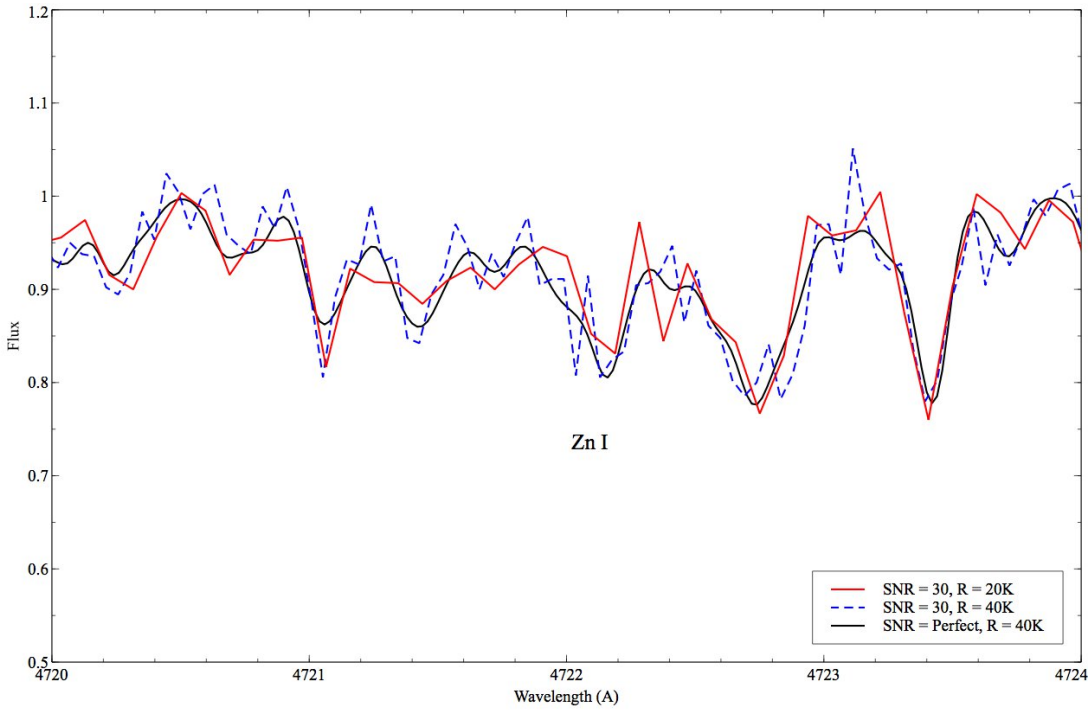

Figure 4.6: Comparison between R=40K and R=20K for the same SNR of 30 and R=40K for SNR >1000. The Zn I line from Table 4.2 is marked. For the R=40K with the highest SNR we can see this line is slightly blended on the blue side. This affects the equivalent width measurement at both resolutions when the SNR is reduced to 30.

Table 4.1: Detailed abundance for different absorption lines in P399 region.

		R=20K, SNR=30			R=40K, SNR=30			R=40K, SNR= Inf		
	lambda (A)	EQW (mA)	Abund. (IRAF)	Abund. (Synth)	EQW (mA)	Abund. (IRAF)	Abund. (Synth)	EQW (mA)	Abund. (IRAF)	Abund. (Synth)
Fe I	4045.812	222	4.4	5.7[0.1]	447	5.1	5.60[0.02]	338	5.0	5.60[0.02]
	4062.441	81	5.6	5.6[0.1]	124	6.2	5.60[0.04]	73	5.4	5.60[0.01]
	4063.594	212	4.7	5.6[0.1]	227	4.8	5.60[0.02]	182	4.5	5.60[0.01]
	4071.738	247	5.0	5.6[0.1]	261	5.0	5.55[0.02]	392	5.4	5.60[0.01]
	4118.55	89	5.3	5.5[0.1]	84	5.2	5.50[0.08]	87	5.3	5.60[0.05]
	4132.058	207	5.4	5.7[0.1]	183	5.3	5.70[0.10]	197	5.4	5.60[0.05]
	4143.868	213	5.3	5.7[0.1]	176	5.0	5.55[0.05]	167	5.0	5.60[0.02]
	4147.67	85	5.4	5.5[0.1]	94	5.6	5.70[0.06]	88	5.5	5.60[0.03]
	4172.76	307	7.6	<6.1	146	6.7	<6.20	131	6.6	5.70[0.01]
	4181.75	140	5.8	<6.1	132	5.7	<6.20	134	5.8	5.60[0.03]
	4187.05	127	5.3	<5.9	118	5.4	5.70[0.02]	109	5.2	5.70[0.00]
	4187.81	81	5.5	5.9[0.2]	128	5.5	<6.00	127	5.4	5.80[0.00]
	4198.33	181	6.0	6[0.2]	185	6.0	5.70[0.02]	178	5.9	5.80[0.00]
	4199.1	121	5.3	5.9[0.1]	118	5.3	5.80[0.10]	116	5.2	5.60[0.03]
	4202.029	167	5.1	5.7[0.1]	164	5.0	5.70[0.11]	171	5.1	5.70[0.02]
	4216.19	117	5.7	5.7[0.1]	131	5.9	5.70[0.06]	112	5.6	5.70[0.00]
	4222.22	109	5.7	5.7[0.1]	104	5.6	5.60[0.05]	141	6.0	5.60[0.01]
	4227.44	171	5.8	5.7[0.1]	132	5.5	5.90[0.10]	149	5.7	5.70[0.03]
	4233.61	109	5.3	5.7[0.1]	118	5.4	5.60[0.10]	120	5.5	5.70[0.01]
	4235.95	187	5.7	<6.2	124	5.2	5.90[0.10]	141	5.4	5.60[0.00]
	4250.8	182	5.3	5.6[0.1]	204	5.4	5.55[0.10]	179	5.2	5.60[0.01]
	4260.474	182	5.3	5.7[0.1]	150	5.0	5.70[0.05]	187	5.3	5.70[0.01]
Avg			5.5[0.1]	5.7[0.1]		5.5[0.1]	5.67[0.02]		5.5[0.1]	5.68[0.00]
Fe II	4178.86	86	5.6	—	86	5.5		81	5.6	—
	4233.17	127	6.3	—	121	6.6		120	6.6	—
Avg			6.0[0.5]			6.1[0.7]			6.1[0.7]	
Mg I	4057.52	37	5.6	5.7[0.2]	35	5.5	5.70[0.10]	28	5.4	5.60[0.03]
	4167.28	95	6.0	5.9[0.2]	86	5.9	5.80[0.20]	94	6.0	5.65[0.00]
Avg			5.8[0.3]	5.8[0.2]		5.7[0.3]	5.75[0.15]		6.0[0.7]	5.68[0.02]
Si I	4102.936	133	6.3	5.7[0.1]	165	6.6	5.71[0.14]	135	7.0	5.60[0.03]
Ca I	4226.728	396	4.1	4.6[0.1]	246	3.6	4.64[0.08]	366	4.3	4.64[0.02]
Sc II	4246.822	138	1.6	—	149	1.7	—	140	1.6	—
Ti I	3998.64	87	3.1	3.1[0.1]	87	3.1	3.05[0.04]	81	3.0	3.00[0.01]
	4008.93	51	3.3	<3.2	50	3.2	3.15[0.06]	35	2.9	3.00[0.02]
Avg			3.2[0.1]	3.1[0.1]		3.2[0.1]	3.10[0.05]		3.0[0.0]	3.00[0.02]
Ti II	4012.385	63	2.8	—	66	2.8	—	63	2.8	—
	4025.12	52	3.0	—	41	2.7	—	46	2.8	—
	4028.343	76	3.9	—	85	4.1	—	80	4.0	—
	4053.83	39	3.4	—	35	3.3	—	24	3.0	—
	4161.53	31	3.2	—	25	3.1	—	25	3.1	—
	4163.63	34	3.2	—	39	3.3	—	41	3.4	—
	4184.31	77	4.5	—	75	4.5	—	78	4.5	—
Avg			3.4[0.2]			3.4[0.2]			3.4[0.2]	
Cr I	4254.332	165	3.4	3.7[0.2]	177	3.4	3.70[0.20]	181	3.5	3.74[0.02]
Mn I	4030.753	190	3.3	3.5[0.1]	58	1.3	3.53[0.03]	204	3.4	3.53[0.03]
	4033.062	210	3.8	3.5[0.1]	224	3.2	3.53[0.11]	230	3.4	3.50[0.02]
	4034.483	179	3.7	3.5[0.2]	176	3.0	3.53[0.10]	168	3.4	3.53[0.00]
	4041.36	103	3.8	3.5[0.1]	113	3.9	3.53[0.04]	101	3.7	3.53[0.02]
Avg			3.6[0.]	3.5[0.1]		2.9[0.5]	3.53[0.07]		3.5[0.1]	3.53[0.06]
Co I	3995.302	109	3.3	3.1[0.1]	108	3.3	3.09[0.04]	105	3.3	3.09[0.01]
	4020.9	43	3.2	3.1[0.1]	45	3.3	3.09[0.04]	34	3.1	3.09[0.01]
	4110.53	56	3.2	3.1[0.1]	40	2.9	3.09[0.07]	38	2.9	3.09[0.01]
	4121.311	100	3.2	3.1[0.1]	95	3.1	3.09[0.04]	97	3.2	3.09[0.03]
	4118.767	101	3.6	3.1[0.1]	101	3.6	3.09[0.04]	85	3.3	3.09[0.04]
Avg			3.3[0.1]	3.1[0.1]		3.2[0.1]	3.09[0.04]	—	3.1[0.1]	3.09[0.02]
Sr II	4077.71	167	0.7	—	173	0.7	—	159	0.6	—
	4215.52	155	0.9	—	147	0.8	—	165	0.9	—
Avg			0.8 [0.1]			0.8 [0.1]	—	—	0.8[0.2]	
Zr II	4208.98	13	0.5	—	22	0.8	—	11	0.5	—
		—	—	—	—	—	—	—	—	—
Eu II	4129.7	43	-0.6	—	32	-0.8	—	27	-1.0	—

Note. Detailed Abundance of each line for P399 region. Note that the uncertainty of equivalent width is calculated using Cayrel method and is 7 mA and 3.5 mA for R=20K nd R=40K respectively.

Table 4.2: Detailed abundance for different absorption lines in P452 region.

		R=20K, SNR=30			R=40K, SNR=30			R=40K, SNR= Inf		
	lambda (A)	EQW (mA)	Abund. (IRAF)	Abund. (Synth)	EQW (mA)	Abund. (IRAF)	Abund. (Synth)	EQW (mA)	Abund. (IRAF)	Abund. (Synth)
Fe I	4531.15	96	5.6	5.5 [0.1]	86	5.4	5.60[0.03]	89	5.4	5.60[0.00]
	4592.66	75	5.6	5.5 [0.1]	69	5.5	5.50[0.04]	78	5.7	5.50[0.00]
	4602.95	84	5.4	5.5 [0.1]	83	5.4	5.50[0.04]	87	5.5	5.50[0.00]
	4691.41	46	5.7	5.5[0.1]	49	5.7	5.50[0.03]	43	5.6	5.50[0.00]
	4707.27	49	6.8	5.6[0.1]	65	7.1	5.50[0.04]	52	6.8	5.55[0.00]
	4710.28	25	5.4	5.5[0.1]	45	5.8	5.50[0.04]	30	5.5	5.50[0.00]
	4727.4	39	6.0	5.7[0.3]	33	5.9	5.70[0.03]	28	5.7	5.50[0.00]
	4733.59	68	5.9	5.7[0.1]	52	5.6	5.60[0.10]	46	5.4	5.60[0.02]
	4736.77	94	5.9	5.8[0.1]	72	5.6	5.60[0.01]	49	5.2	5.60[0.01]
	4741.53	73	6.2	5.8[0.1]	44	5.7	<5.8	35	5.5	5.75[0.04]
Avg			5.9[0.1]	5.6[0.1]		5.8[0.1]	5.60[0.05]		5.7[0.1]	5.60 [0.0]
Fe II	4520.22	42	5.8	—	55	6.0	—	35	5.6	—
	4541.52	37	6.1	—	40	6.2	—	39	6.2	—
	4555.89	50	5.6	—	45	5.5	—	44	5.5	—
	4576.34	34	6.1	—	29	6.0	—	29	6.0	—
	4582.84	17	5.7	—	8	5.2	—	11	5.5	—
	4583.83	84	6.0	—	74	5.8	—	75	5.8	—
	4629.34	73	6.2	—	70	6.1	—	59	5.9	—
	4731.45	29	6.3	—	16	6.0	—	16.0	6.0	—
Avg			6.0[0.1]			5.9 [0.1]			5.8[0.1]	
Mg I	4703	90	5.7	5.6[0.1]	89	5.7	5.70[0.04]	83	5.6	5.65[0.01]
Sc II	4670.41	8	0.8		15	1.1		13	1.0	
Ti I	4533.25	62	2.8	3.0[0.1]	73	3.1	3.00[0.01]	80	3.2	2.95[0.00]
	4534.78	72	3.2	3.0[0.1]	65	3.1	3.00[0.01]	61	3.0	2.95[0.00]
	4535.57	68	3.3	3.0[0.1]	47	2.9	3.00[0.07]	39	2.7	2.95[0.03]
	4544.69	27	3.1	3.1[0.1]	14	2.8	3.00[0.08]	22	3.0	2.95[0.03]
	4548.76	15	2.6	3.2[0.1]	30	3.0	3.10[0.10]	31	3.0	3.05[0.03]
	4681.91	38	3.0	3.1[0.1]	35	2.9	3.00[0.01]	28	2.8	3.00[0.00]
Avg			3.0[0.1]	3.1[0.1]		3.0[0.1]	3.00[0.05]		3.0[0.1]	2.98[0.02]
Ti II	4529.47	25	3.5	—	15	3.2	—	12	3.1	—
	4533.969	96	3.3	—	90	3.2	—	101	3.4	—
	4545.14	29	2.9	—	16	2.5	—	8	2.2	—
	4563.761	74	3.0	—	83	3.2	—	74	3.00	—
	4568.31	18	3.5	—	5.5	2.9	—	12	3.3	—
	4571.968	129	3.9	—	121	3.8	—	113	3.7	—
	4583.41	7	3.2	—	2.3	2.7	—	3.1	2.8	—
	4589.96	25	2.9	—	29	2.9	—	26	2.9	—
	4657.21	16	3.2	—	11	3.0	—	9	2.8	—
	4763.88	23	3.5	—	20	3.4	—	23	3.4	—
	4779.99	19	3.2	—	11	2.9	—	17	3.1	—
	4798.53	28	3.6	—	12	3.2	—	12	3.2	—
	4805.09	32	3.3	—	19	2.9	—	28	3.2	—
Avg			3.3[0.1]			3.1[0.1]			3.1[0.1]	
V	4786.5	31	4.0	2.3[0.1]	22	3.8	2.30[0.04]	28	3.9	2.00[0.00]
Cr I	4580.06	28	3.6	3.6[0.1]	48	3.9	3.70[0.10]	30	3.7	3.64[0.02]
	4588.2	4	5.1	<3.7	9	5.5	3.70[0.10]	10	5.5	3.69[0.01]
	4600.75	47	3.7	3.6[0.1]	44	3.6	3.60[0.10]	43	3.6	3.64[0.01]
	4616.14	60	3.8	3.6[0.1]	58	3.8	3.70[0.10]	50	3.6	3.69[0.03]
	4646.17	177	5.0	3.8[0.2]	55	3.3	3.70[0.20]	83	3.8	3.78[0.05]
	4651.28	47	3.8	3.7[0.1]	37	3.6	3.60[0.10]	43	3.8	3.76[0.04]
	4652.16	71	3.9	3.7[0.1]	66	3.8	3.70[0.10]	71	3.9	3.76[0.03]
Avg			4.0[0.2]	3.7[0.1]		3.7[0.1]	3.70[0.10]		3.7[0.1]	3.71[0.03]

P452

		R=20K, SNR=30			R=40K, SNR=30			R=40K, SNR= Inf		
	lambda (A)	EQW (mA)	Abund. (IRAF)	Abund. (Synth)	EQW (mA)	Abund. (IRAF)	Abund. (Synth)	EQW (mA)	Abund. (IRAF)	Abund. (Synth)
Cr II	4824.13	34	4.5	—	19	4.2	3.90[0.10]	23	4.3	—
	4588.2	5	3.2	—	13	3.6	3.70[0.10]	10	3.6	—
	4558.65	26	4.0	—	19	3.9	3.80[0.10]	18	3.9	—
Avg			3.9[0.7]			3.9[0.3]			3.8[0.3]	
Mn I	4754.04	74	3.7	3.5[0.1]	63	3.5	3.40[0.05]	65	3.5	3.43[0.01]
	4762.37	33	3.1	<3.4	47	3.4	3.50[0.08]	43	3.3	3.43[0.01]
	4783.43	66	3.5	3.4[0.1]	72	3.6	3.40[0.04]	72	3.5	3.43[0.03]
	4823.524	69	3.4	3.5[0.1]	82	3.7	3.60[0.10]	78	3.6	3.53[0.05]
Avg										
Ni I	4648.66	32	4.3	4.2[0.1]	31	4.3	4.20[0.05]	27	4.2	4.22[0.03]
	4714.42	69	4.5	4.3[0.1]	71	4.5	4.20[0.03]	54	4.2	4.22[0.00]
Avg			4.4[0.1]	4.3[0.1]		4.4[0.1]	4.20[0.05]		4.2 [0.1]	4.22[0.01]
Zn I	4722.153	15	2.6	2.6[0.1]	21	2.8	2.60[0.03]	13	2.6	2.56[0.00]
	4810.54	28	2.9	2.6[0.1]	18	2.6	2.60[0.03]	15	2.5	2.61[0.02]
Avg			2.8 [0.2]	2.6[0.1]		2.7 [0.1]	2.60[0.04]		2.6[0.1]	2.58[0.01]
Ba II	4554.03	173	0.9	0.3[0.1]	190	1.0	0.28[0.04]	182	0.9	0.20[0.04]

Note. Detailed Abundance of each line for P452 region. Note that the uncertainty of equivalent width is calculated using Cayrel method and is 7 mA and 3.5 mA for R=20K nd R=40K respectively.

In the above tables, differences between EQW measurements and synthetic spectrum matching can be seen in abundance determination for individual lines. We find the difference in SNR = 30 and SNR >1000 for the R=40K spectra is not very significant. However the differences between R=40K and R=20K at SNR =30 can be larger than 1σ errors.

4.3.3 Future Work

The possible potentials of using ML techniques are examined using the StarNet neural network. In total 340 synthetic spectra for a single star with different resolution (i.e. 40000 and 20000), SNR (i.e. 30, 60, 100, 150, 200, 250, 300, 350, 400 and 450) and Ba II abundance range of -1.5 dex to 1.4 dex are generated. The Ba II is chosen as the test candidate because our previous IRAF-based results showed that Ba II could be very sensitive to the SNR of the spectra. The training set and the test set contain 17 and 323 number of spectra respectively. Our preliminary result shows a promising prediction of the abundance using the same neural network as the StarNet (see Fig. 4.7). In our future work, other elements as well as different stellar parameters such as the effective temperature, metallicity and gravity of the optical spectra will be examined.

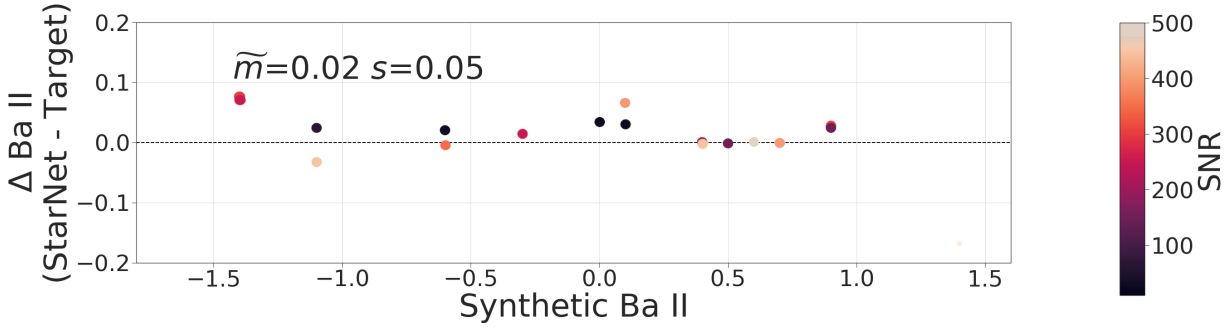

Figure 4.7: Comparison between the real abundance of Ba II and the estimated abundance from the StarNet. All the predictions are within 0.1 dex of the real abundance, which suggests the StarNet architecture can be used for the optical spectra as well as the IR spectra.

4.4 Spectral Classification of Supernovae Using Unsupervised Machine Learning

The spectra of supernovae Type Ia are examined with the goal of classification of the sub-classes of this type of supernovae. In total, over 300 spectra of supernovae Type Ia are extracted from different surveys between 1979 to 2006 (the data are extracted, calibrated and normalized by Muthukrishna 2016). For this work, we chose the data within five days from the maximum peak of the light curve (138 spectra). The five-day range is chosen as the strength of the absorption lines decreases dramatically before and after a few days from the maximum emission of the light. Unsupervised machine learning and vector quantization methods such as K-mean (MacQueen et al. 1967) and SOM (Kohonen 1990) techniques are used distinctively:

- **K-means** is an unsupervised clustering technique for classification of a mixed and unclassified group of data. In this method the only known parameter is the total number of clusters or K-variable, that must be provided by the user. The main mechanism of this technique is clustering data based on their similarity through the K-mean algorithm that assigns each point in one of the K number of groups. The K-mean algorithm defines the similarity between data points based on their distance from random centroid guesses. Therefore, its objective is finding centroids with minimum distances from each point using the following function (see Fig. 4.8):

$$A = \Sigma_{j=1}^{k} \Sigma_{i=1}^{n} ||x_i^j - c_j||^2 \tag{4.1}$$

  where $||x_i^j - c_j||^2$ is the distance between the data point (i.e. x_i^j) and the centroid c_j, k is the number of clusters and n is the number of points.

- **Self-Organizing Map (SOM)** is a data visualization technique, which can classify high-dimensional data (such as the spectrum of an astronomical object) based on their nonlinear statistical relationships. This unsupervised neural network trains itself using the input data as artificial neurons and locates each data based on the similarity between each group in a high-dimensional grid that the user defines. Through the learning and classification process, the position of each data point gradually changes to optimize the system based on the similarity between each point and its neighbourhood (see Fig. 4.9).

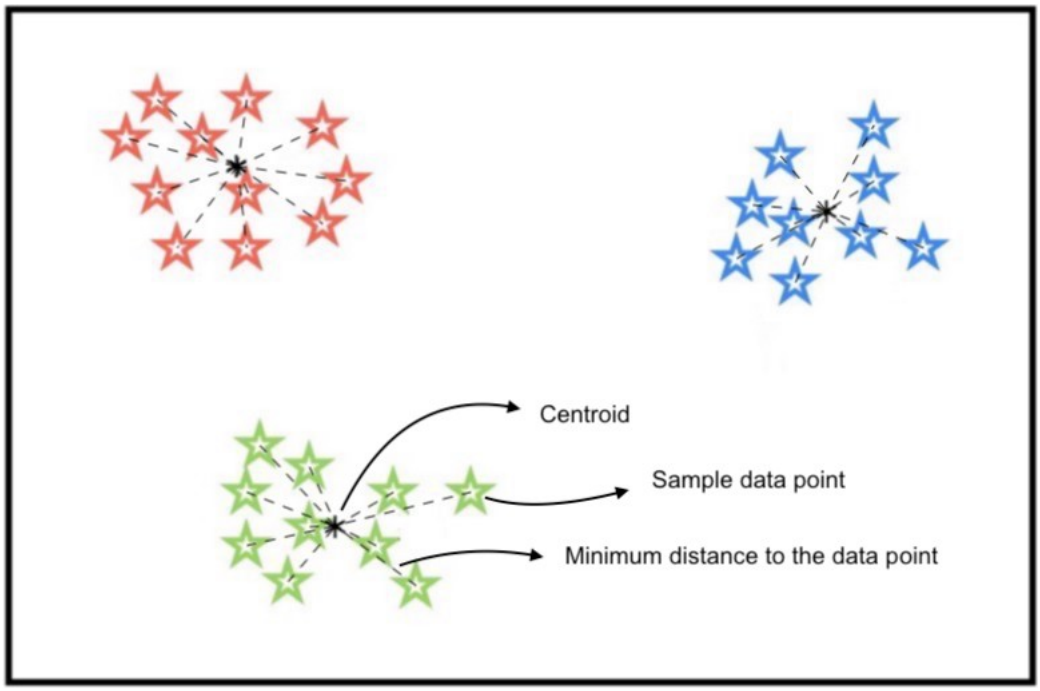

Figure 4.8: The K-mean algorithm determines the position of centroids based on their minimum distance from each cluster's data point. Note that number of centroids is the only user-variable in this vector quantization method.

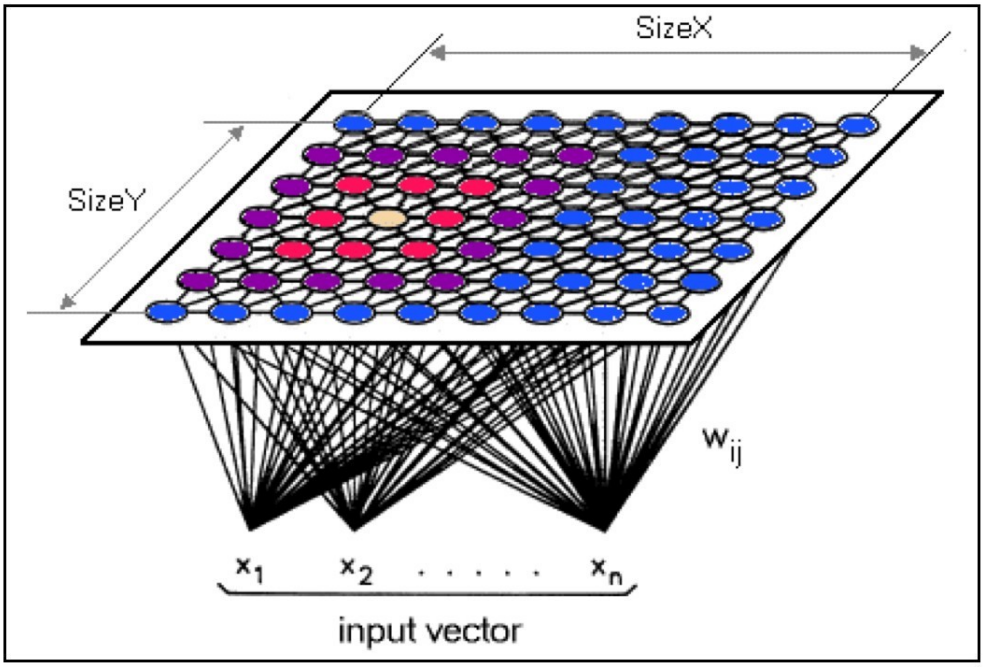

Figure 4.9: The SOM creates a correlation map from the input data (i.e. $x_1 ... x_n$) onto a high dimensional array of nodes (i.e. with dimensions of X and Y). The SOM classification is based on the topological relationships in the input's data. Note that unlike the K-mean method, each node of the SOM is defined by a vector w_{ij} that gradually changes during the training in order to optimize the map. Image credit: http://www.lohninger.com/helpcsuite/kohonen_network_-_background_information.htm

4.4.1 Preliminary results

The preliminary results of the K-mean analysis suggest that there are at least three distinct subclasses with different spectrum pattern (see Fig. 4.10). This result is also consistent with results from Sasdelli et al. (2016).

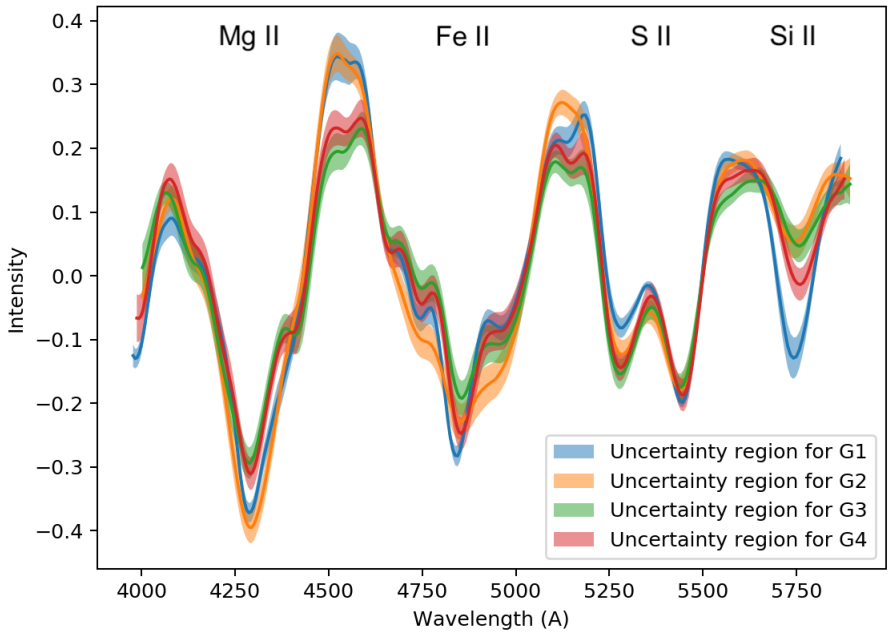

Figure 4.10: The K-mean results for the SNIa spectra. In total four groups with 17, 30, 39 and 40 supernovae (i.e. G1, G2, G3 and G4 respectively) are classified, and the contents of each group are median-combined. Note that the colour band around each line is the uncertainty area for each group, which is determined from the standard deviation of the members in the groups.

Parallel to the K-mean analysis, the SOM technique is applied to the raw spectra. Multiple different neuron structures are examined (see Fig. 4.11 and Fig. 4.12). The SOM results are in close agreement with the K-mean clusters, which both suggest that we have three distinct sub-classes in our SNIa dataset and one debatable cluster, G4.

In our follow-up studies, we will increase the size of our dataset by increasing number of spectra and adding photometric data of the supernovae. In addition, the sub-classes of other types of supernovae will be examined.

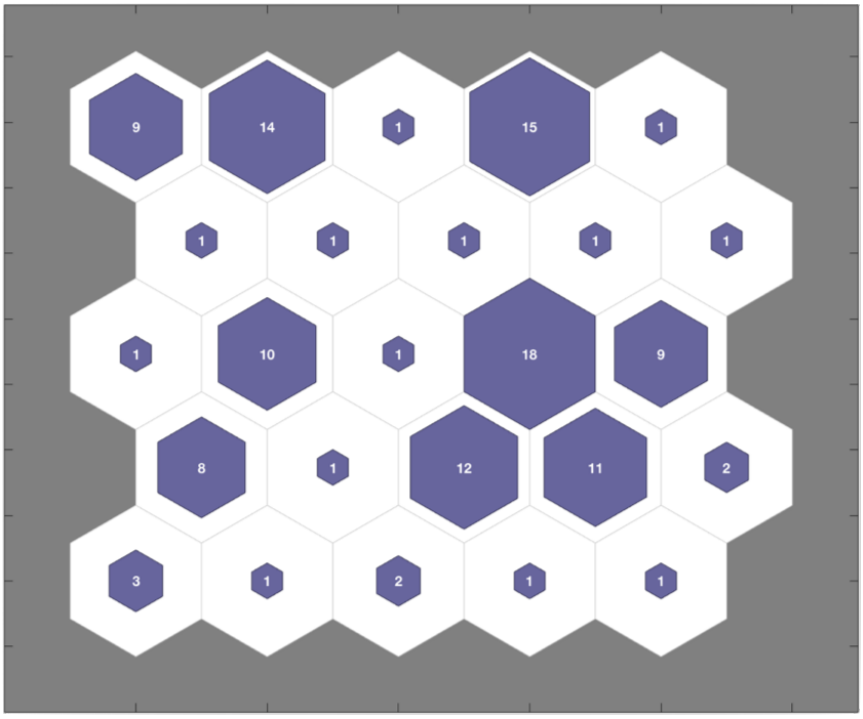

Figure 4.11: SOM of the supernovae Type Ia spectra in a 5x5 dimensional grid. Each neuron shows the number of the supernovae spectra in the corresponding group and the size of the coloured node is based on the relative number of vectors for each neuron.

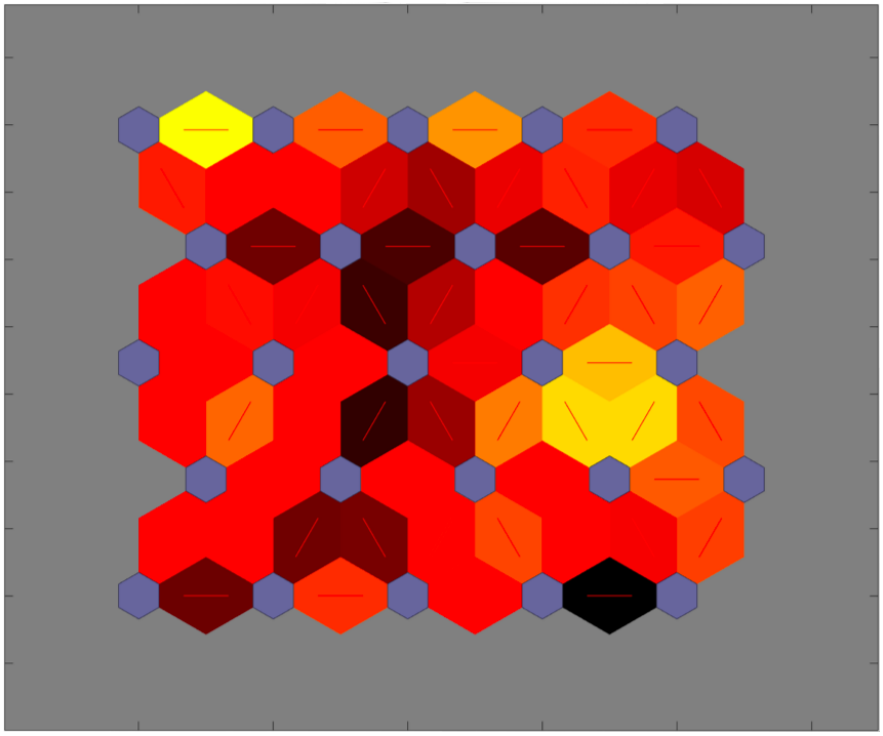

Figure 4.12: The SOM of the supernovae Type Ia spectra in a 5x5 dimensional grid. The relationship between each node is shown in coloured patches from black to yellow based on how similar each neurons weight vector is to its surrounding nodes (i.e. the colour becomes lighter as the nodes become more similar)

4.4.2 Summary

Three different applications of machine learning in astronomy were examined. Supervised machine learning techniques are used for both infrared and optical spectra of red giant stars, and their stellar parameters are determined. The effects of persistence on the overall performance of our machine learning algorithms was negligible, however further studies are required. In addition, unsupervised machine learning is used for classification of sub-classes of supernovae (SN) Type Ia. The K-mean and the Self-organized Map (SOM) were used in this analysis. The preliminary results suggest multiple distinct sub-classes in the SN Type Ia spectra. In future work, spectra and photometric data of different types of SN (i.e. Type Ib, Ic and II) will be added in the database to examine other SN subclasses efficiently and accurately.

Chapter 5

Automated Testing of Optical Fibres for Maunakea Spectroscopic Explorer Project

This is a team project in instrumental astronomy and engineering, conducted with Stephanie Monty and Jooyoung Lee, under supervision from Colin Bradley, Darren Erickson, David Crampton, and Kim Venn. The software development and post-processing steps of this work was led by me.

5.1 Introduction

Optical fibre transmission technology has made a significant improvement in the last few decades, becoming an efficient method for use in astronomy. The Maunakea Spectroscopic Explorer (MSE) project is an example of a multi-object spectroscopy facility that has a fibre transmission system and is designed to be a complementary for Canada-France-Hawaii telescope (CFHT). In fact, the MSE project will transform the CFHT into a new spectroscopic facility with a 11.25 m telescope and wide field of view of 1.5 $\deg^2$ that covers the wavelength range of 0.36-1.8 μm. This facility will use optical fibres and transmission systems for multiple spectrographs with different resolutions from 2000 to 40000.

The internal Fibre transmission systems (FiTS) is the critical part of the MSE project that is designed to include over 4300 optical fibres to transmit the light from the primary focus of the telescope to the spectrographs in the facility. The primary objective of FiTS project is to transmit the selected light from the focal plane to the MSE spectrographs efficiently. However, there are several challenges in any fibre-based system as the optical fibres do not conserve the etendue of the system. Therefore, several techniques are invented to examine the efficiency and the data loss in the fibres. The examination of the focal ratio degradation (FRD) is one of the

techniques that shows the change in the light's angular distribution as the light propagates through the fibre. The relative FRD can be examined through the ring test (see Fig. 5.1). This method is especially crucial in astronomy as there is a correlation between the FRD and the signal loss. Thus, it is critical to minimize and examine the FRD to improve the efficiency of the system. The current science requirements for MSE project is optical fibres with 1% consistency and FRD of less than 5%. This chapter presents the preliminary results from the UVic's FiTS team that includes the full automation of the ring test for fast, repeatable, and efficient measurements of an individual fibre in multi-fibre bundles.

5.2 Ring Test

At UVic, we have used the standard collimated beam method, or "ring test," to measure the FRD of the MSE-like fibres. The ring test is when the output light from a fibre is not centrally concentrated but is instead distributed in a ring-like pattern due to a high incident angle when the light is injected into the fibre (Fig. 5.1).

In the ring test, the incident light angle is correlated with the input f-number through the relation:

$$f_{in} = \frac{1}{2tan(\theta)} \tag{5.1}$$

where f_{in} is the input f-number and θ is the incident angle.
The ratio of the FWHM to the radius of the output annulus determines the FRD of the system. This method examines the quality of the fibre quantitatively by demonstrating the signal loss in the output ring for different f-numbers.
Our experimental setup for the ring test is shown in Fig. 5.2. This setup includes a high-resolution 4K camera, two optical fibres, a blue light source (460 nm), a high precision rotation mount and a collimator. Increasing the input angle increases the size of the output ring with minimum change in the FWHM of the ring. Therefore, from the equation 5.1, the greater incident angle corresponds to the smaller f-number. For the MSE project, since the MSE spectrographs are optimized for an f-number of 2, we are interested in the FRD at the incident angle of 14 degrees (from equation 5.1). Note that the increase in the size of the ring results in a significant decrease in the brightness of the ring. Therefore, the brightness has to be controlled by changing the exposure time of the system in order to have a consistent results.

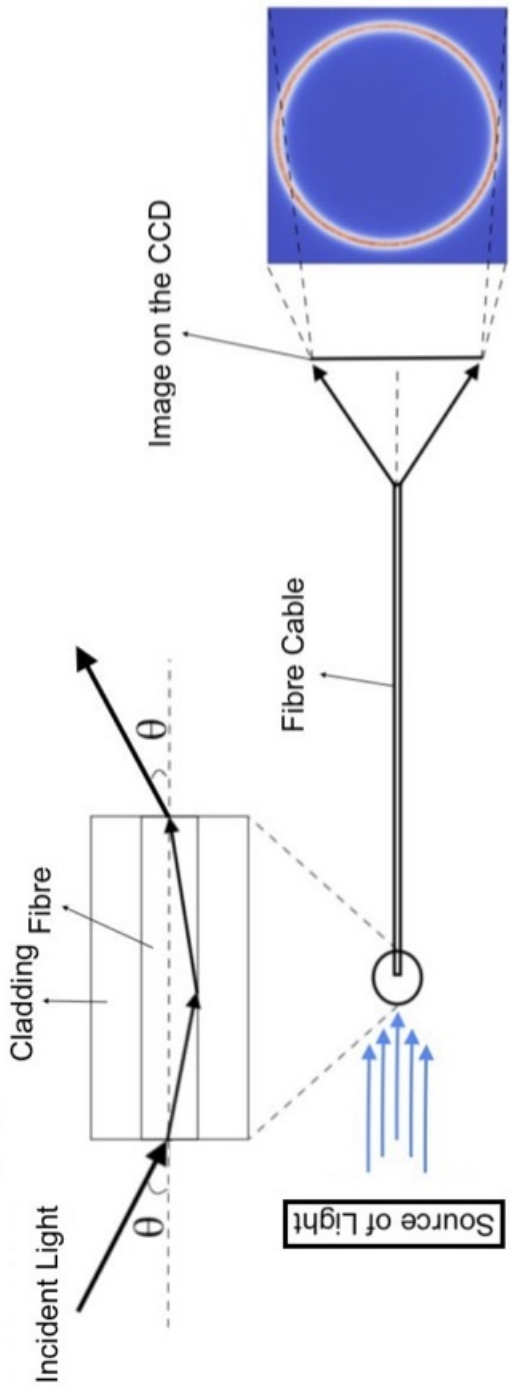

Figure 5.1: Different incident angles can form a ring-shape output from the optical fibres and the FRD of the system can be determined by examination of the ring.

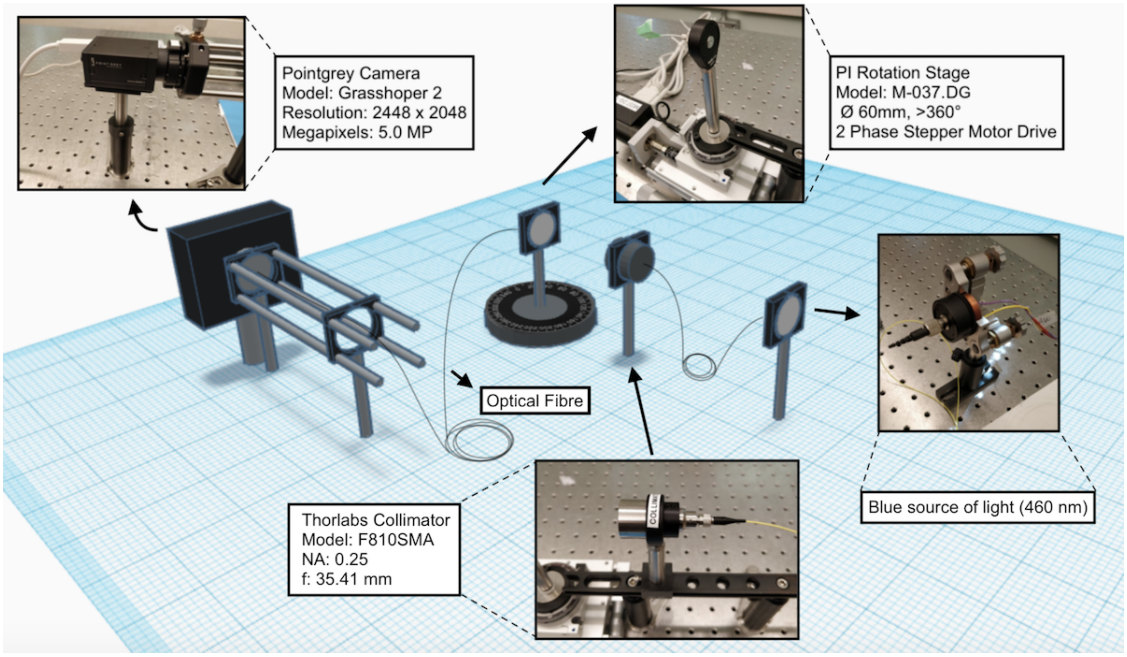

Figure 5.2: The diagram of the ring test setup.

5.2.1 Automation of the Ring Test

Ring test analysis is an essential way of checking efficiency and quality of optical fibres, but the process can be time consuming. We have developed a multilayer software for automation of the ring test. Our final master Python software controls the camera, calibrates the system, controls the stages and analyzes the output data (see Fig. 5.3).

5.2.2 Data Analysis for the Ring Test

The data analysis part of our software has a critical role in the FRD examination. We introduce The Ring Analyzer Python Interface for ring-test Data (RAPID) that let the user control and examine the analysis steps of the output ring image. This interface is shown in Fig. 5.4. The RAPID requires the following six variables from the user:

- Name = Name of the image file
- Dim1 and Dim2 = The x and y dimensions of a horizontal slice from the ring
- Smoothing Factor = This value will be added or subtracted from default smoothing factor of 20

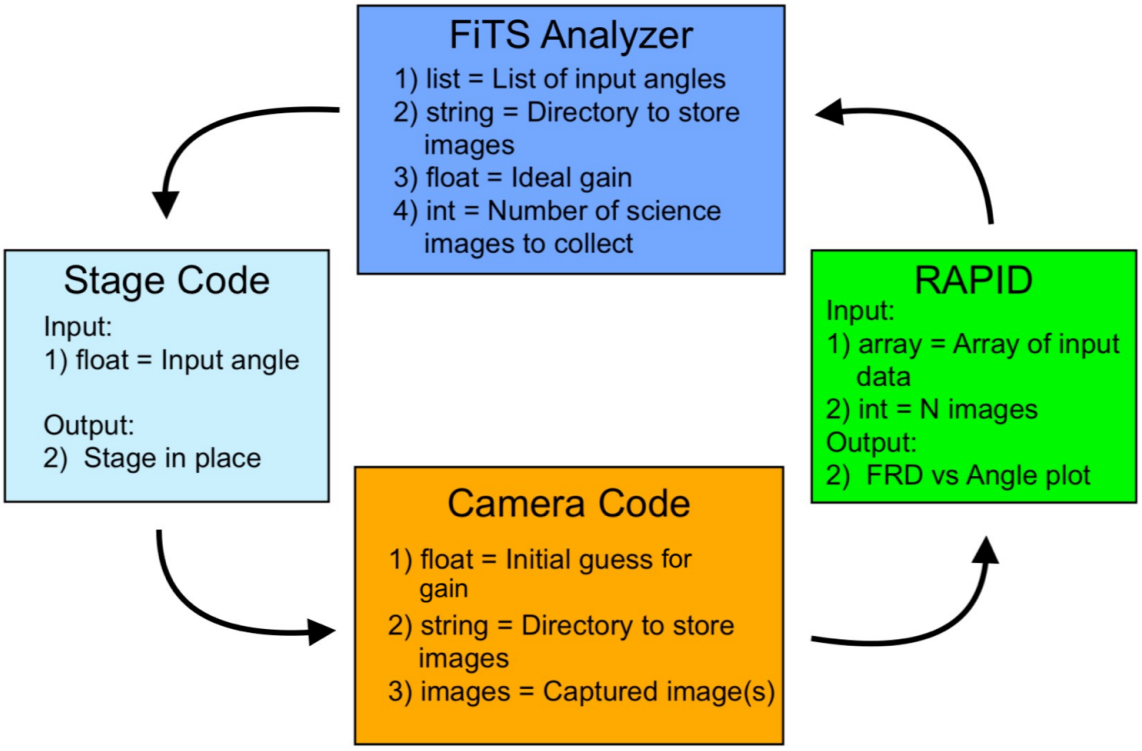

Figure 5.3: The overal structure of our master Python wrapper. The FiTS Analyzer window is the only visible feature to the user and all the other parts are built-in scripts.

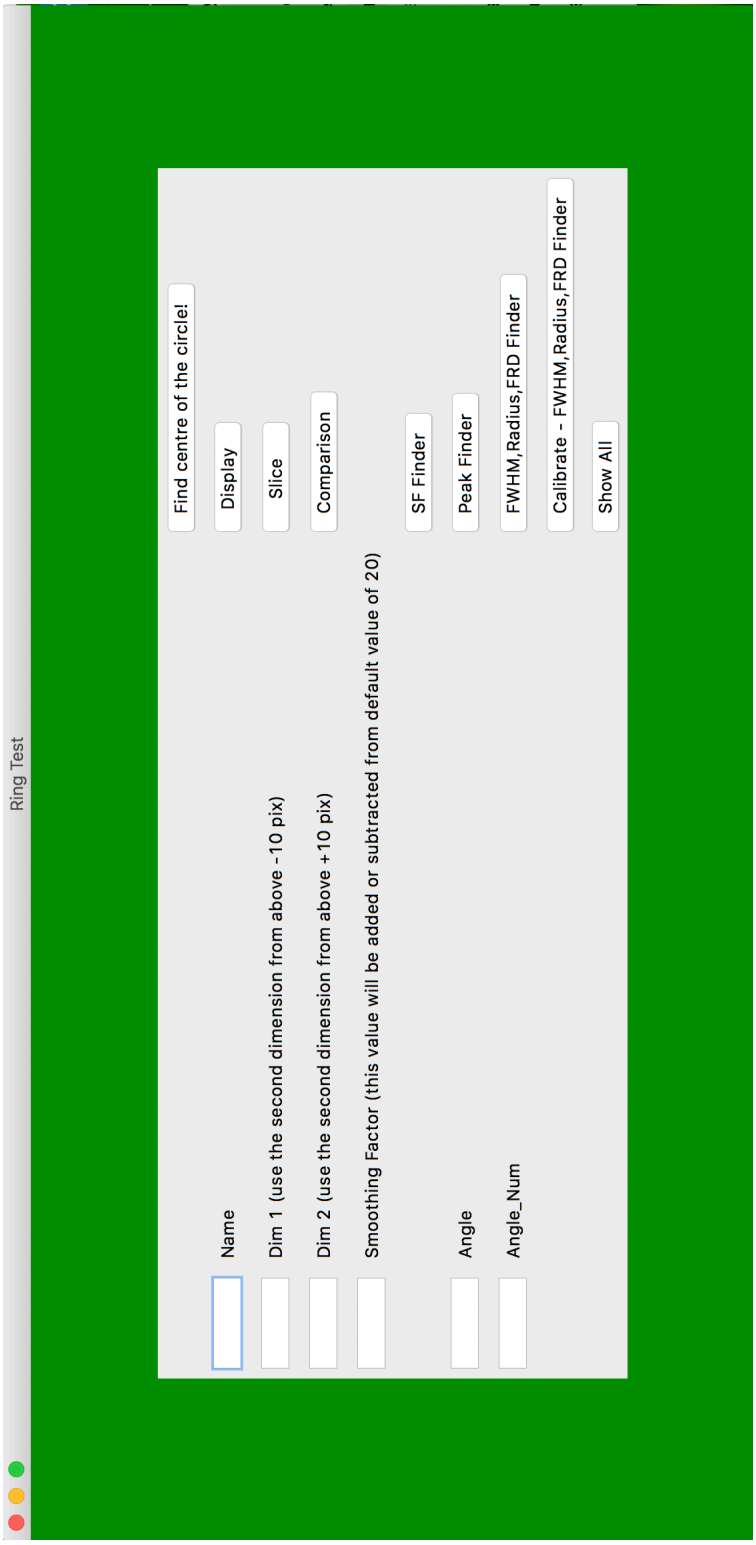

Figure 5.4: The input window of the RAPID. The interface requires six variable from the user and can perform nine different functions.

- Angle = The image will be rotated with respect to this input angle
- Angle_{Num} = Rotates the image multiple times with respect to the random angles

The following functions are defined in RAPID:

- Find center of the circle: Determines the center of the circle in pixels.
- Display: Displays the input image as a whole and also a slice of it based on the Dim1 and Dim2 values (see Fig. 5.5).
- Slice: Plots intensity vs pixel number graph based on the chosen slice (from Dim1 and Dim2, see Fig. 5.6).
- Comparison: Compares the raw data with the smoothed version of it.
- SF Finder: Helps to find the best smoothing factor by giving the mean of difference between the smoothed graph and the original graph.
- Peak Finer: Finds peaks of the plot generated from the slice function (see Fig. 5.7).
- FWHM, Diameter, FRD Finder: Determines the diameter of the circle (in pixels), fits a spline polynomial to the gaussians and calculates the Full Width Half Maximum (FWHM) and also the Focal Ratio Degradation (FRD) of the ring (see Fig. 5.8).
- Calibrate - FWHM, Radius, FRD Finder: Rotates the image several times with random angles and determines FWHM, Diameter and FRD Finder of the system (the final result includes standard deviation of the measurments).
- Show All - Determines FRD of multiple rings in multiple files, and plots a graph of FRD vs angle of all rings (note that for this function, name of the directory should be entered in the corresponding space).

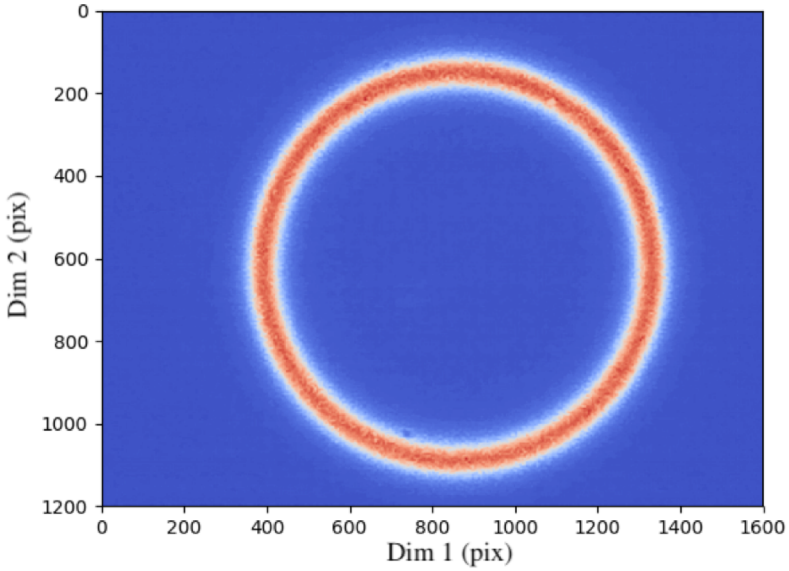

Figure 5.5: The output of the "Display" function in RAPID. The colour scale is based on the intensity of each pixel in the image.

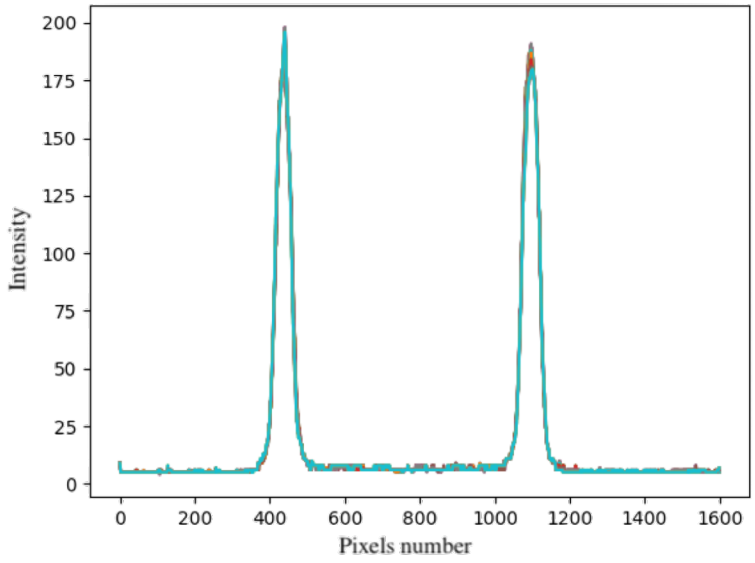

Figure 5.6: The output of the "Slice" function in RAPID. This function shows the intensity plot of a thin slice of the ring. The size of the slice varies depends on the input values for "Dim1" and "Dim2".

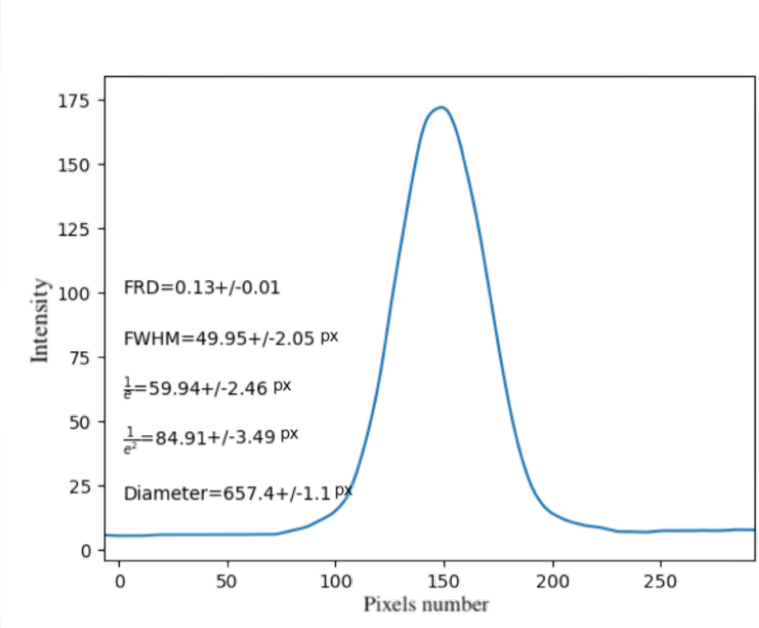

Figure 5.7: The output of the "Peak Finder" function in RAPID. This function labels all peaks in the system and stores their pixel numbers.

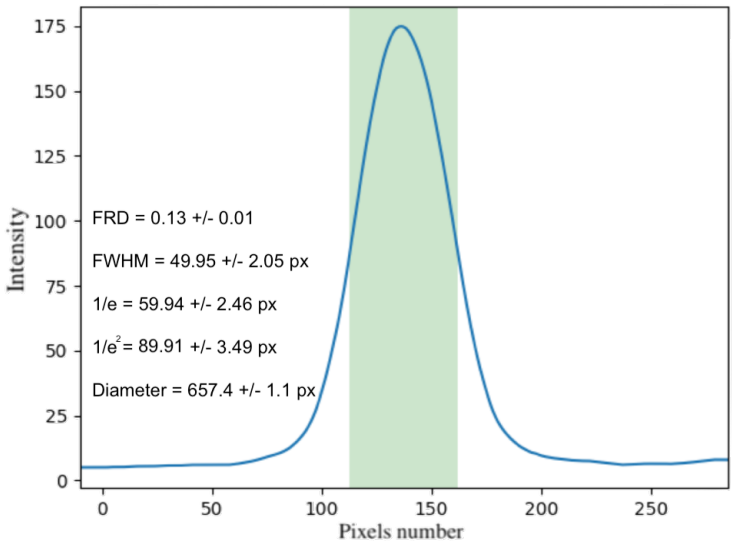

Figure 5.8: The output of the "FWHM, ..." function in RAPID. This function shows the intensity plot with the measured diameter and FRD. Note that the FWHM of the Gaussian peak is highlighted.

5.3 Future Stability Test

When light is injected through an optical fibre, the output light could vary from the original light due to the variation in the enviornment's temperature, external disturbances and mechanical tensions. In particular for quality and time sensitive signals, the mentioned factors can be crucial. In order to meet the current science requirements for the MSE project (i.e. optical fibres with 1% consistency and FRD of less than 5%), the stability of the fibres has to be quantified. Therefore, the future stablity tests will evaluate different internal and external variables affecting a signal's transmission in an optical fibre.
Our evaluation will be based on four components:

- **Temperature:** The consistency of the signal's transmission in optical fibres can be violated if the setup's temperature be unstable. In particular, the light source can heat up the body of the optical fibres. Through our collimated ring tests, we noticed that the hotter fibres form a fainter ring. This signal loss in the hot fibres will be evaluated by measuring the temperature of the fibre ends and cooling down the overall temperature by mechanical fans.

- **Mechanical Tensions:** The dynamical changes and mechanical tensions can directly change the path of light's propagation inside of the fibre, resulting into inconsistent transmission of the signal. This effect will be evaluated by designing a new setup to move, press and stretch the fibres in a measureable manner.

- **Fibre's Ends:** The most common stability test is injecting light in both directions (i.e. swapping the fibre ends) and measuring the FRD of the system. Comparison between the FRD of the two ends can show systematic errors and also possible inaccuracies from the fibre surface and the cladding.

- **The light's wavelength:** Finally, the sensitivity of the optical fibres to the input light's wavelength will be evaluated. This can be done by performing the ring test for different light sources and comparing their FRD with each other.

5.4 Summary

The Maunakea Spectroscopic Explorer (MSE) facility is designed with over 4000 optical fibres with well-known characteristics. The UVic's Fibre Transmission System

(FiTS) team examined the quality of different optical fibres to find the best candidate fibres for the MSE project. Through this project, we introduced a master Python wrapper for optical fibre quality tests that performs the ring test on an optical fibre within a few minutes. This is significantly faster than the traditional techniques. The FiTS team achieved the focal ratio degradation (FRD) measurement of 3.7% at f/2, which is well within the science requirement of the MSE project (i.e. FRD of less than 5% at f/2).

Chapter 6

Conclusion

This thesis has presented multiple spectroscopic and instrumental projects with the unifying theme of increasing the efficiencies in spectroscopic surveys. The main results and the future works for the projects are highlighted as follows:

- Multiple members of Palomar 1 (Pal 1) are examined by abundance and dynamical analysis of stars in the APOGEE database. Abundances for more than ten elements of the Pal 1 members and candidates are determined using FERRE, and the binarity of them are studied by examination of their heliocentric velocity. In addition, we found the destructive effect of the persistence on our raw data. We proposed a new technique to remove and calibrate the spectra with persistence. By examination of the effect of persistence, we conclude that persistence does not necessarily affect the abundance analysis, but when it does, it is critical. Therefore complete or partial removal of persistence is recommended.

- In the DAO-Pristine project, several candidate Extrememly Metal Poor (EMP) stars from the Pristine database were observed. We could successfully narrow-down the initial list of the candidates by observing over 48 new stars from the Pristine survey. Twelve stars had weak Ca II triplet absorption lines in their spectra. Therefore, they are chosen as suitable EMP candidates for the follow-up observations. In the future, the best EMP candidates from the DAO-Pristine project will be observed with larger telescopes such as INT in La Palma, Spain.

- Different applications of machine learning in astronomy were examined. We worked on both supervised and unsupervised perspectives of the machine learning techniques. Our neural network structure, StarNet, determined the stellar parameters of the red giant stars in APOGEE database efficiently and accu-

rately. In addition the unsupervised attempts for spectral analysis of Supernovae Type Ia (SNIa) and stars could reproduce results from the previous studies in a more efficient manner. In the future, new artificial intelligence structures will be tested to expand our current techniques. For the StarNet project, the optical spectra will be tested on the StarNet and abundance of more elements will be examined. Also, for the unsupervised project, the spectra and light curves of different types of supernovae will be added to our training set.

- The Fibre Transmission System (FiTS) project, as a part of the Maunakea Spectroscopic Explorer (MSE), is the last component of this thesis. Through the FiTS project, we designed and implemented an optical system for checking the quality of the optical fibres. A new software is also developed that could perform the ring test on the fibres in a fully automated manner for the first time. Our preliminary results suggest that we achieved Focal Ratio Degradation (FRD) of 3.7% at f/2, which is less than the science requirement of the MSE project (i.e. FRD of less than 5%). In the future, our current system will be extended to perform the ring and stability tests on multiple fibres simultaneously. The ultimate goal of this project is testing over 4000 optical fibres for the MSE project in a precise and efficient manner.

Bibliography

Albareti, F. D. et al. 2016, arXiv preprint arXiv:1608.02013

Anderson, R. E., Regan, M., Valenti, J., & Bergeron, E. 2014, arXiv preprint arXiv:1402.4181

Anthony-Twarog, B. J. & Twarog, B. A. 1998, The Astronomical Journal, 116, 1922

Armandroff, T. & Da Costa, G. 1991, The Astronomical Journal, 101, 1329

Armandroff, T. E. & Zinn, R. 1988, The Astronomical Journal, 96, 92

Beers, T. C. & Christlieb, N. 2005, Annu. Rev. Astron. Astrophys., 43, 531

Belokurov, V. et al. 2007, The Astrophysical Journal, 658, 337

Bensby, T., Feltzing, S., & Oey, M. 2014, Astronomy & Astrophysics, 562, A71

Bonifacio, P., Sbordone, L., Marconi, G., Pasquini, L., & Hill, V. 2004, Astronomy & Astrophysics, 414, 503

Bovy, J., Bahmanyar, A., Fritz, T. K., & Kallivayalil, N. 2016a, The Astrophysical Journal, 833, 31

Bovy, J., Erkal, D., & Sanders, J. L. 2016b, Monthly Notices of the Royal Astronomical Society, stw3067

Bowen, I. & Vaughan, A. 1973, Applied Optics, 12, 1430

Caffau, E. et al. 2017, Astronomische Nachrichten, 338, 686

Carlberg, R., Grillmair, C., & Hetherington, N. 2012, The Astrophysical Journal, 760, 75

Carollo, D. et al. 2010, The Astrophysical Journal, 712, 692

— 2007, Nature, 450, 1020

Carrera, R., Pancino, E., Gallart, C., & del Pino, A. 2013, Monthly Notices of the Royal Astronomical Society, 434, 1681

Carretta, E. et al. 2010, Astronomy & Astrophysics, 520, A95

Casagrande, L., Ramírez, I., Melendez, J., Bessell, M., & Asplund, M. 2010, Astronomy & Astrophysics, 512, A54

Chené, A.-N. et al. 2014, in Advances in Optical and Mechanical Technologies for Telescopes and Instrumentation, Vol. 9151, International Society for Optics and Photonics, 915147

Chou, M.-Y., Majewski, S. R., Cunha, K., Smith, V. V., Patterson, R. J., & Martínez-Delgado, D. 2010, The Astrophysical Journal Letters, 720, L5

Cohen, J. G. 2004, The Astronomical Journal, 127, 1545

Cohen, J. G., Christlieb, N., McWilliam, A., Shectman, S., Thompson, I., Melendez, J., Wisotzki, L., & Reimers, D. 2008, The Astrophysical Journal, 672, 320

Conroy, C. 2012, The Astrophysical Journal, 758, 21

Deason, A. et al. 2012, Monthly Notices of the Royal Astronomical Society, 425, 2840

Djorgovski, S. G., Mahabal, A., Drake, A., Graham, M., & Donalek, C. 2013, in Planets, Stars and Stellar Systems (Springer), 223–281

Doi, M. et al. 2010, The Astronomical Journal, 139, 1628

Dotter, A., Chaboyer, B., Jevremović, D., Kostov, V., Baron, E., & Ferguson, J. W. 2008, The Astrophysical Journal Supplement Series, 178, 89

Fabbro, S., Venn, K., O'Briain, T., Bialek, S., Kielty, C., Jahandar, F., & Monty, S. 2017, arXiv preprint arXiv:1709.09182

Frebel, A. & Norris, J. E. 2015, Annual Review of Astronomy and Astrophysics, 53, 631

Fukugita, M., Ichikawa, T., Gunn, J., Doi, M., Shimasaku, K., & Schneider, D. 1996, The Astronomical Journal, 111, 1748

Girardi, L., Bertelli, G., Bressan, A., Chiosi, C., Groenewegen, M., Marigo, P., Salasnich, B., & Weiss, A. 2002, Astronomy & Astrophysics, 391, 195

Grillmair, C. 2006, The Astrophysical Journal Letters, 645, L37

Gunn, J. et al. 1998, The Astronomical Journal, 116, 3040

Gunn, J. E. et al. 2006, The Astronomical Journal, 131, 2332

Harris, W. E. 1996, The Astronomical Journal, 112, 1487

Hattori, K., Yoshii, Y., Beers, T. C., Carollo, D., & Lee, Y. S. 2013, The Astrophysical Journal Letters, 763, L17

Hawkins, K., Masseron, T., Jofre, P., Gilmore, G., Elsworth, Y., & Hekker, S. 2016, Astronomy & Astrophysics, 594, A43

Hill, V., François, P., Spite, M., Primas, F., & Spite, F. 2000, arXiv preprint astro-ph/0009273

Hinkle, K., Wallace, L., & Livingston, W. 2003, in Bulletin of the American Astronomical Society, Vol. 35, 1260

Holtzman, J. A. et al. 2015, The Astronomical Journal, 150, 148

Ishigaki, M. N., Hwang, N., Chiba, M., & Aoki, W. 2016, The Astrophysical Journal, 823, 157

Jordi, K., Grebel, E. K., & Ammon, K. 2006, Astronomy & Astrophysics, 460, 339

Jovanovic, N. et al. 2017, Optics Express, 25, 17753

Kafle, P. R., Sharma, S., Lewis, G. F., & Bland-Hawthorn, J. 2012, The Astrophysical Journal, 761, 98

Kaiser, N. et al. 2002, in Survey and Other Telescope Technologies and Discoveries, Vol. 4836, International Society for Optics and Photonics, 154–165

Kaiser, N. et al. 2010, in Ground-based and Airborne Telescopes III, Vol. 7733, International Society for Optics and Photonics, 77330E

Kirby, E. N., Guhathakurta, P., Zhang, A. J., Hong, J., Guo, M., Guo, R., Cohen, J. G., & Cunha, K. 2016, The Astrophysical Journal, 819, 135

Kohonen, T. 1990, Proceedings of the IEEE, 78, 1464

MacQueen, J. et al. 1967in , Oakland, CA, USA, 281–297

Majewski, S., Schiavon, R., Frinchaboy, P., & et al. 2015, arXiv preprint arXiv:1701.03802

Martin, N., Ibata, R., Conn, B., Lewis, G., Bellazzini, M., Irwin, M., & McConnachie, A. 2004, Monthly Notices of the Royal Astronomical Society, 355, L33

Monaco, L., Saviane, I., Correnti, M., Bonifacio, P., & Geisler, D. 2011, Astronomy & Astrophysics, 525, A124

Mucciarelli, A., Carretta, E., Origlia, L., & Ferraro, F. R. 2008, The Astronomical Journal, 136, 375

Muthukrishna, D. 2016, PhD Thesis, The University of Queensland

Nidever, D. L. et al. 2015, The Astronomical Journal, 150, 173

Niederste-Ostholt, M., Belokurov, V., Evans, N., Koposov, S., Gieles, M., & Irwin, M. 2010, Monthly Notices of the Royal Astronomical Society: Letters, 408, L66

Pallottini, A., Ferrara, A., Gallerani, S., Salvadori, S., & D'Odorico, V. 2014, Monthly Notices of the Royal Astronomical Society, 2498

Paunzen, E., Heiter, U., Netopil, M., & Soubiran, C. 2010, Astronomy & Astrophysics, 517, A32

Paust, N. E. et al. 2010, The Astronomical Journal, 139, 476

Pazder, J., Fournier, P., Pawluczyk, R., & van Kooten, M. 2014, in Advances in Optical and Mechanical Technologies for Telescopes and Instrumentation, Vol. 9151, International Society for Optics and Photonics, 915124

Peacock, M. B., Strader, J., Romanowsky, A. J., & Brodie, J. P. 2015, The Astrophysical Journal, 800, 13

Pérez, A. E. G. et al. 2016, The Astronomical Journal, 151, 144

Pietrinferni, A., Cassisi, S., Salaris, M., & Castelli, F. 2004, The Astrophysical Journal, 612, 168

Prieto, C. A., Beers, T. C., Wilhelm, R., Newberg, H. J., Rockosi, C. M., Yanny, B., & Lee, Y. S. 2006, The Astrophysical Journal, 636, 804

Ramírez, I. & Meléndez, J. 2005, The Astrophysical Journal, 626, 465

Robin, A. C., Reylé, C., Derrière, S., & Picaud, S. 2003, Astronomy & Astrophysics, 409, 523

Sakari, C., McWilliam, A., & Wallerstein, G. 2017, arXiv preprint arXiv:1701.03802

Sakari, C. M., Venn, K. A., Irwin, M., Aoki, W., Arimoto, N., & Dotter, A. 2011, The Astrophysical Journal, 740, 106

Salaris, M. & Weiss, A. 2002, Astronomy & Astrophysics, 388, 492

Salaris, M., Weiss, A., & Percival, S. M. 2004, Astronomy & Astrophysics, 414, 163

Sarajedini, A. et al. 2007, The Astronomical Journal, 133, 1658

Sasdelli, M. et al. 2016, Monthly Notices of the Royal Astronomical Society, 461, 2044

Sbordone, L., Bonifacio, P., Buonanno, R., Marconi, G., Monaco, L., & Zaggia, S. 2007, Astronomy & Astrophysics, 465, 815

Schlafly, E. F. & Finkbeiner, D. P. 2011, The Astrophysical Journal, 737, 103

Siegel, M. H. et al. 2007, The Astrophysical Journal Letters, 667, L57

Smith, R. M., Zavodny, M., Rahmer, G., & Bonati, M. 2008, in High Energy, Optical, and Infrared Detectors for Astronomy III, Vol. 7021, International Society for Optics and Photonics, 70210J

Sneden, C. A. 1973, PhD thesis, The University of Texas at Austin

Sommer-Larsen, J., Beers, T., Flynn, C., Wilhelm, R., & Christensen, P. 1997, The Astrophysical Journal, 481, 775

Starkenburg, E. et al. 2010, Astronomy & Astrophysics, 513, A34

— 2017, Monthly Notices of the Royal Astronomical Society, 471, 2587

Tolstoy, E., Hill, V., & Tosi, M. 2009, Annual Review of Astronomy and Astrophysics, 47, 371

Twarog, B. A. & Anthony-Twarog, B. J. 1995, The Astronomical Journal, 109, 2828

Twarog, B. A., Vargas, L. C., & Anthony-Twarog, B. J. 2007, The Astronomical Journal, 134, 1777

van Leeuwen, F. 2009, Astronomy & Astrophysics, 497, 209

VandenBerg, D. A., Bergbusch, P. A., & Dowler, P. D. 2006, The Astrophysical Journal Supplement Series, 162, 375

Venn, K. A., Irwin, M., Shetrone, M. D., Tout, C. A., Hill, V., & Tolstoy, E. 2004, The Astronomical Journal, 128, 1177

Venn, K. A. et al. 2012, The Astrophysical Journal, 751, 102

Ventura, P. & D'Antona, F. 2008, Astronomy & Astrophysics, 479, 805

Villanova, S., Geisler, D., Carraro, G., Bidin, C. M., & Muñoz, C. 2013, The Astrophysical Journal, 778, 186

York, D. G. et al. 2000, The Astronomical Journal, 120, 1579

Youakim, K. et al. 2017, Monthly Notices of the Royal Astronomical Society, 472, 2963

Zasowski, G. et al. 2013, The Astronomical Journal, 146, 81